



UNIVERSITÀ DEGLI STUDI DI NAPOLI FEDERICO II

DOTTORATO DI RICERCA IN RISCHIO SISMICO

XIX CICLO – 2006

**Feasibility study of a seismic sensor
using a suspended Fabry-Perot cavity**

Iolanda Ricciardi



UNIVERSITÀ DEGLI STUDI DI NAPOLI FEDERICO II

DOTTORATO DI RICERCA IN RISCHIO SISMICO

XIX CICLO - 2006

Iolanda Ricciardi

**Feasibility study of a seismic sensor
using a suspended Fabry-Perot cavity**

Advisor: Ch.mo Prof. Leopoldo Milano

Co-Advisor: dr. Guido Russo

Ph.D. Coordinator: Ch.mo Prof. Paolo Gasparini

AUTHOR'S ADDRESS:

Iolanda Ricciardi

Dipartimento di Scienze Fisiche

Università degli Studi di Napoli "Federico II"

Complesso Universitario di Monte Sant'Angelo,

Via Cintia - 80126 Napoli, Italy

E-MAIL: iolanda.ricciardi@na.infn.it

WWW: [people.na.infn.it~iricciar](http://people.na.infn.it/~iricciar)

Contents

Introduction	1
1 Basic seismological theory	4
1.1 Stress and strain	4
1.1.1 The Stress tensor	5
1.1.2 Equation of motion	8
1.1.3 The Strain tensor	9
1.1.4 Constitutive equations	10
1.1.5 Boundary conditions	11
1.1.6 Strain energy	12
1.2 Seismic waves	12
1.2.1 The seismic wave equation	13
1.2.2 Plane and spherical waves	15
1.2.3 P and S waves	16
1.2.4 Energy in P and S waves	18
1.2.5 Surface waves	20
1.2.6 Principles for seismic waves propagation	24
1.2.7 Normal modes of the Earth	27
1.3 Seismometers and seismological networks	30
1.3.1 Introduction	30
1.3.2 The damped harmonic oscillator	30
1.3.3 Earth noise	32
1.3.4 Seismometers, seismographs and seismological networks	33
2 Interferometric seismic sensors	39
2.1 The Fabry Perot interferometer	39
2.1.1 Optical interference	39

2.1.2	Laser beams: approximate solution for the wave equation	41
2.1.3	Propagation laws for the fundamental beam	42
2.1.4	Higher order modes	43
2.1.5	Optical cavities	45
2.2	Optical interferometers as seismic sensors	47
2.3	The Fabry Perot interferometer as a speed-meter	50
2.4	Fabry Perot seismic interferometers	52
3	Reading and actuation systems for suspended mass control	54
3.1	Optical reading system for suspended mass	54
3.2	Coil-magnet system of actuation: description and limitations	56
3.3	Current model for electrostatic actuators	57
3.3.1	Periodic sequence of strips at alternate potentials	58
3.4	New theoretical simulations and experimental results	61
3.4.1	Optimization of the algorithm to calculate the capacitance	61
3.4.2	Optimization of the actuator design	61
3.4.3	Refined theoretical model	62
3.4.4	Simulations of the force	63
3.5	Experimental set up, measures and results	63
4	Fabry Perot seismic sensor and experimental data	75
4.1	Experimental set-up	75
4.1.1	Optical components for the Fabry Perot interferometer	75
4.2	Fabry Perot with two fixed mirrors: first experimental data	79
4.2.1	Optical bench transfer function	79
4.2.2	Piezo actuator transfer function	86
4.2.3	Mode matching and alignment of the interferometer	86
4.2.4	First comparison between Episensor and Fabry Perot	90
4.3	Signal reconstruction algorithm: basic theory and experimental data	93
4.3.1	Signal reconstruction algorithm: basic theory	93
4.3.2	Reconstruction of longitudinal motions	95
4.4	Fabry Perot with a suspended mirror: experimental data and critical analysis	100
4.4.1	Critical analysis	107
5	Mechanical simulations and sensitivity curve of a 3mx3m Michelson interferometer	110
5.1	Inverted pendulum	113

5.1.1	Lagrangian model of the inverted pendulum	114
5.2	Pendular mirror suspension subsystem	117
5.2.1	Lagrangian model	118
5.2.2	Static Lagrangian	119
5.2.3	Total Lagrangian	119
5.3	Sensitivity curve of the Michelson suspended interferometer	124
5.3.1	Environmental noise	127
5.3.2	Optical noise	128
5.3.3	Thermal noise	130
Conclusions		135
A Electric field by an array of electrodes in the presence of dielectrics		137
A.1	Free space electrodes	137
A.2	Electrodes on a dielectric substrate	139
A.3	Electrodes in the presence of a mirror	140
B Potential methods		141
B.1	Potential energy of the elastic line	141
B.2	Violin modes	146
B.3	Matrix method for transfer functions	147
C Thermal noise in seismic interferometers		149
C.1	Suspension wires thermal noise	149
C.2	Test mass thermal noise	151
C.3	Thermodynamical noise in the mirrors	152
C.4	Heating by laser beam	153

Introduction

The aim of Seismic Risk is to mitigate the effects of earthquakes on people and society. The output of a seismic risk analysis is the probability of damage and fatalities as a consequence of natural or artificial seismological phenomena. The estimation of risk requires both the theoretical study of the probability of occurrence of earthquakes and the study of the potentiality of people, goods and buildings to be damaged because of earthquakes.

In particular the study of past earthquakes and the systematic collection of geophysical data can help to forecast the location and size of future earthquakes: to this scope, nowadays many instruments exist to record ground motion and monitor seismicity in different dynamical and frequency ranges.

This thesis work has been developed with the aim of studying the performances of a Fabry Perot interferometer as a very sensitive detector of the ground motion: for this reason various arguments belonging to different fields of research have been analyzed.

First of all it is presented the analysis of the basic working principle of a seismometer, as a device put on the ground, able to read the ground motion: this is achieved by suspending the sensitive part of the seismometer using a damped harmonic oscillator, that filters the ground motion in a given frequency band. Moreover, classical seismometers use capacitive or electromagnetic systems to read displacements. In the first case the sensing mass is connected to the center plate of a capacitor whose outer plates are fixed: as the mass moves, the voltage between the center plate and the outer plates is proportional to the displacement. In the second case the motion of the mass relative to the frame is measured by moving a coil attached to the mass through the magnetic field produced by a magnet fixed to the seismometer frame.

The alternative proposed in this work is the use of a Fabry Perot as a very sensitive device to measure relative displacements. A Fabry Perot cavity is composed by two mirrors aligned in such a way that a light beam is reflected in a closed path, and, after one round trip, it interferes perfectly with the incident wave. The light is reflected many times inside the cavity: each round trip generates a partial wave, and all these waves interfere. When the length of the cavity is an integer multiple of the wavelength of the incident light, a strong field is built up inside the cavity due to constructive interference, then the cavity is said to be on resonance: in this situation the transmitted power contains sensitive informations about the relative displacements of the two mirrors.

Successively, to make a Fabry Perot a seismometer, it is necessary to decouple the motion of one of its mirrors from the ground: this can be done by suspending this mirror to the last stage of a double pendulum, that constitutes a low pass filter for the ground motion. The mechanical transfer function of a double pendulum shows in fact three distinct behaviours in three frequency ranges: a flat response for frequencies lower than the resonances; two resonance peaks, corresponding to an amplification of the ground motion; a reduction of the transmitted motion for frequencies higher than the resonances.

All the above aspects, from optical interference to mechanical suspension systems, have been analyzed and improved in this thesis, step by step.

The first chapter contains an overview of the basic concepts of seismology and seismometry. It starts with the description of stresses and strains inside the materials in terms of continuum mechanics, and successively analyzes the seismic wave equation and the main features of seismic waves. The second part of the chapter is devoted to seismometry, with a general analysis of the working principle of seismic instrumentation, and a particular attention on the currently used seismometers.

The second chapter concerns interferometry, both from the optical point of view and in the field of geophysical applications. The chapter starts with the optical treatment of interference for two beams and multiple beams, and describes in detail the theory of gaussian beams and of Fabry Perot resonators. The second part of the chapter contains a list of applications of Michelson and Fabry Perot interferometers in the field of geophysics, as instruments to obtain measurements of free oscillations of the earth and crustal strain, and earth tides and seismic noise monitoring. The chapter ends with the analysis of the possible use of a Fabry Perot as a speed-meter and the calculus of the interferometer transfer function with respect to a seismic perturbation.

The third chapter is devoted to the control of the double pendulum used to isolate the mirror from the ground motion. The chapter starts with the description of the reading and actuation systems used to keep the position and orientation of the pendulum stages around a certain value. The second part of the chapter contains the description of an alternative to the coil-magnet system based on the electrostatic actuation. This system has been already introduced to control the last pendulum stages because it does not require the attachment of magnets on the surface of the mass to be controlled: in this way there is no need to alter the symmetry of the mirror and, as a consequence, its resonance factor. In this chapter the current theoretical model for the electrostatic actuation is analyzed and refined and new experimental data confirm that this system can represent a good alternative to the magnetic actuation system, when some forces from μN to mN is needed.

The fourth chapter contains all the significant experimental data collected during this thesis work. It starts with a detailed description of the experimental set-up in all its optical and mechanical parts, then it continues with the list and analysis of several sets of measurements performed. The first data concern the test on a Fabry Perot interferometer made-up of two mirrors fixed to an optical bench: these measurements

aimed to verify the consistence of the properties of the real cavity with respect to the design (beam waist, finesse, line width) and to the alignment of the cavity in a standard configuration. The second set of data contains the characterization of the mechanical transfer function of the optical bench with respect to the ground in order to link the motion read by the cavity on the bench with the ground motion. The third set of data concerns the test on the algorithm to reconstruct the relative motion of the mirrors by using the reflected cavity power: it contains several examples of reconstruction of sinusoidal and random longitudinal motions. The last set of data concerns the Fabry Perot cavity with a fixed mirror and a suspended one. The chapter ends with a critical discussion on the experimental results.

The last chapter contains several theoretical simulations on the Michelson interferometer currently under development in the Virgo lab in Napoli. The main feature of this interferometer is the ULF (Ultra Low Frequency) system of suspension for optics and mirrors, made up of a pendular chain with four stages, whose first resonance frequency can be tuned in the range of mHz: this interferometer seems to be very promising for sensitive seismic measurements at very low frequencies. The first part of the chapter describes the lagrangian model and the mechanical simulations of the transfer functions of the suspension system, while the second part is devoted to the calculus of the sensitivity curve of the interferometer, with the analysis of the main expected noise contributions, among which seismic noise.

Chapter 1

Basic seismological theory

The principal aim of seismological theory is to understand how the physics of the solid earth allows the propagation of seismic waves and how the propagation of seismic waves depends on the nature of the materials within the earth: in his *Lectures on Physics* Richard Feynmann told that by using a large number of observations of many earthquakes at different places we could know *what is inside the earth*.

In the first part of this chapter we will introduce many basic concepts of the seismological theory: we will talk about the forces acting on a solid material and the consequent deformations, we will analyze the relations within displacements inside the material as functions of position and time satisfying the seismic wave equation and we will discuss about *P* and *S* waves in particular.

In the second part of the chapter we will introduce some ideas about *seismometry*, the design and development of seismic instrumentation. We will talk about the basic problem of seismometry: how to measure the motion of the ground using an instrument put on the ground, too. We will describe then the various types of seismometers and give some hints about seismological networks: in this picture the systematic collection of geophysical data helps to forecast the location and size of future earthquakes [1].

1.1 Stress and strain

In this section we will introduce some concepts and some basic results of *continuum mechanics*, necessary for introductory seismology [2] [3]. *Continuum mechanics* describes the behaviour of continuous deformable materials made up of particles packed so closely together that density, force and displacements can be thought as continuous and differentiable functions. This approximation breaks down on atomic distance scale, but it is adequate for most seismological problems. For these applications we can write Newton's law, in the hypothesis of constant density, as:

$$\mathbf{f}(\mathbf{x}, t) = \rho \frac{\partial^2 \mathbf{u}(\mathbf{x}, t)}{\partial t^2}. \quad (1.1)$$

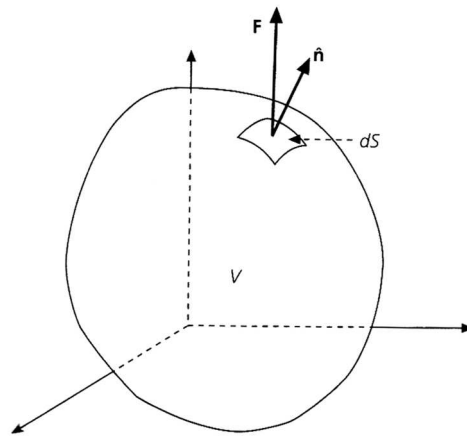


Figure 1.1: Surface force acting on a volume element V within the material: the surface force \mathbf{F} due to the material outside V acts on each element of surface dS , which has a outward-pointing unit normal $\hat{\mathbf{n}}$.

The goal of this section is to characterize a continuous medium and its response to applied forces: to this aim we will introduce the *stress tensor* that describes the forces acting on a deformable continuous medium.

We will then formulate the *equation of motion*, the version of Newton's law appropriate for a continuous medium, which relates the stress to the displacement. The variation of the displacement, which gives rise to internal deformation within the material, is then described by the *strain tensor*: this deformation is linked to the stress via the *constitutive equation* that characterizes the properties of the various materials.

1.1.1 The Stress tensor

We start this subsection talking about the two types of forces that can act on an object:

- the *body force*, which acts everywhere within an object, resulting in a net force proportional to the volume of the object
- the *surface force*, which acts on the surface of an object, yielding a net force proportional to the surface area of the object

A familiar example of body force is the force due to gravity, while pressure is a typical example of surface force.

We consider now the forces acting on a small volume V , with surface S , within a larger continuous medium (fig. 1.1).

The material inside V is affected by body forces acting on everything inside V and surface forces, due to the material outside, acting on the surface S . If the surface force \mathbf{F} acts on each element of surface dS , whose outward unit normal is $\hat{\mathbf{n}}$, we define the traction vector \mathbf{T} , as the limit of surface force per unit area

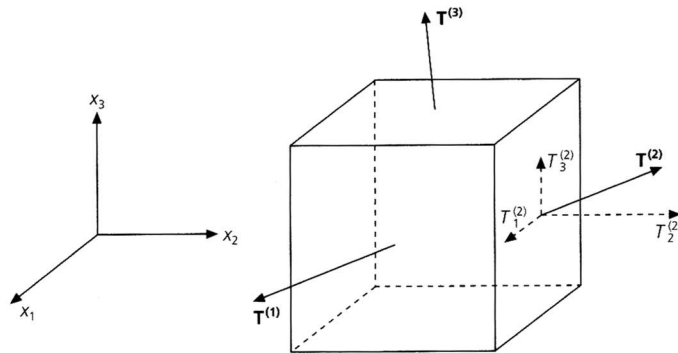


Figure 1.2: Traction vectors acting on three faces of a volume element which are perpendicular to the coordinate axes.

at any point as the area becomes infinitesimal:

$$T(\hat{\mathbf{n}}) = \lim_{dS \rightarrow 0} \frac{\mathbf{F}}{dS}. \quad (1.2)$$

The traction vector has the same orientation as the force, and is a function of the unit normal vector $\hat{\mathbf{n}}$ because it depends on the orientation of the surface.

The system of surface forces acting on a volume is described by three traction vectors: each acts on a surface perpendicular to a coordinate axis (fig. 1.2). We define $\mathbf{T}^{(j)}$ as the traction vector acting on the surface whose outward normal is in the positive $\hat{\mathbf{e}}_j$ direction. The components of the three traction vectors are $T_i^{(j)}$, where the upper index (j) indicates the surface and the lower index (i) indicates the component.

This set of nine terms that describes the surface forces can be grouped into the *stress tensor* σ_{ij} . The tensor's rows are the three traction vectors, such that:

$$\sigma_{ij} = \begin{pmatrix} \sigma_{11} & \sigma_{12} & \sigma_{13} \\ \sigma_{21} & \sigma_{22} & \sigma_{23} \\ \sigma_{31} & \sigma_{32} & \sigma_{33} \end{pmatrix} = \begin{pmatrix} \mathbf{T}^{(1)} \\ \mathbf{T}^{(2)} \\ \mathbf{T}^{(3)} \end{pmatrix} = \begin{pmatrix} T_1^{(1)} & T_2^{(1)} & T_3^{(1)} \\ T_1^{(2)} & T_2^{(2)} & T_3^{(2)} \\ T_1^{(3)} & T_2^{(3)} & T_3^{(3)} \end{pmatrix}. \quad (1.3)$$

The stress gives the force per unit area that the material on the outside (the side to which $\hat{\mathbf{n}}$ points) of the surface exerts on the material inside.

The stress tensor is related to the traction and normal vectors by:

$$T_i = \sigma_{ij} n_j, \quad (1.4)$$

where the repeated index indicates summation.

The three diagonal components of the stress tensor are known as *normal stresses*, while the six off diagonal components are called *shear stresses*: the corresponding components of the traction vector are called normal and shear tractions. Positive values of the normal tractions correspond to *tension*, whereas negative normal tractions correspond to *compression*.

An important property of the stress tensor is that it is symmetric:

$$\sigma_{ij} = \sigma_{ji}. \quad (1.5)$$

For a given state of stress, the traction vector acting on most surfaces within the material has components both normal to the surface and tangential to it.

There are however some surfaces oriented such that the shear tractions on them vanish: these surfaces can be characterized by their normal vectors, called *principal stress axes*; the normal stresses on these surfaces are called *principal stresses*. The principal stress axes $\hat{\mathbf{n}}$ are the eigenvectors of the stress tensor, while the principal stresses λ are the eigenvalues. The eigenvalues and eigenvectors can be found by solving the system of homogeneous linear equations:

$$(\sigma_{ij} - \lambda\delta_{ij})n_j = 0. \quad (1.6)$$

The concept of principal stress is very important for discussion of earthquake source mechanism: the simplest theory for rock fracture predicts that faulting will occur on the plane on which the shear stress is highest.

Deviatoric stresses

Large compressive stresses occur at depth within the earth due to the weight of the overlying rock. In many applications it is then convenient to remove the effect of the overall compressive stress and consider only the deviation from it. We thus define the *mean stress*:

$$M = (\sigma_{11} + \sigma_{22} + \sigma_{33})/3 = \sigma_{ii}/3, \quad (1.7)$$

as $\frac{1}{3}$ of the sum of the normal stresses, the trace of the stress tensor.

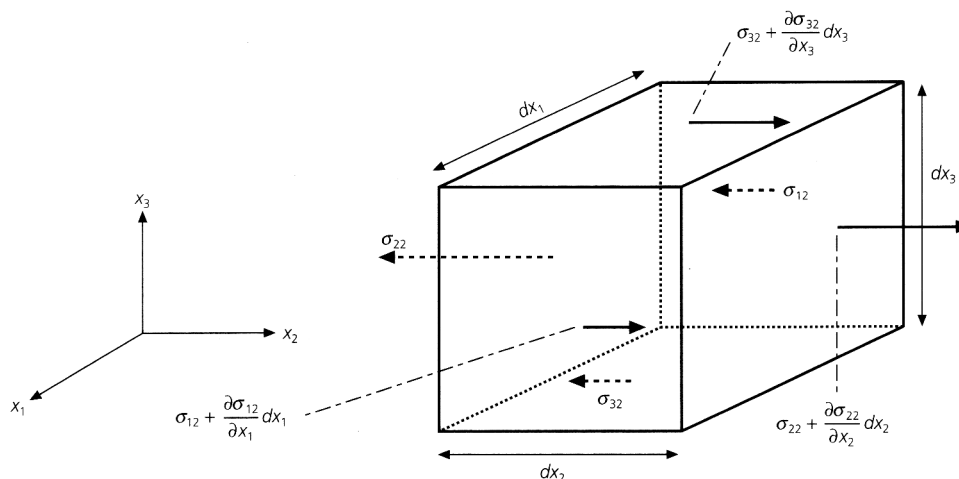
The *deviatoric* stress tensor is defined by removing the effect of the mean stress from the stress tensor:

$$D_{ij} = \sigma_{ij} - M\delta_{ij}, \quad (1.8)$$

$$D = \begin{pmatrix} \sigma_{11} - M & \sigma_{12} & \sigma_{13} \\ \sigma_{21} & \sigma_{22} - M & \sigma_{23} \\ \sigma_{31} & \sigma_{32} & \sigma_{33} - M \end{pmatrix}. \quad (1.9)$$

Thus, when the principle stresses are large and nearly equal, the deviatoric stress tensor removes their effects and indicates the remaining stress state.

This concept is important in discussing processes in the earth, because the deviatoric stresses result from tectonic forces and cause earthquake faulting and seismic wave propagation effects like anisotropy. At depths greater than few kilometers, we often assume that a *lithostatic* state of stress exists, where the normal stresses are equal to minus the pressure of the overlying material and the deviatoric stresses are zero. This assumption is only approximate, but it is useful because the mean stress is usually thought to be much greater than the deviatoric stress.

Figure 1.3: Stress components contributing to the force in the x_2 direction

1.1.2 Equation of motion

The first step to derive the equations describing seismic wave propagation is to write Newton's second law in terms of body forces and stresses.

Let us consider a block of material of density ρ and volume $dx_1 dx_2 dx_3$ (fig. 1.3). The total force acting on it is the sum of the surface forces on each face plus the body force within the material. Let us start from the body force: if f_i is the force for unit volume at the center of the block the net body force will be $f_i dx_1 dx_2 dx_3$.

For what concerns surface forces we analyze as an example the x_2 direction: the net surface force in this direction is the sum of three terms, each of which describes the force due to the difference in traction between opposite faces; we multiply this difference by the area of the two faces and then use a Taylor expansion, thus obtaining:

$$\left[\sigma_{22}(\mathbf{x}) + \frac{\partial \sigma_{22}(\mathbf{x})}{\partial x_2} dx_2 - \sigma_{22}(\mathbf{x}) \right] dx_1 dx_3 = \frac{\partial \sigma_{22}(\mathbf{x})}{\partial x_2} dx_1 dx_2 dx_3. \quad (1.10)$$

We do the same for the force in this direction due to the other pair of faces and sum these terms. At the end we sum the contribute of the body forces obtaining the following equation:

$$\frac{\partial \sigma_{ij}(\mathbf{x}, t)}{\partial x_j} + f_i(\mathbf{x}, t) = \rho \frac{\partial^2 u_i(\mathbf{x}, t)}{\partial t^2}. \quad (1.11)$$

This equation, called the *equation of motion* is satisfied everywhere in a continuous medium.

There are two important forms for this equation. An important form of the equation of motion describes a body at equilibrium, whose acceleration is zero, so the divergence of the stress tensor exactly balances the body forces:

$$\frac{\partial \sigma_{ij}(\mathbf{x}, t)}{\partial x_j} = -f_i(\mathbf{x}, t). \quad (1.12)$$

This equation must be satisfied for any static elasticity problem, such as finding the stresses due only to gravity.

Another important form, if no body forces are applied, is:

$$\frac{\partial \sigma_{ij}(\mathbf{x}, t)}{\partial x_j} = \rho \frac{\partial^2 u_i(\mathbf{x}, t)}{\partial t^2}. \quad (1.13)$$

This is called the *homogeneous equation of motion*, where homogeneous refers to the lack of forces: this equation describes seismic wave propagation except at a source, such as an earthquake or an explosion, where a body force generates seismic waves.

1.1.3 The Strain tensor

If stresses are applied to a material which is not rigid, points within it move respect to each other, and deformation results. The *strain tensor* describes the deformation resulting from the differential motion within the body.

We consider now an element of solid material within which displacements $\mathbf{u}(\mathbf{x})$ have occurred. If a point originally at \mathbf{x} (fig. 1.4) is displaced by \mathbf{u} , we describe the displacement of a nearby point originally at $\mathbf{x} + \delta(\mathbf{x})$ expanding the components of the displacement vector in a Taylor series:

$$u_i(\mathbf{x} + \delta(\mathbf{x})) \approx u_i(\mathbf{x}) + \frac{\partial u_i(\mathbf{x})}{\partial x_j} \delta x_j = u_i(\mathbf{x}) + \delta u_i, \quad (1.14)$$

so that the relative displacement near \mathbf{x} , δu_i , is to the first order:

$$\delta u_i = \frac{\partial u_i(\mathbf{x})}{\partial x_j} \delta x_j. \quad (1.15)$$

Until now we have been interested in deformations that distort the body: there can also be rigid translations or rotations, neither of which produce deformation. To distinguish these effects we use the expression:

$$\delta u_i = \frac{1}{2} \left(\frac{\partial u_i}{\partial x_j} + \frac{\partial u_j}{\partial x_i} \right) \delta x_j + \frac{1}{2} \left(\frac{\partial u_i}{\partial x_j} - \frac{\partial u_j}{\partial x_i} \right) \delta x_j = (e_{ij} + \omega_{ij}) \delta x_j. \quad (1.16)$$

The ω_{ij} term corresponds to a rigid body rotation without deformation. We note that ω_{ij} is symmetric, the diagonal terms are zero, and there are only three independent components.

The other term e_{ij} is the *strain tensor*, a symmetric tensor describing the internal deformations:

$$e_{ij} = \begin{pmatrix} \frac{\partial u_1}{\partial x_1} & \frac{1}{2} \left(\frac{\partial u_1}{\partial x_2} + \frac{\partial u_2}{\partial x_1} \right) & \frac{1}{2} \left(\frac{\partial u_1}{\partial x_3} + \frac{\partial u_3}{\partial x_1} \right) \\ \frac{1}{2} \left(\frac{\partial u_2}{\partial x_1} + \frac{\partial u_1}{\partial x_2} \right) & \frac{\partial u_2}{\partial x_2} & \frac{1}{2} \left(\frac{\partial u_2}{\partial x_3} + \frac{\partial u_3}{\partial x_2} \right) \\ \frac{1}{2} \left(\frac{\partial u_3}{\partial x_1} + \frac{\partial u_1}{\partial x_3} \right) & \frac{1}{2} \left(\frac{\partial u_3}{\partial x_2} + \frac{\partial u_2}{\partial x_3} \right) & \frac{\partial u_3}{\partial x_3} \end{pmatrix}. \quad (1.17)$$

Its tensor components are dimensionless and can be divided in two different types: the diagonal components, that show how the displacement of a coordinate axis varies along that axis; the off-diagonal components describe changes along a coordinate axis of displacement in another direction.

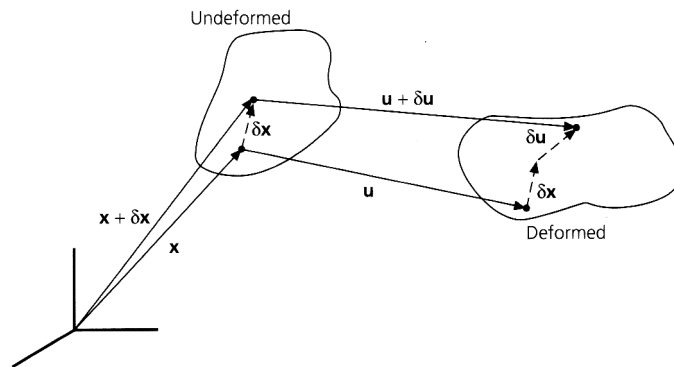


Figure 1.4: Geometry showing how deformation arises from the relative displacement δu between two points originally separated by δx .

The strain tensor can be characterized by its eigenvectors, the principal strain axes, and associated eigenvalues, the principal strains. The strain tensor is diagonal when expressed in a coordinate system whose basis vectors are the principal strain axes. The trace of the strain tensor:

$$\theta = e_{ii} = \frac{\partial u_1}{\partial x_1} + \frac{\partial u_2}{\partial x_2} + \frac{\partial u_3}{\partial x_3} = \nabla \cdot \mathbf{u}, \quad (1.18)$$

known as *dilatation*, equals the divergence of the displacement field $\mathbf{u}(\mathbf{x})$. The dilation has physical significance because it gives the change in volume per unit volume associated with the deformation.

1.1.4 Constitutive equations

Various materials respond differently to an applied stress: for a given stress a more rigid material responds with smaller strain respect to a less rigid material. This important relation between stress and strain is given by the material's *constitutive equation*. The simplest types of materials are *linearly elastic*, that is there is a linear relation between stress and strain. When the earth is linearly elastic, it gives rise to seismic waves: anyway we have to remember that the assumption of linear elasticity is valid for the time scale involved in the propagation of seismic waves, but not for longer time scales.

The stress and strain for a linearly elastic material are related by a constitutive equation known as *Hooke's law*:

$$\sigma_{ij} = c_{ijkl} e_{kl}. \quad (1.19)$$

The constants, c_{ijkl} , the *elastic moduli*, describe the properties of the material. The elastic moduli c_{ijkl} form a complicated tensor: it has four subscripts and has 81 independent components. Fortunately the number of independent components is strongly reduced by symmetry considerations. By considering in fact that the stress and strain tensors are symmetric and assuming that materials within the earth are *isotropic* the

independent components reduce to the number of two, and can be defined in various ways. One useful pair are the *Lame' constants* λ and μ defined such that:

$$c_{ijkl} = \lambda\delta_{ij}\delta_{kl} + \mu(\delta_{ik}\delta_{jl} + \delta_{il}\delta_{jk}). \quad (1.20)$$

In terms of the Lamé' constants the constitutive equation for an isotropic material is written:

$$\sigma_{ij} = \lambda e_{kk}\delta_{ij} + 2\mu e_{ij} = \lambda\theta\delta_{ij} + 2\mu e_{ij}. \quad (1.21)$$

We can also define other important constants, such as the *incompressibility*, or *bulk modulus* K :

$$K = \lambda + \frac{2}{3}\mu. \quad (1.22)$$

It describes the behaviour of a body subjected to a lithostatic pressure: the larger the value of K , the smaller the volume change produced by the pressure.

We write now the constitutive equation in terms of K and μ :

$$\sigma_{ij} = K\theta\delta_{ij} + 2\mu(e_{ij} - \theta\delta_{ij}/3). \quad (1.23)$$

This form of the constitutive equation shows that the response to an applied stress has two parts: a volume change characterized by K and a shear deformation, characterized by μ .

The last important elastic constants that can be defined are: ν , the *Poisson's ratio*, and E , the *Young's modulus*, with expressions:

$$\nu = \frac{\lambda}{2(\lambda + \mu)}, \quad E = \frac{\mu(3\lambda + 2\mu)}{\lambda + \mu}. \quad (1.24)$$

The first one gives the ratio of the contraction along the other two axes to the extension along the axis where the tension is applied, while the second one gives the ratio of the tensional stress to the resulting extensional strain. Many seismological problems are simplified by assuming that $\lambda = \mu$: such material, called a *Poisson's solid*, is often a good approximation for the earth.

1.1.5 Boundary conditions

The boundary conditions at the earth's surface are derived for most seismological purposes by neglecting the atmosphere and treating the surface as a boundary between a solid and a vacuum. In this approximation the earth's surface is a *free surface*, not subject to any force. At a free surface with normal $\hat{\mathbf{n}}$ the traction vector is zero, giving a constraint on those stress components that affect the components of the traction:

$$T_i = \sigma_{ij}n_j = 0. \quad (1.25)$$

The components of the stress tensor that do not affect the traction, σ_{11} , σ_{12} , and σ_{13} are unconstrained. For what concerns the interface between two solids we have that the three components of the traction vector $T_i = \sigma_{ij}n_j$ must be continuous across the interface. The continuity of traction leads to conditions on specific

stress components, depending on the orientation of the interface. For example if the surface is horizontal, then $n_j = \delta_{j3}$, so:

$$T_i = \sigma_{ij}\delta_{j3} = \sigma_{i3} \quad (1.26)$$

must be continuous.

At the interface between a solid and a perfect fluid the fluid can slip along the interface because its rigidity is zero, so it can support shear stress. Hence the components of tractions tangential to the interface are zero in the fluid and, for continuity, in the solid as well. Thus the tangential displacement components need not be continuous, but the normal components of the traction and displacements are continuous.

1.1.6 Strain energy

Because applying force to an elastic material causes deformation, potential energy is stored within this material. To motivate this *elastic strain energy* consider a spring with a restoring force $f = -kx$. Compressing the spring at a distance dx requires work against the spring, equal to the integral of the force applied times the distance. If the spring is initially at equilibrium, the work is:

$$W = \int_0^x kx dx = \frac{1}{2}kx^2, \quad (1.27)$$

which equals the potential energy stored in the spring.

By analogy, the strain energy stored in a volume is the integral of the product of stress and strain components summed:

$$W = \frac{1}{2} \int \sigma_{ij} e_{ij} dV = \frac{1}{2} \int c_{ijkl} e_{ij} e_{kl} dV. \quad (1.28)$$

The strain energy is symmetric both in ij and kl .

1.2 Seismic waves

In this section we will describe in detail the solutions of the equation of motion: the seismic waves. In particular we will see how this equation admits two types of propagating seismic waves: *compressional* and *shear* waves: these waves propagate differently, with velocities that depend in different way on the elastic properties of the materials.

We will also talk about surface waves, that originate from the interference between the above waves and whose energy is concentrated near the earth's surface.

At the end we will briefly talk about the most important principles for seismic waves propagation: these laws are not so far from the laws of propagation for electromagnetic waves.

1.2.1 The seismic wave equation

Let us now consider a homogeneous region of uniform properties, within an elastic material. We assume that the region contains no source of seismic waves, which requires a body force. Once the waves propagate away from the source the relation between stresses and displacements is given by the homogeneous equation of motion, which includes no body force terms, so we have:

$$\sigma_{ij,j}(\mathbf{x}, t) = \rho \frac{\partial^2 u_i(\mathbf{x}, t)}{\partial t^2}. \quad (1.29)$$

Before giving the solution we have to point out two important aspects: first, this equation can be written and solved entirely in terms of displacements, because the stress is related to strain, which is formed from derivatives of the displacement. The stress and strain are related by the constitutive relation, which characterizes the material: thus, although the equation of motion does not depend on the elastic constants, the solution does. Second, this equation relates spatial derivatives of the stress tensor to a time derivative of the displacement vector: the resulting solutions give the displacement vector and hence the stress and strain tensor as functions of both space and time.

We start solving the x component of eq. (1.29):

$$\frac{\partial \sigma_{xx}(\mathbf{x}, t)}{\partial x} + \frac{\partial \sigma_{xy}(\mathbf{x}, t)}{\partial y} + \frac{\partial \sigma_{xz}(\mathbf{x}, t)}{\partial z} = \rho \frac{\partial^2 u_x(\mathbf{x}, t)}{\partial t^2}. \quad (1.30)$$

Now we can use the constitutive law for an isotropic material: $\sigma = \lambda \theta \delta_{ij} + 2\mu e_{ij}$ and write the strains in terms of displacements. After some calculations and with the assumptions that we are in a homogeneous material (the elastic constants do not vary with position) we obtain:

$$(\lambda + \mu) \frac{\partial \theta}{\partial x} + \mu \nabla^2 u_x = \rho \frac{\partial^2 u_x}{\partial t^2}. \quad (1.31)$$

Similar equations can be obtained for the y and z components of displacements. The three equations can be now combined into a single vector equation:

$$(\lambda + \mu) \nabla(\nabla \cdot \mathbf{u}(\mathbf{x}, t)) + \mu \nabla^2 \mathbf{u}(\mathbf{x}, t) = \rho \frac{\partial^2 \mathbf{u}(\mathbf{x}, t)}{\partial t^2}. \quad (1.32)$$

Eq. (1.32) can be rewritten by the use of the vector identity:

$$\nabla^2 \mathbf{u} = \nabla(\nabla \cdot \mathbf{u}) - \nabla \times (\nabla \times \mathbf{u}), \quad (1.33)$$

to obtain:

$$(\lambda + 2\mu) \nabla(\nabla \cdot \mathbf{u}(\mathbf{x}, t)) - \mu \nabla \times \nabla \times \mathbf{u}(\mathbf{x}, t) = \rho \frac{\partial^2 \mathbf{u}(\mathbf{x}, t)}{\partial t^2}. \quad (1.34)$$

Seismic potentials

Instead of solving eq. (1.34) we can express the displacement field in terms of other two functions, ϕ and Ψ , which are known as potentials:

$$\mathbf{u}(\mathbf{x}, t) = \nabla \phi(\mathbf{x}, t) + \nabla \times \Psi(\mathbf{x}, t). \quad (1.35)$$

In this representation the displacement is the sum of the gradient of a *scalar potential* ϕ , and the curl of a *vector potential* Ψ , both of which are functions of space and time.

This decomposition is very useful in separating the displacement field into two parts, by the vector identities:

$$\nabla \times (\nabla \phi) = 0, \quad \nabla \cdot (\nabla \times \Psi) = 0. \quad (1.36)$$

The part associated with the scalar potential has no curl and gives rise to compressional waves. Conversely, the part associated with the vector potential has no divergence, causes no volume change, and corresponds to shear waves.

Substituting the potentials (1.35) into eq. (1.34) and rearranging the terms we obtain:

$$(\lambda + 2\mu)\nabla(\nabla^2\phi) - \mu\nabla \times \nabla \times (\nabla \times \Psi) = \rho \frac{\partial^2}{\partial t^2}(\nabla\phi + \nabla \times \Psi). \quad (1.37)$$

Now using the vector identity:

$$\nabla^2\mathbf{u} = \nabla(\nabla \cdot \mathbf{u}) - \nabla \times (\nabla \times \mathbf{u}), \quad (1.38)$$

the terms in eq. (1.34) can be regrouped to give:

$$\nabla \left[(\lambda + 2\mu)\nabla^2\phi(\mathbf{x}, t) - \rho \frac{\partial^2\phi(\mathbf{x}, t)}{\partial t^2} \right] = -\nabla \times \left[\mu\nabla^2\Psi(\mathbf{x}, t) - \rho \frac{\partial^2\Psi(\mathbf{x}, t)}{\partial t^2} \right]. \quad (1.39)$$

One solution of the equation can be found if both terms in the brackets are zero. In this case, we have two wave equations, one for each potential.

The scalar potential satisfies:

$$\nabla^2\phi(\mathbf{x}, t) = \frac{1}{\alpha^2} \frac{\partial^2\phi(\mathbf{x}, t)}{\partial t^2}, \quad (1.40)$$

with the velocity:

$$\alpha = \left(\frac{\lambda + 2\mu}{\rho} \right)^{1/2}. \quad (1.41)$$

This type of solution corresponds to P , or compressional waves.

Similarly the vector potential satisfies:

$$\nabla^2\Psi(\mathbf{x}, t) = \frac{1}{\beta^2} \frac{\partial^2\Psi(\mathbf{x}, t)}{\partial t^2}, \quad (1.42)$$

with velocity:

$$\beta = \left(\frac{\mu}{\rho} \right)^{1/2} \quad (1.43)$$

and corresponds to S , or shear waves.

The wave equations in eq. (1.40) and eq. (1.42) are strictly valid only for a homogeneous medium, because they were derived assuming that all derivatives of the elastic constants were zero, but they are also valid in any coordinate system, not only in the Cartesian one.

1.2.2 Plane and spherical waves

In this section we will briefly describe some particular solutions of scalar and vector wave equations: the *harmonic plane waves* and *spherical waves*.

Let's start from the scalar wave equation in three dimensions:

$$\nabla^2 \phi(\mathbf{x}, t) = \frac{1}{v^2} \frac{\partial^2 \phi(\mathbf{x}, t)}{\partial t^2}. \quad (1.44)$$

This is a homogeneous wave equation, without any forcing function acting as the source of the waves. A solution for this three dimensional equation is the *harmonic plane wave*:

$$\phi(\mathbf{x}, t) = A e^{i(\omega t \pm \mathbf{k} \cdot \mathbf{x})} = A e^{i(\omega t \pm k_x x \pm k_y y \pm k_z z)}, \quad (1.45)$$

where \mathbf{x} represents the position vector and $\mathbf{k} = (k_x, k_y, k_z)$ is the *wave vector*. The wave vector describes two important features of a propagating wave: its magnitude gives the spatial frequency, while its direction gives the direction of propagation. The wave fronts, which are at any time surfaces of constant phase ($\omega t - \mathbf{k} \cdot \mathbf{x}$) are planes perpendicular to the direction of propagation (fig. 1.5).

This solution to the three dimensional scalar wave equation can be generalized to solve the vector equation in three dimensions:

$$\nabla^2 \Psi(\mathbf{x}, t) = \frac{1}{\beta^2} \frac{\partial^2 \Psi(\mathbf{x}, t)}{\partial t^2}, \quad (1.46)$$

which describes the propagation of a vector field. In Cartesian coordinates this breaks up into three scalar wave equations:

$$\begin{aligned} \nabla^2 \psi_x(\mathbf{x}, t) &= \frac{1}{v^2} \frac{\partial^2 \psi_x(\mathbf{x}, t)}{\partial t^2}, \\ \nabla^2 \psi_y(\mathbf{x}, t) &= \frac{1}{v^2} \frac{\partial^2 \psi_y(\mathbf{x}, t)}{\partial t^2}, \\ \nabla^2 \psi_z(\mathbf{x}, t) &= \frac{1}{v^2} \frac{\partial^2 \psi_z(\mathbf{x}, t)}{\partial t^2}. \end{aligned} \quad (1.47)$$

The harmonic plane wave solution is then:

$$\Psi(\mathbf{x}, t) = \mathbf{A} e^{i(\omega t \pm \mathbf{k} \cdot \mathbf{x})}, \quad (1.48)$$

where $\Psi(\mathbf{x}, t)$ and the constant \mathbf{A} are vectors.

A second solution to the three dimensional scalar wave equation yields waves with spherical, rather than planar, wave fronts. The spherically symmetric waves satisfy the homogeneous wave equation in spherical coordinates:

$$\nabla^2 \phi(r, t) = \frac{1}{r^2} \frac{\partial}{\partial r} \left(r^2 \frac{\partial \phi(r, t)}{\partial r} \right) = \frac{1}{v^2} \frac{\partial^2 \phi(r, t)}{\partial t^2}. \quad (1.49)$$

Any solution of the form:

$$\phi(r, t) = \frac{f(t \pm r/v)}{r} \quad (1.50)$$

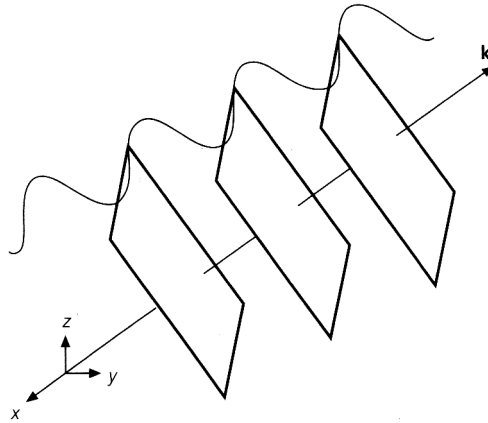


Figure 1.5: Wave front for a harmonic plane wave traveling in the direction indicated by the wave vector \mathbf{k} .

is a spherically symmetric solution to the scalar wave equation. This solution describes spherical waves centered about the origin $\mathbf{r} = 0$, whose amplitude depends on the distance from the origin.

However the solution of eq. (1.50) is not a solution to the homogeneous equation everywhere in space, because it is infinite at $\mathbf{r} = 0$. Thus actually it is a solution of the *inhomogeneous* wave equation:

$$\nabla^2 \phi(r, t) - \frac{1}{v^2} \frac{\partial^2 \phi(r, t)}{\partial t^2} = 4\pi \delta(\mathbf{r}) f(t). \quad (1.51)$$

This equation is used in the study of waves radiated by a seismic source. The fact that the spherical wave solution represents an outgoing wave generated from the origin explains the distance-dependent amplitude factor $1/r$, which has no counterpart for the plane wave solution.

Anyway a plane wave can be regarded as a limit of a spherical wave far from the source, because the spherical wave front becomes almost planar. This approximation is often used in seismology when seismometers are far from the earthquake.

1.2.3 P and S waves

In the previous section we found that the displacement can be separated into a scalar potential corresponding to P waves and a vector potential corresponding to S waves. We will describe now the displacements caused by this types of waves.

Let us start with the P waves and consider a wave propagating in the z direction. The scalar potential for a harmonic plane P wave satisfying eq. (1.40) is:

$$\phi(z, t) = A e^{i(\omega t - kz)}, \quad (1.52)$$

so the resulting displacement is:

$$\mathbf{u}(z, t) = \nabla \phi(z, t) = (0, 0, -ik) A e^{i(\omega t - kz)}, \quad (1.53)$$

which has a non zero component only along the propagating direction. The corresponding dilatation is nonzero:

$$\nabla \cdot \mathbf{u} = -k^2 A e^{i(\omega t - kz)}, \quad (1.54)$$

so a volume change occurs. As the wave propagates the displacements in the direction of propagation cause material to be alternately compressed and expanded. Thus the P wave generated by the scalar potential is called a compressional wave.

By contrast, for the S wave, or shear wave, described by the vector potential:

$$\Psi(z, t) = (A_x, A_y, A_z) e^{i(\omega t - kz)}, \quad (1.55)$$

the resulting displacement is given by the curl:

$$\mathbf{u}(z, t) = \nabla \times \Psi(z, t) = (ikA_y, -ikA_x, 0) e^{i(\omega t - kz)}, \quad (1.56)$$

whose component along the propagation direction z is zero. Thus the only displacement associated with a propagating shear wave is perpendicular to the direction of wave propagation. A shear wave causes no volume change, because the dilatation is zero.

A compressional wave is an example of *longitudinal* wave, because the propagating displacement field varies in the direction of propagation, while a shear wave is an example of a *transverse wave*, as the propagating displacement field varies at right angles to the direction of propagation (fig. 1.6). Moreover for what concerns shear waves only the components A_x and A_y of $\Psi(z, t)$ contribute to the displacement: because each component depends on only one of these terms there can be two independent shear wave fields. Thus shear wave can have two independent polarizations, as in the case for other transverse waves, such as light. In real applications the z axis is taken as the vertical direction: the shear wave polarization direction are defined as SV , for waves with displacement in the $x - z$ plane, and SH , for polarized waves with displacement in the y direction.

Seismometers record horizontal motion in the north-south and east-west directions, which rarely correspond exactly to the SV and SH polarization. As a result data from seismometers are often rotated: the direction connecting a source to the receiver, corresponding to SV displacements, is called the *radial* direction, while the orthogonal direction corresponding to SH displacements is called *transverse* direction. For what concerns the velocity of P and S waves, α and β respectively:

$$\alpha = \left(\frac{\lambda + 2\mu}{\rho} \right)^{1/2} \quad \beta = \left(\frac{\mu}{\rho} \right)^{1/2}, \quad (1.57)$$

we can see that they depend in different ways on the elastic constants of the material: as a result P , or "primary" waves travel faster than S , "secondary" waves: the first wave arriving from an earthquake is always a compressional wave (fig. 1.7). The typical P wave velocity is $5.5Km/s$, while the S wave velocity is $3.2Km/s$.

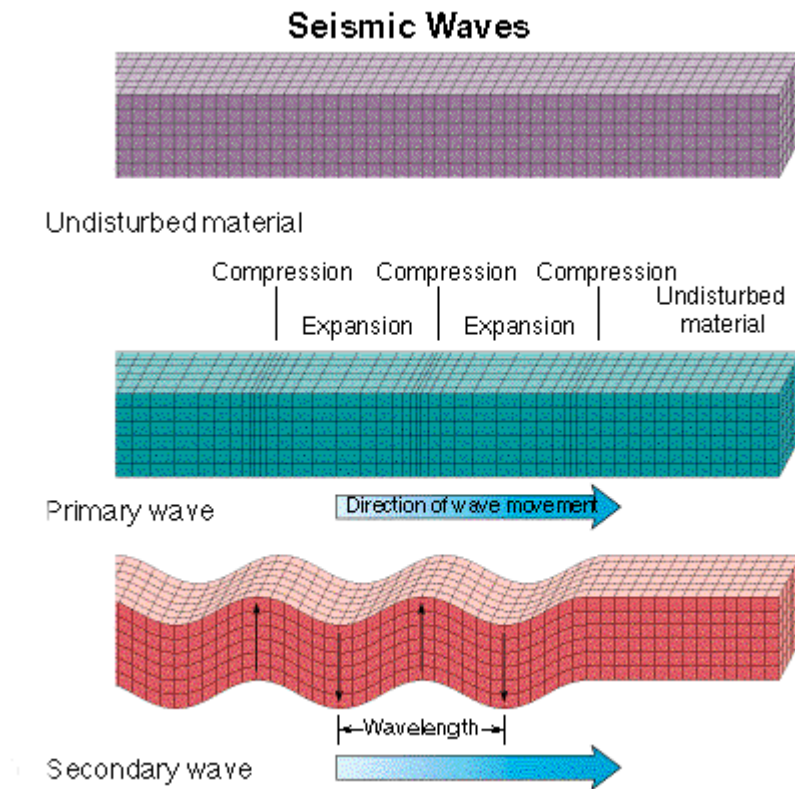


Figure 1.6: A schematic view of displacement for P and S waves

Earthquake sources generate both P and S waves, with the S waves generally significantly larger. To reveal these waves we use a seismometer sensitive to three directions: the z direction, the vertical one, and the (x, y) plane. The first arrival will be a P wave and will appear on the vertical component of the seismogram; the later arrival will be a shear wave and will appear most on the horizontal component of the seismogram.

1.2.4 Energy in P and S waves

Seismic waves transport energy both as kinetic energy and as strain, or potential energy. To find this energy we consider now harmonic plane S and P waves traveling in the z direction.

An SH wave with displacement in the y direction is:

$$u_y(z, t) = B \cos(\omega t - kz), \quad (1.58)$$

where this expression is written directly in terms of displacement, rather than potential. The kinetic energy in a volume V is the integral of the kinetic energy associated with each component of the displacement:

$$KE = \frac{1}{2} \int_V \rho \left(\frac{\partial u_i}{\partial t} \right)^2. \quad (1.59)$$

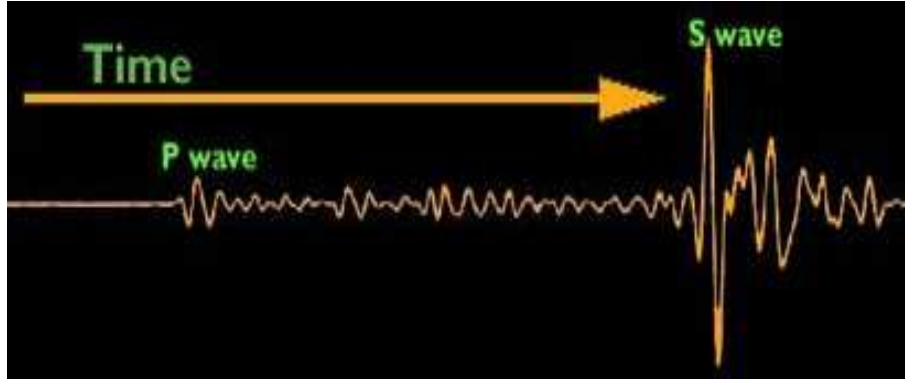


Figure 1.7: A seismogram with P and S waves

Hence for the plane wave in eq. (1.58) the kinetic energy per unit wave front averaged over a wavelength λ is:

$$KE = \frac{1}{2\lambda} \rho B^2 \omega^2 \int_0^\lambda \sin^2(\omega t - kz) dz = B^2 \omega^2 \rho / 4. \quad (1.60)$$

The strain energy is:

$$W = \frac{1}{2} \int_V \sigma_{ij} e_{ij} dV, \quad (1.61)$$

and substituting the only nonzero strain components (e_{32} and e_{23}) and stress components (σ_{32} and σ_{23}) we obtain for the strain energy averaged over a wavelength in the direction of propagation:

$$W = \frac{1}{2\lambda} \int_0^\lambda \mu B^2 k^2 \sin^2(\omega t - kz) dz = B^2 \omega^2 \rho / 4. \quad (1.62)$$

Hence the total energy is:

$$E = KE + W = B^2 \omega^2 \rho / 2, \quad (1.63)$$

and the average energy flux is:

$$\dot{E} = B^2 \omega^2 \rho \beta / 2. \quad (1.64)$$

As we can see the total energy and flux are proportional to the square of the amplitude and the frequency, so, for waves of the same amplitude, the higher frequency wave transports more energy.

Similarly, for a plane P wave propagating in the z direction described by the scalar potential:

$$\phi(z, t) = A e^{i(\omega t - kz)}, \quad (1.65)$$

the real part of the displacement is given by:

$$u_z(z, t) = Ak \sin(\omega t - kz). \quad (1.66)$$

By the use of eq. (1.59) the kinetic energy is:

$$KE = \frac{1}{2\lambda} \rho A^2 k^2 \omega^2 \int_0^\lambda \cos^2(\omega t - kz) dz = A^2 \omega^2 k^2 \rho / 4, \quad (1.67)$$

while the strain energy is:

$$W = \frac{1}{2\lambda} \int_0^\lambda \rho \alpha^2 A^2 k^4 \cos^2(\omega t - kz) dz = A^2 \omega^2 k^2 \rho / 4. \quad (1.68)$$

Hence the total energy is:

$$E = KE + W = A^2 k^2 \omega^2 \rho / 2 \quad (1.69)$$

and the average energy flux in the propagation direction is:

$$\dot{E} = A^2 \omega^2 k^2 \rho \alpha / 2. \quad (1.70)$$

The energy flux gives information about how waves behave when they change media: for example when seismic waves pass from bedrock into soft soil with lower density, their amplitudes increase to conserve energy.

1.2.5 Surface waves

Introduction

Besides P and S waves seismograms are dominated by large longer period waves that arrive after them: these waves are the so called *surface waves* as their energy is concentrated near the earth's surface [4]. At large distances from the seismic source, surface waves are prominent on seismograms for the following reason: the energy of body waves spreads three-dimensionally and decays with distance r approximately as r^{-2} , whereas the energy of surface waves spreads two-dimensionally and decays as r^{-1} .

Two types of surface waves, known as *Love waves* and *Rayleigh waves* after their discoverers, propagate near the earth's surface. Love waves result from SH waves trapped near the surface, while Rayleigh waves are combinations of P and SV motions.

An interesting difference between surface and body waves, due to their different rate of decay, is that surface waves can circle the globe many times after a great earthquake. Another important feature of surface waves is *dispersion*, the fact that waves of different periods travel at different velocities.

As a result the surface wave arrivals are not sharp lines, but are spread out in time.

Rayleigh waves

Rayleigh waves are combination of P and S waves that can exist at the top of a homogeneous halfspace.

To describe them we define the free surface as $z = 0$, measure z downward, and use potentials for waves propagating in the (x, z) plane. We consider only P and SV waves because they can satisfy the free surface boundary conditions and do not interact with SH waves.

For laterally homogeneous medium the displacement for harmonic plane waves propagating in the x direction is can be written as:

$$\mathbf{u} = \mathbf{A} e^{-i\omega(t-px-\eta z)}. \quad (1.71)$$

We know that we can express the displacement in terms of a P wave scalar potential ϕ and a S wave vector potential Ψ , that is:

$$\mathbf{u} = \nabla\phi + \nabla \times \Psi. \quad (1.72)$$

Now we consider plane wave solutions for ϕ and ψ_y , the only part of Ψ that produces SV motion for waves propagating in the x direction:

$$\phi = A e^{i\omega(t-px-n_\alpha z)} \quad (1.73)$$

$$\psi_y = B e^{i\omega(t-px-n_\beta z)}, \quad (1.74)$$

where A and B are the amplitudes of the P and S waves respectively, p is the ray parameter and:

$$n_\alpha = (1/\alpha^2 - p^2)^{1/2} \quad (1.75)$$

$$n_\beta = (1/\beta^2 - p^2)^{1/2} \quad (1.76)$$

are the vertical slownesses of the waves.

The ray paramater p is constant; both P and S waves are assumed to have the same horizontal slowness.

Under these conditions the P wave displacements are:

$$u_x^P = \frac{\partial\phi}{\partial x} = p A i \omega e^{-i\omega(t-px-n_\alpha z)} \quad (1.77)$$

$$u_z^P = \frac{\partial\phi}{\partial z} = n_\alpha A i \omega e^{-i\omega(t-px-n_\alpha z)}, \quad (1.78)$$

while the SV displacements are:

$$u_x^S = \frac{\partial\Psi_y}{\partial z} = n_\beta B i \omega e^{-i\omega(t-px-n_\beta z)} \quad (1.79)$$

$$u_z^S = -\frac{\partial\Psi_y}{\partial x} = -p B i \omega e^{-i\omega(t-px-n_\beta z)}. \quad (1.80)$$

Now we have to impose the boundary conditions at the free surface $z = 0$: here we require both the normal and shear tractions to vanish:

$$\sigma_{x,z} = \sigma_{x,z}^P + \sigma_{x,z}^S = 0 \quad (1.81)$$

$$\sigma_{z,z} = \sigma_{z,z}^P + \sigma_{z,z}^S = 0. \quad (1.82)$$

The explicit expressions for these components of the shear tractions are:

$$\sigma_{x,z}^P = -A(2\mu p n_\alpha)\omega^2 e^{-i\omega(t-px-n_\alpha z)} \quad (1.83)$$

$$\sigma_{z,z}^P = -A[(\lambda + 2\mu)n_\alpha^2 + \lambda p^2]\omega^2 e^{-i\omega(t-px-n_\alpha z)} \quad (1.84)$$

$$\sigma_{x,z}^S = B\mu(p^2 - n_\beta^2)\omega^2 e^{-i\omega(t-px-n_\beta z)} \quad (1.85)$$

$$\sigma_{z,z}^S = B(2\mu n_\beta p)\omega^2 e^{-i\omega(t-px-n_\beta z)}. \quad (1.86)$$

Substituting eq. (1.83)-(1.86) into eq. (1.81) and (1.82) and using the relations $\lambda + 2\mu = \rho\alpha^2$, $\mu = \rho\beta^2$, and $\lambda = \rho(\alpha^2 - 2\beta^2)$ we obtain:

$$A[2p n_\alpha] - B[p^2 - n_\beta^2] = 0 \quad (1.87)$$

$$A[\alpha^2(n_\alpha^2 + p^2) - 2\beta^2 p^2] - B[2\beta^2 n_\beta p] = 0. \quad (1.88)$$

This coupled set of equations describes the free surface boundary condition for P and SV waves with horizontal slowness p .

When $p < 1/\alpha$, there are two real solutions, a positive value of n_α for downgoing P waves and a negative value for upgoing P waves. Similarly, when $p < 1/\beta$, then n_β is real and there exist both downgoing and upgoing SV waves. However a case of interest is where $p > \beta^{-1} > \alpha^{-1}$ and both n_α and n_β are imaginary. In this situation the expression for the displacement is:

$$\mathbf{u}(x, t) = \mathbf{A}e^{i\omega\eta z} e^{-i\omega(t - px)}, \quad (1.89)$$

where we factored out the depth dependence. For imaginary values of η we obtain real values in the exponent and, as a consequence, evanescent waves for which the amplitude grows or decays exponentially as a function of depth. The sign of η is chosen to give the solution that decays away from $z = 0$. For single imaginary values of n_α and n_β the linear system of equation for A and B given in eq. (1.87) and (1.88) has a non trivial solution only when the determinanat vanishes, that is when:

$$\left(2p^2 - \frac{1}{\beta^2}\right)^2 - 4p^2 \left(p^2 - \frac{1}{\alpha^2}\right)^{1/2} \left(p^2 - \frac{1}{\beta^2}\right)^{1/2} = 0. \quad (1.90)$$

This equation is termed the *Rayleigh function* and has a single solution, with the exact value of p depending upon α and β . The corresponding phase velocity, $c = 1/p$, is always slightly less than the shear velocity for a Poisson solid.

By substituting the solutions for p into eq. (1.75), (1.76), (1.87) and (1.88) we may obtain the relative amplitudes of the P and SV components, while substituting into eq. (1.77)-(1.80) will give the vertical and horizontal displacements.

The vertical and horizontal components are out of phase by $\pi/2$: the resulting elliptical motion changes from *retrograde* at the surface to *prograde* at depth, passing through a node at which there is no horizontal motion (fig. 1.8).

Love waves: solution for a single layer

We mentioned that Love waves are formed through the constructive interference of high order SH surface multiples: it is possible to model this type of surface waves as a sum of boby waves.

To see this we consider the propagation of a monochromatic plane wave in the case of a vertical velocity gradient in a laterally homogeneous model: in this situation the rays will curve and the wave fronts are

only locally planar in any homogeneous part of the model. Thus monochromatic plane waves are waves at constant frequency and horizontal wave number $k_x = \omega p$.

The plane wave will turn at the depth where $\beta = 1/p$; along the surface the plane wave will propagate with horizontal slowness p . If the surface bouncepoints are separated by a distance $X(t)$, the travel time along the surface between bouncepoints is given by $pX(p)$. In contrast the travel time along the ray paths is given by $T(p)$ and is a function of the velocity-depth profile.

Because these travel times are not the same, destructive interference will occur except at certain fixed frequencies. Along the surface, the phase (0 to 2π) of a harmonic wave will be delayed by $\omega pX(p)$. The phase along the ray path is delayed by $\omega T(p) - \pi/2$, where last factor comes from the WKJB approximation. The requirement for constructive interference is:

$$\omega pX(p) = \omega T(p) - \frac{\pi}{2} - 2n\pi. \quad (1.91)$$

Rearranging eq. (1.91) we obtain:

$$\omega = \frac{2n\pi + \pi/2}{\tau(p)}, \quad (1.92)$$

where $\tau(p) = T(p) - pX(p)$ represents the delay time. The wave travels along the surface at velocity $c = 1/p$. We derive now an exact equation for Love wave dispersion within an homogeneous layer. Let us consider a surface layer overlying a higher velocity half-space with thickness h . We can still apply eq. (1.92), replacing the approximate $\pi/2$ phase shift with the phase shift ϕ_{SS} , resulting from the SH reflection off the bottom of the layer:

$$\omega = \frac{2n\pi + \phi_{SS}}{\tau(p)}. \quad (1.93)$$

The delay time $\tau(p)$ is given by:

$$\tau(p) = 2h\sqrt{1/\beta_1^2 - p^2}, \quad (1.94)$$

where β_1 is the shear velocity in the top layer. For postcritical reflections (reflections at angles bigger than the *critical angle*) it can be shown that:

$$\phi_{SS} = 2 \tan^{-1} \left[\frac{\mu_2 \sqrt{p^2 - 1/\beta_2^2}}{\mu_1 \sqrt{1/\beta_1^2 - p^2}} \right]. \quad (1.95)$$

Substituting eq. (1.94) and (1.95) into eq. (1.93) we have:

$$\tan \left[h\omega \sqrt{1/\beta_1^2 - p^2} \right] = \frac{\mu_2 \sqrt{p^2 - 1/\beta_2^2}}{\mu_1 \sqrt{1/\beta_1^2 - p^2}}. \quad (1.96)$$

This equation defines the dispersion curve for Love wave propagation within the layer: it has no analytical solution, so the phase velocity $c = 1/p$ must be determined numerically.

The phase velocity varies between β_1 and β_2 ; for every value of c there are multiple values of ω because of the periodicity in the tangent function. The smallest value of ω defines the fundamental mode, the second smallest is the first higher mode and so on. A schematic view of the displacement for Love waves is shown in fig. 1.8.

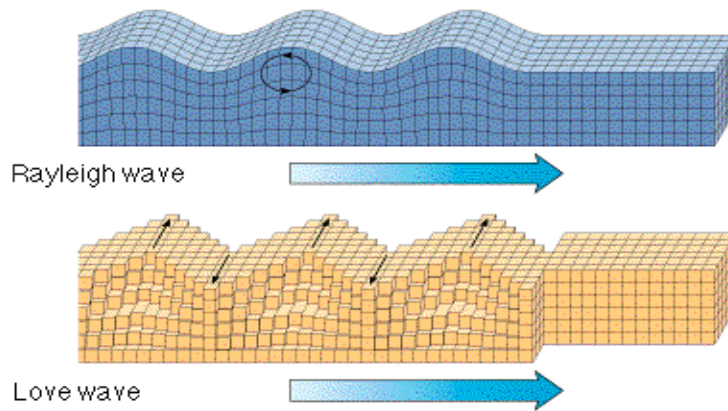


Figure 1.8: A schematic view of the displacements for Love and Rayleigh waves

1.2.6 Principles for seismic waves propagation

In the previous sections we have analyzed both body and surface seismic waves and their main features. In this subsection we want to briefly describe some important principles in wave propagation: Snell's law, Fermat's principle, Huygen's principle and diffraction, dispersion. The first three principle are usually applied for P and S waves, while dispersion is typical of surface waves. Some of these principles were born in the field of optics, to study the propagation of electromagnetic waves, but remain valid for seismic waves, too.

Fermat's principle

Fermat's principle states that the ray paths between two points are those for which the travel time is an extremum, a minimum or maximum, with respect to the nearby possible paths. A useful way to characterize a wave's ray path is via its *ray parameter* p :

$$p = \sin \frac{i}{v}, \quad (1.97)$$

where i is the angle of incidence of either a P or an S wave and v is the corresponding velocity.

So, if we want to know the behaviour of seismic waves, we can consider the ray paths associated with them: this approach is called *geometric ray theory* and is widely used because it greatly simplifies the analysis of wave propagation.

The most obvious application of rays is for computing travel times. To find when a plane wave generated

at one position will arrive at another we use the travel time, which is the length of the ray path divided by the velocity: thus, if waves follow complicated paths, their travel time is the sum of the travel times for each portion of the ray path.

Snell's law

Snell's law states the relation between the angles of incidence for transmitted and reflected harmonic plane waves at the interface between two medium. Let us consider an interface which separates medium 1 with wave velocity α_1 from medium 2 with wave velocity α_2 .

A wave incident from medium 1 generates reflected and transmitted waves. Let i_1 and i_2 be the angle of the incident beam respect to the vertical direction in medium 1 and the angle of the reflected beam in medium 2, respectively. Snell's law states that:

$$\frac{\alpha_1}{\sin i_1} = \frac{\alpha_2}{\sin i_2}. \quad (1.98)$$

This means that the ratio of the sine of the angle of incidence for each wave to the corresponding velocity is constant.

Snell's law can be derived from Fermat's principle, just considering the possible ray paths between two points in two different medium: these ray paths can be parametrized by the point x where they cross the interface, and the travel time with them. We then differentiate the travel time respect to x to find the path for which it is an extremum: we obtain the same result stated in Snell's law.

Huygen's principle and diffraction

Huygen's principle gives another way of thinking about phenomena already discussed, but sometimes not completely explained. For example in some applications treating propagating waves as geometric rays fails to explain what we observe.

According to Huygen's principle each point on a wave front is considered to be a *Huygen's source* that gives rise to another circular wave front: these wave fronts interfere constructively to give a circular wave front, and destructively everywhere else.

This principle well explains the phenomenon of *diffraction*, in which waves bend around obstacles. An analogous process occurs with shear waves that cannot pass through the liquid outer core, and so diffract around it.

For evaluating the amplitude of the diffracted waves we would require to go beyond Huygen's principle, but we can describe a simple model. Let us consider a slit with width d . Waves from either side of the slit will be out of phase by 90° and so interfere destructively at distance D when the path difference is a half wavelength. Hence the amplitude will be zero at a distance x_0 , or an angle θ , from the middle of the slit.

By this condition:

$$\lambda/2 = d \sin \theta \approx dx_0/D, \quad (1.99)$$

assuming $D \gg d$. Thus the amplitude decay from its maximum at $\theta = 0$ to zero at $x_0 = \lambda D/2d$. This slit illustrates general properties of diffraction, because diffraction around an obstacle is in many ways similar.

An important point is that diffraction depends on the wavelength, so longer wavelengths have broader lobes and thus are more affected by diffraction. Specifically the diffraction depends on the ratio of the wavelength to the slit width: if the slit is less than a half wavelength wide, the side lobes vanish. Hence, if an obstacle is less than a half wavelength wide, waves impinging on it are insensitive to the details of its structure; conversely, if the slit is very wide compared to the wavelength, diffraction occurs only at the slit's edges.

Similar effects occur when wave fronts encounter a circular (or spherical) obstacle: geometric ray theory would predict that no energy will arrive behind the obstacle. In reality the wave diffracts around the sphere, closing the gap behind it.

Dispersion

Dispersion is a physical phenomenon according to which waves of different frequencies propagate at different speeds. To best view this process we use the Fourier analysis. Let us express a displacement field $u(x, t)$ as an integral over harmonic plane waves of all frequencies:

$$u(x, t) = \frac{1}{2\pi} \int_{-\infty}^{+\infty} A(\omega) e^{i[\omega t - k(\omega)x + \phi_i(\omega)]} d\omega. \quad (1.100)$$

In this formulation, the wavenumber $k(\omega)$ and the amplitude $A(\omega)$ of each harmonic plane wave are functions of the angular frequency. At each angular frequency the phase:

$$\Phi(\omega) = \omega t - k(\omega)x + \phi_i(\omega) \quad (1.101)$$

has two parts. The term $\omega t - k(\omega)x$ gives the variation in the phase due to the propagation of the harmonic wave. Hence, the propagation depends on both time (ωt) and space ($k(\omega)x$). Surface of constant phase travel with a *phase velocity*:

$$c(\omega) = \omega/k(\omega). \quad (1.102)$$

That may vary as a function of angular frequency.

The other phase term $\phi_i(\omega)$ includes effects such as the initial phase of the wave when it was generated by a seismic source, which depends on the earthquake focal mechanism.

If the harmonic waves of different angular frequencies propagate with different phase velocities, the velocity at which a *wave group* propagates differs from the phase velocity at which individual harmonic waves travel. To find the group velocity of energy propagation in the angular frequency band between

$\omega_0 - \Delta\omega$ and $\omega_0 + \Delta\omega$, we have to approximate the wave number $k(\omega)$ by the first term of Taylor series about ω_0 :

$$k(\omega) = k(\omega_0) + \frac{dk}{d\omega}(\omega - \omega_0). \quad (1.103)$$

Substituting eq. (1.103) in eq. (1.100) we obtain the group velocity as a function of the angular frequency:

$$U(\omega) = \left. \frac{d\omega}{dk} \right|_{\omega_0}. \quad (1.104)$$

This approximation to the first term in Taylor series could not be sufficient, but is generally valid for seismic waves. At any angular frequency, the group velocity is related to the phase velocity by:

$$U(\omega) = \frac{d\omega}{dk} = \frac{d(ck)}{dk} = c + k \frac{dc}{dk}. \quad (1.105)$$

The same equation in terms of wavelength is expressed as:

$$U \approx c - \lambda \frac{dc}{d\lambda}. \quad (1.106)$$

If the wave is not dispersive, different wavelengths travel at the same phase velocity, so $\frac{dc}{d\lambda} = 0$, and the phase and group velocity are equal. For a dispersive wave, such as a Love wave the group velocity can be found from the dispersion relation. If the dispersion relation is:

$$f(\omega, k) = 0, \quad (1.107)$$

the group velocity results:

$$U(\omega) = \frac{d\omega}{dk} = - \left(\frac{\partial f}{\partial k} \right)_{\omega} / \left(\frac{\partial f}{\partial \omega} \right)_{k}. \quad (1.108)$$

1.2.7 Normal modes of the Earth

Motivation

We can describe the displacement resulting from the application of a force to a body in two ways: as waves propagating through the body or as the sum of standing waves, called *normal modes*.

Both of these descriptions are equivalent because all the features of wave propagation, such as velocity and amplitudes of reflected and transmitted waves, come out the same. This concept is called *mode-wave duality* and is useful in seismology because the two formulations provide different insights and jointly lead to deeper understanding.

Most studies do not use the normal mode approach because normal mode calculations are more complicated than those for rays and, by representing all seismic waves simultaneously, mode solutions do not select specific seismic phases.

Anyway the normal mode approach has the advantage that by the analysis in the Fourier domain of seismological records we can identify the various modes and use them to constrain Earth's structure. Normal

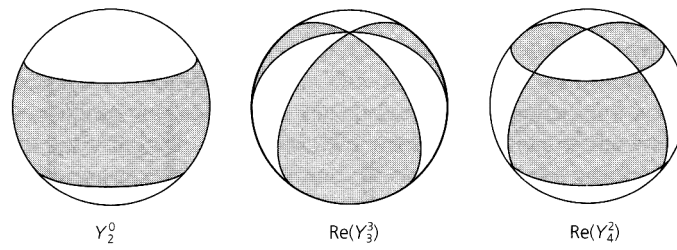


Figure 1.9: Examples of spherical harmonics

modes are also able to examine Earth's properties, such as shear response in the inner core, that have not yet been observed directly with body waves.

Neither formulation is more real, both are mathematical ways of representing the displacement, which is the physical quantity.

Modes of a sphere and spherical harmonics

Normal modes are specified by their eigenfrequencies and eigenfunctions. The most important properties of the eigenfunctions of any vibrating system are:

- They are complete: any wave motion within the Earth may be expressed as a sum of normal modes with different excitation factors
- They are orthogonal in the sense that the integral over the volume of the Earth of the product of any two eigenfunctions is zero. This implies that the normal mode representation of wave motion is unique

The Earth is a finite spherical body in which all wave motions must be confined: to calculate normal modes we have to describe wave propagation in a three dimensional spherical solid, so we write the displacement vector $\mathbf{u}(r, \theta, \phi)$ that satisfies the equation of motion as a function of the radius r and surface position (θ, ϕ) . We write the displacement as a normal mode sum:

$$\mathbf{u}(r, \theta, \phi) = \sum_n \sum_l \sum_m {}_n A_l^m y_l(r) \mathbf{x}_l^m(\theta, \phi) e^{i_n \omega_l^m t}. \quad (1.109)$$

As we can see each mode is described by three indices: the eigenfrequency ${}_n \omega_l^m$ depends on all three, while the spatial behaviour is described by the radial eigenfunction ${}_n y_l(r)$, which is a scalar, and by the surface eigenfunction $\mathbf{x}_l^m(\theta, \phi)$, which is a vector. Moreover the sum depends on the weights for each eigenfunction, ${}_n A_l^m$, which are excitation amplitudes that depend on the seismic source.

For what concerns the shape of the normal modes it can be shown that for a spherically symmetric solid there are two distinctly different types of modes: *spheroidal modes*, which are analogous to *P/SV* and Rayleigh wave motion, and *toroidal modes*, which are analogous to *SH* and Love wave motion.

The Earth's departures from spherical symmetry mean that this separation is not complete, but it is a very good first-order approximation. Toroidal modes include no radial motion and are sensitive only to shear velocity, whereas spheroidal modes have both radial and horizontal motion and are sensitive to both compressional and shear velocities. Spheroidal mode observations at long periods are also sensitive to gravity and provide the best direct seismic constraints on Earth's density structure.

The lateral variations in normal mode eigenfunctions are best described in terms of *spherical harmonics*, which provide an orthogonal set of basis functions on a spherical surface. A spherical harmonic function may be expressed as Y_l^m , where l is termed the *angular order number* and m is the *azimuthal order number*:

$$Y_l^m(\theta, \phi) = (-1)^m \left[\left(\frac{2l+1}{4\pi} \right) \frac{(l-m)!}{(l+m)!} \right]^{1/2} P_l^m(\cos \theta) e^{im\phi}, \quad (1.110)$$

where $P_l^m(\cos \theta)$ are the *associated Legendre functions*. The *azimuthal order* m varies over $-l \leq m \leq l$.

Earth's normal modes are specified in terms of the spherical harmonic numbers l and m and a *radial order number* n that describes the number of zero crossings in radius that are present.

Some spherical harmonics are shown in fig.1.9.

Toroidal modes are thus designed as ${}_nT_l^m$ and spheroidal modes as ${}_nS_l^m$. The solutions for $n = 0$ are called the fundamental modes; the solutions for $n > 0$ are termed overtones. For a spherically symmetric Earth the eigenfrequencies at constant n and l are identical for all values of m , and it is common to denote modes only by their radial and angular order numbers, as ${}_nT_l$ and ${}_nS_l$.

The explicit expression for the eigenfunctions of the toroidal modes in terms of the spherical harmonics is:

$$T_l^m = \left(0, \frac{1}{\sin \theta} \frac{\partial Y_l^m(\theta, \phi)}{\partial \phi}, \frac{-\partial Y_l^m(\theta, \phi)}{\partial \theta} \right). \quad (1.111)$$

Analogously the explicit expression for the eigenfunctions of the spheroidal modes in terms of the spherical harmonics is:

$$S_l^m = \left(0, \frac{\partial Y_l^m(\theta, \phi)}{\partial \theta}, \frac{1}{\sin \theta} \frac{\partial Y_l^m(\theta, \phi)}{\partial \phi} \right). \quad (1.112)$$

The fundamental spheroidal mode ${}_0S_0$ is termed the *breathing mode* and represents a simple expansion and contraction: it has a period of about 20 minutes. ${}_0S_2$ has a period of about 54 minutes and represents an oscillation between an ellipsoid of horizontal and vertical orientation. The toroidal mode ${}_0T_0$ represents a simple change in the Earth's rotation rate, while the toroidal mode ${}_0T_1$ has a period of about 44 minutes and describes a relative twisting motion between the northern and southern hemispheres.

The definitive experimental observations of these modes occurred in 1960 after the great earthquake in Chile, when a few dozen of modes were identified.

1.3 Seismometers and seismological networks

1.3.1 Introduction

In this section we will introduce some ideas about *seismometry*, the design and development of seismic instrumentation [2]. Although we informally call such system seismometers, the *seismometer* is actually the sensor recording ground motion, and thus a key component of the entire *seismograph* system, which also contains amplifying, timing and recording components. The final product, a record of ground motion, is called a *seismogram*.

From linear systems theory we know that a seismogram is not an exact representation of the ground motion. Seismograms depend upon the seismometer and the rest of the seismograph system, because the sensitivities of the seismometers vary with the frequency of the ground motion recorded. Moreover, seismometers can record ground motion as displacement, velocity, acceleration or combinations of these.

Once recorded, distributing seismic data is crucial, because the data are of no use until they are available for study. Hence seismology has long been a leader among the sciences in developing public data distribution. This tradition began a century ago from the necessity of observations at many sites to locate and study earthquakes. The first major attempt to publish seismically recorded arrival times was the bulletin of the Bureau Central International de Seismologie (BCIS), which began in 1904. The International Seismological Summary (ISC) began publication in 1913, and eventually became the *Bulletin of the International Seismological Centre*, now an authoritative source of earthquake location. The sharing of data started in modern era in 1962 with the World Wide Standardized Seismograph Network (WWSSN).

Today high quality digital global seismic data are available through the Federation of Digital Broad-Band Seismographic Network (FDSN).

Data and results such as earthquake locations are also provided by national and regional data centers.

As much as any development in theory of seismometry, this free access to data and software is responsible for the remarkable growth of the field within the past century.

1.3.2 The damped harmonic oscillator

The basic problem of seismometry is how to measure the motion of the ground using an instrument that is also on the ground. The traditional solution is to use an inertial system, a pendulum, so that the motion of the pendulum is out of phase with the ground motion. Three orthogonal seismometers (vertical, north-south, east-west) can give a three dimensional record of ground motion. A schematic vertical seismometer is shown in fig.1.10. The key elements of the system are the mass, the spring, and a dashpot, or damping device.

This mechanical seismometer system is a damped simple harmonic oscillator. If the spring equilibrium length in the absence of ground motion is ξ_0 , the spring exerts a force proportional to its extension from equilibrium $\xi(t)$, times a spring constant k . The dashpot, with damping constant d , exerts a force propor-

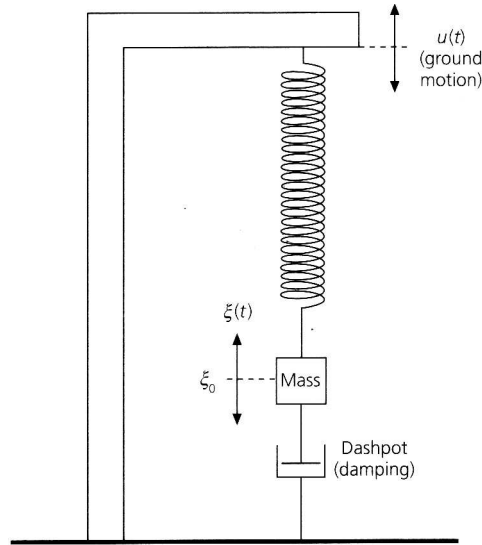


Figure 1.10: Pendulum seismograph consisting of a mass, a spring, and a dashpot.

tional to the velocity between the mass m and the earth. In this condition the equation for the ground motion is:

$$\ddot{\xi} + 2\epsilon\dot{\xi} + \omega_0^2\xi = -\ddot{u}, \quad (1.113)$$

where $\omega_0 = \sqrt{k/m}$ is the natural frequency of the undamped system, while $\epsilon = d/(2m)$ represents the damping. To solve this equation we assume that:

$$u(t) = e^{-i\omega t} \quad \xi(t) = X(\omega)e^{-i\omega t} \quad (1.114)$$

and substitute eq. (1.114) into eq. (1.113) obtaining:

$$X(\omega) = -\omega^2/(\omega^2 - \omega_0^2 + 2\epsilon i\omega), \quad (1.115)$$

which is the instrument response produced by a ground motion $e^{i\omega t}$.

$X(\omega)$ is a complex number and can be written in terms of the amplitude and phase responses:

$$X(\omega) = |X(\omega)| e^{i\phi(\omega)}, \quad (1.116)$$

where

$$|X(\omega)| = \omega^2/[(\omega^2 - \omega_0^2)^2 + 4\epsilon^2\omega^2]^{1/2} \quad (1.117)$$

and

$$\phi = -\tan^{-1} \frac{2\epsilon\omega}{\omega^2 - \omega_0^2} + \pi. \quad (1.118)$$

As we can see in fig.1.11 as the angular frequency of the ground motion, ω , approaches the natural frequency of the pendulum, ω_0 , the amplitude response is large: this effect, called *resonance*, means that the seismometer responds best to ground motion near its natural period.

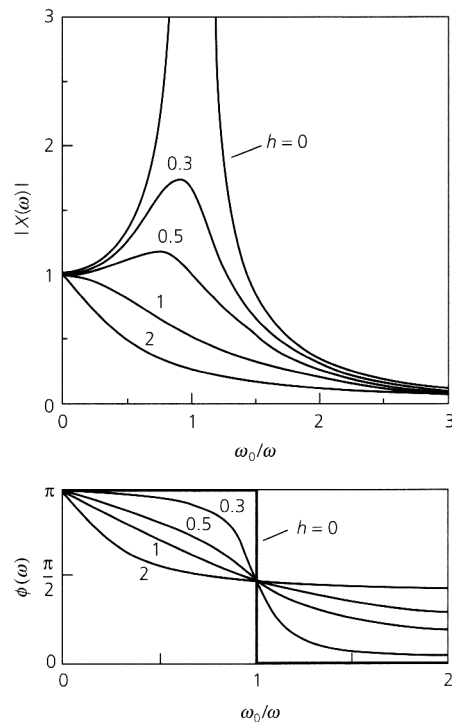


Figure 1.11: Amplitude response $|X(\omega)|$ and phase delay $\phi(\omega)$ for pendulum seismometer.

For frequencies much greater than the natural frequency, $\omega \gg \omega_0$, $|X(\omega)| \rightarrow 1$ and $\phi(\omega) \rightarrow \pi$, so the seismometer records the ground motion, but with the sign reversed. To see why this occurs consider eq. (1.113): for $\omega \gg \omega_0$ the $\ddot{\xi}$ term is the largest term on the left side, so $\ddot{\xi}$ approximately equals \ddot{u} . Thus the seismometer responds to *ground displacement*. On the other hand for frequencies much less than the natural frequency $|X(\omega)| \rightarrow \omega^2/\omega_0^2$ and $\phi(\omega) \rightarrow 0$. Hence, in this case the seismometer responds to *acceleration*, as can be seen from eq. (1.113), because the $\omega_0^2\xi$ term is dominant, so ξ is proportional to \ddot{u} .

The shape of the instrument response depends on the damping factor $h = \epsilon/\omega_0$. For $h = 0$ the system is undamped, and the amplitude response is peaked around the resonant frequency, $\omega = \omega_0$. The seismometer amplifies ground motion with periods near to its natural period. As damping is increased, the curve is smeared out.

Thus the natural period and damping are used to design a seismometer to record ground motion in a particular period range.

1.3.3 Earth noise

An important consideration in designing seismometers is earth noise, which sets a limit to level of detection: thus studies using seismic data in many applications must consider the signal-to-noise ratio.

Many factors contribute to seismic noise, including solar and lunar tides within the solid earth, fluctua-

tions in temperature and atmospheric pressure, storms, human activities, and ocean waves. These factors are constantly at work, so the crust is continually reverberating. Most of the noise occurs at periods between 1 and 10 seconds: such waves, called *microseisms*, are shown in fig.1.12 (*top*). Even before the first waves arrive from the earthquake shown, the seismogram shows a roughly constant level of seismic energy (*center*). The spectrum shows that most of this noise is in the frequency range of 0.1 – 0.2 Hz (*bottom*). The primary source for these microseisms is thought to be ocean waves: thus the ocean island stations are the noisiest.

How a seismometer is deployed has a great effect upon the noise that it can record. Most sources of noise decrease away from the surface, so permanent seismometer installations are often in boreholes.

For portable seismometers, burying them even half a meter beneath the surface greatly reduces noise from daily temperature fluctuations. Rain generates high frequency noise, and wind can generate severe long period noise. Human activity causes significant ground noise, so seismologists deploying temporary stations face a trade off between the convenience of building basements (constant temperature, security, no flooding) and the lower noise of remote sites.

1.3.4 Seismometers, seismographs and seismological networks

Seismometers record ground motions ranging from large high frequency acceleration near an earthquake to small ultra-long-period normal mode signals.

Because no single seismograph can do this, different instruments have evolved to handle the different *dynamic ranges* and *frequency ranges* of seismic waves.

Displacements associated with earthquakes may be as low as 10^{-10} m, whereas teleseismic displacements from a magnitude 8 earthquake may be on the order of 10^{-1} m, and displacements near a large earthquake can be much greater. Thus the dynamic range of seismometry is at least 180 dB. Similarly, the frequency range of seismometers spans seven orders of magnitude from Earth tides (0.000023 Hz) to ultra-high frequencies (greater than 200 Hz) for very shallow structure investigations.

The earliest attempts to record the motions of earthquakes used *seismoscopes*, which differ from seismographs in that they record ground motion without time information. The first known seismoscope, built by the Chinese astronomer Chang Heng in about AD 132, consisted of a pendulum inside a 6 ft-diameter jar. Eight dragon's heads with metal balls in their mouths were placed around the rim of the jar, so the balls would drop in the direction from which seismic waves arrived.

Early seismometers were purely mechanical instruments like that described in the previous subsection. Seismometry began around 1875 with the designs of F. Cecchi, and developed rapidly: the first teleseismic recording was by a seismograph in Postdam of a Japanese earthquake in 1889.

By the start of the twentieth century a global network of more than 40 seismographs was in operation. Such instruments often produced excellent data but their magnification were low, only about 100 times the actual ground motion.

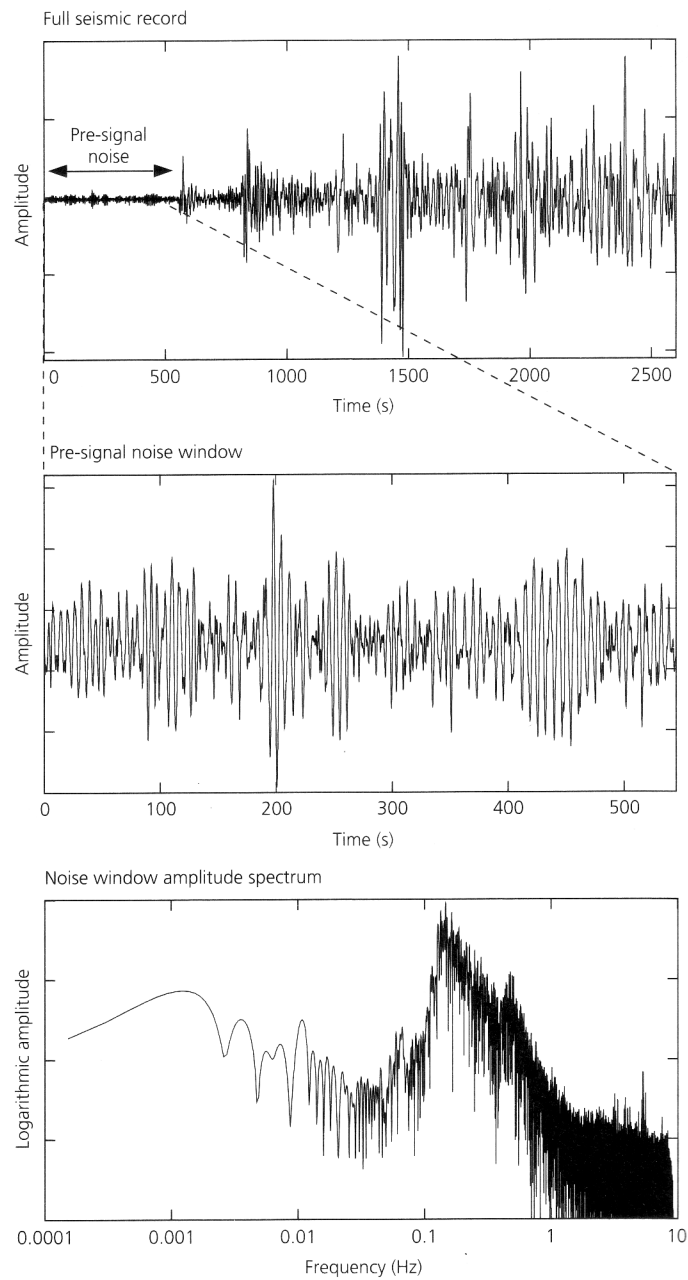


Figure 1.12: Demonstration of seismic noise on a broadband seismogram in Hudson, New York, from an April 7, 1995, Tonga earthquake.

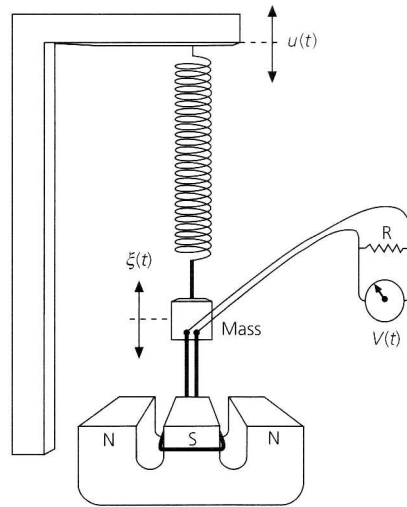


Figure 1.13: Schematic illustration of an electromagnetic seismograph, in which the mass is coupled to an electromagnetic transducer. Motions of the mass move the coil through the magnetic field, generating an electric current. The voltage across the coil is proportional to the relative velocity between the mass and the magnet.

Higher magnifications are achieved by using electromagnetic instruments. The motion of the pendulum relative to the frame is measured by moving a coil attached to the mass through the magnetic field produced by a magnet fixed to the seismometer frame. The voltage produced in the coil is proportional to the time rate of change of the magnetic field, and thus to the velocity of the mass relative to the frame (fig. 1.13). The sensitivity can be increased by feeding the output from this sensor into a galvanometer, a wire suspended by a thin fiber such that it is deflected by the current produced by the sensor (fig. 1.14). A mirror is attached so that ground motion deflects the mirror and thus changes the position of a beam of light hitting a piece of photographic paper.

Thus the response of an electromagnetic analog seismometer system is a combination of the pendulum, transducer, and galvanometer responses. The pendulum response is proportional to ω^2 for $\omega < \omega_s$, the pendulum frequency. The transducer response is proportional to ω because it responds to the velocity, the derivative of displacement. The galvanometer response falls as ω^{-2} for $\omega > \omega_g$, the galvanometer frequency. Thus the response of an electromagnetic seismometer can be shaped by choosing the pendulum and galvanometer frequency.

Two classic electromagnetic instruments used heavily for years were the World Wide Standardized Seismograph Network (WWSSN) long- and short-period instruments. The long-period (LP) instrument had a pendulum period of 15 s and a galvanometer period of 100 s. The short-period instrument had a 1 s pendulum and a 0.75 s galvanometer. Each WWSSN station had three LP and three SP instruments oriented

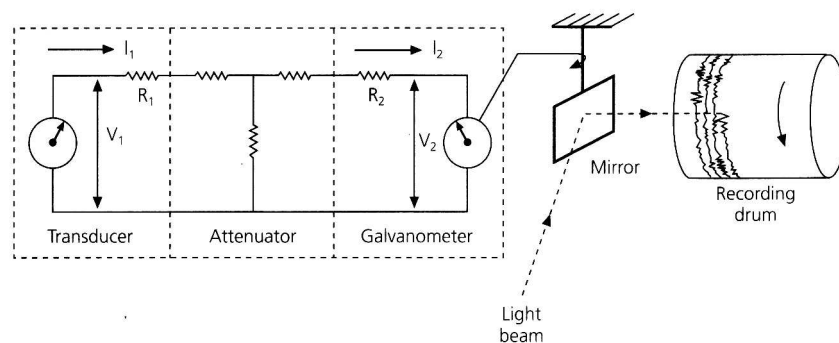


Figure 1.14: Coupling of the transducer of an electromagnetic seismograph to a galvanometer, which deflects a mirror and thus a light beam, causing a time history of the voltage and thus the mass movements to be recorded on a photographic paper.

to record ground motion in the vertical, east-west and north-south directions. Anyway using WWSSN data was cumbersome: the records were digitized by taping them to a special table that contained a grid of electromagnetic wires and then tracing the seismogram with a cursor. After digitization the seismogram was interpolated to a desired sampling rate.

The replacement of analog seismographs by digital broadband instruments has important advantages. The newer seismometers provide better data over a broader frequency band and the digital data are available via magnetic tape, compact disk or the Internet.

One of the more recent digital seismological system was the instrument used by the International Deployment of Accelerometers (IDA) shown in fig.1.15. The sensor is a force-feedback gravimeter that detects vertical ground motion by the resulting change in gravity. The gravimeter mass is connected to the center plate of a capacitor whose outer plates are fixed; as the mass moves, the voltage between the center plate and the outer plates is proportional to the displacement. A 5 KHz alternating voltage applied to the outer plates is amplitude modulated by the lower frequency seismic signal. The modulated signal is fed to an amplifier that generates a voltage proportional to the displacement of the mass. This signal then goes to an integrator circuit whose output is proportional to the acceleration of the mass: this is the seismic system's output. The voltage is also fed back to the outer capacitor plates to stabilize the system and increase linearity.

This force-feedback is an important feature of modern seismometers and provides a greater dynamic range because the mass does not move as far to record large amplitudes. Because this instrument can record a static displacement it has a flat response out to frequencies approaching $\omega = 0$. Such long-period response is valuable for studying normal modes and large earthquakes.

The most versatile of the current digital seismometers are broadband systems that record ground motion over a very broad frequency range. At present the primary broadband seismometers are the Steckheisen

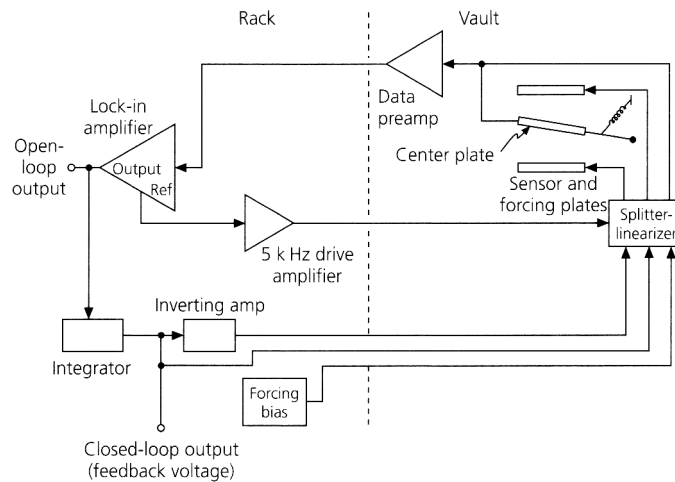


Figure 1.15: Block diagram of the sensing and feedback electronics of an IDA gravimeter recording system.

STS-1 STS-2 and Guralp-3T, which use force-feedback technology to allow large dynamic and frequency ranges.

A variety of specialized seismic instruments are also used.

Strainmeters, which will be described in detail in next chapter, are used to measure gradual displacements, especially near faults and volcanoes. Such instruments are technically challenging to build, and have taken unusual forms.

Whereas strainmeters record minute displacements there exist strong motion sensors, also called accelerometers, which record acceleration up to $2g$, without breaking or going off scale.

A major advance in seismometry has been in timing, which has long been a difficulty. In early days of seismology, timing errors played a large part in the mislocation of the earthquakes. However seismometers now receive time signals from GPS satellites, whose atomic clocks are accurate to billionth of a second.

At the end of this section we want to tell some words about seismic networks.

Most seismic experiments require multiple seismometers that are deployed in networks or arrays. Different applications, such as studying regional and global earth structure, resource exploration, seismicity monitoring, or identifying nuclear tests, lead to different deployment geometries.

Thus deployments of seismometers are often divided into global networks, arrays and regional networks. Global networks are used to study global pattern of seismicity, plate tectonics, mantle convection, and earth structure. For these purposes seismometers should ideally be spread all over the world (a real example of global network is shown in fig.1.16).

The antithesis of a global network is a local array, where a set of seismometers is deployed with a geometry chosen for a particular goal. Arrays data are often analyzed for a single entity, as in refraction and reflection

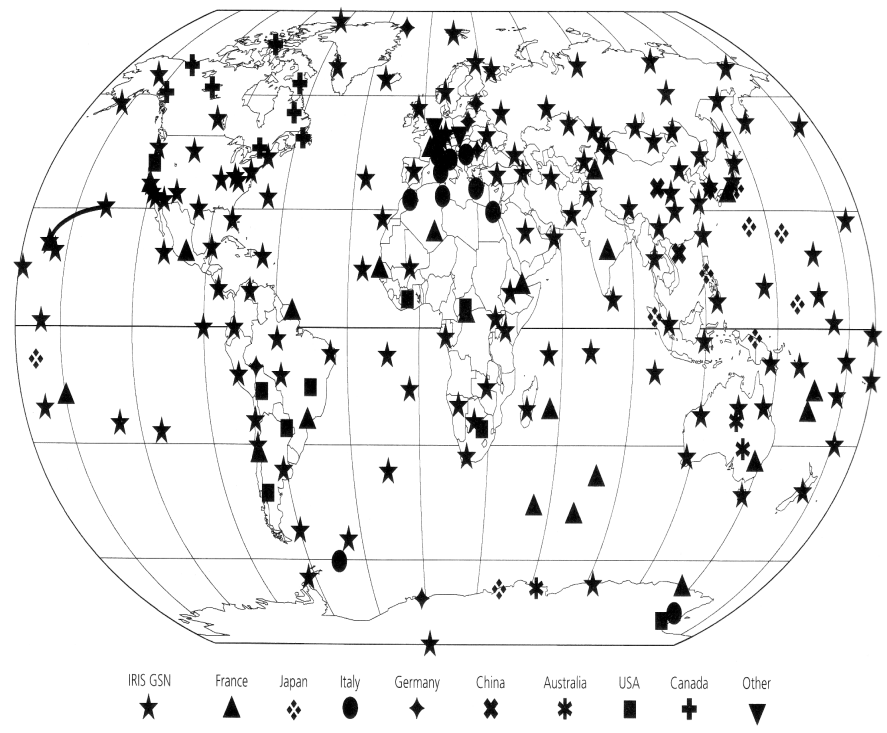


Figure 1.16: Station map of the Federation of Digital Broad-Band Seismographic Network.

studies.

Between global networks and local arrays are regional networks, which usually focus on seismicity or structure of a particular region.

Chapter 2

Interferometric seismic sensors

Laser interferometry is currently one of the most sensitive methods for small displacement measurements. In this chapter we will analyze the basic theory of optical interference and of Fabry Perot interferometers. Interferometers have already been used since 1960 for various geophysical purposes. We will give a brief description of some interesting applications for Michelson and for Fabry Perot interferometers in seismic noise measurements, before than describing the particular application developed in this thesis work.

2.1 The Fabry Perot interferometer

In this section we will describe in detail the Fabry Perot resonator: the simplest configuration for a resonator consists of two mirrors with a given radius of curvature and a laser beam bouncing back and forth into it.

Thus we will introduce the phenomenon of interference, the nature of laser beams and their propagation laws before then describing the Fabry Perot cavity.

2.1.1 Optical interference

If light from a source is divided by suitable apparatus into two beams which are then superposed, the intensity in the region of superposition is found to vary from point to point between maxima, which exceed the sum of the intensities in the beams, and minima, which may be zero: this phenomenon is called *interference*. Suppose that two monochromatic waves [5] \mathbf{E}_1 and \mathbf{E}_2 propagating in the z direction and linearly polarized in the x direction are superposed at some point P . The total electric field at P is:

$$\mathbf{E} = \mathbf{E}_1 + \mathbf{E}_2, \quad (2.1)$$

so that

$$\mathbf{E}^2 = \mathbf{E}_1^2 + \mathbf{E}_2^2 + 2\mathbf{E}_1 \cdot \mathbf{E}_2. \quad (2.2)$$

Hence the total intensity at P is:

$$I = I_1 + I_2 + J_{12}, \quad (2.3)$$

where

$$I_1 = \langle \mathbf{E}_1^2 \rangle, \quad I_2 = \langle \mathbf{E}_2^2 \rangle \quad (2.4)$$

are the intensities of the two waves and

$$J_{12} = \langle \mathbf{E}_1 \cdot \mathbf{E}_2 \rangle \quad (2.5)$$

is the *interference term*. The total intensity I can be also expressed as:

$$I = I_1 + I_2 + 2\sqrt{I_1 I_2} \cos \phi, \quad (2.6)$$

where

$$\phi = \frac{2\pi}{\lambda_0} \Delta S \quad (2.7)$$

is the phase difference between the two waves, λ_0 the wavelength of the light and ΔS the difference between the optical paths for the two waves from their source to P .

Evidently there will be the maxima of intensity:

$$I_{\max} = I_1 + I_2 + 2\sqrt{I_1 I_2} \quad (2.8)$$

when

$$|\phi| = 0, 2\pi, 4\pi, \dots \quad (2.9)$$

and minima of intensity

$$I_{\min} = I_1 + I_2 - 2\sqrt{I_1 I_2} \quad (2.10)$$

when

$$|\phi| = \pi, 3\pi, \dots \quad (2.11)$$

What we have described is the simple case of the two-beam interference. When we consider multiple-beam interference we can repeat the above considerations superposing in some way a generic number n of waves.

This can be done illuminating a plane parallel transparent plate with a plane wave of monochromatic light: what will happen? A part of the incident light will be reflected and another complementary part of the light will be transmitted by the plate, according to the formulas:

$$I_r = \frac{4R \sin^2 \frac{\phi}{2}}{(1-R)^2 + 4R \sin^2 \frac{\phi}{2}} I_i \quad (2.12)$$

and

$$I_t = \frac{T^2}{(1-R)^2 + 4R \sin^2 \frac{\phi}{2}} I_i \quad (2.13)$$

where R and T represent respectively the reflectivity and transmittivity of the plate surfaces.

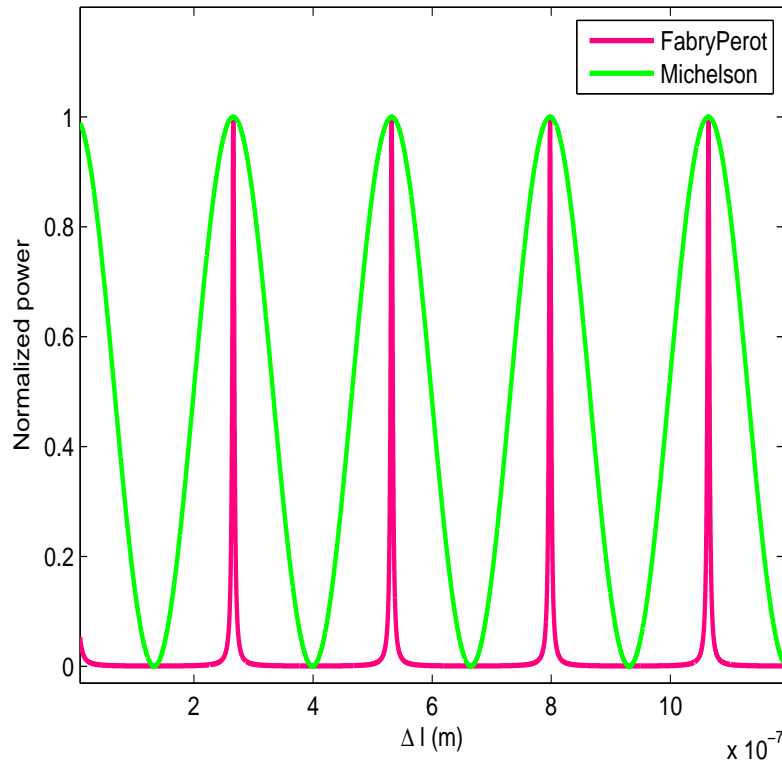


Figure 2.1: Comparison between the transmitted power by the Michelson interferometer and the Fabry Perot interferometer as a function of the variation of the arm length.

The above formulas are well known as *Airy's formulae* and are the basic references for multiple-beam interference.

An important application of two beams interference is the Michelson interferometer, while an application of multiple beam interference is the Fabry Perot resonator. In fig. 2.1 we show a comparison between the transmitted power by the Michelson interferometer and the Fabry Perot interferometer: as we can see the transmission figure of the Fabry Perot shows very narrow peaks in the correspondence of the resonance lengths respect to a sinusoidal variation of the power in the Michelson interferometer: this behaviour affects the sensitivity of these devices in the measurements of relative displacements.

2.1.2 Laser beams: approximate solution for the wave equation

Laser beams are similar in many aspects to plane waves; however their intensity distributions are not uniform but concentrated near the axis of propagation and their fronts are slightly curved [6].

A potential u of the coherent light satisfies the scalar wave equation:

$$\nabla^2 u + k^2 u = 0, \quad (2.14)$$

where $k = \frac{2\pi}{\lambda}$ is the propagation constant in the medium. For light traveling in the z direction we have:

$$u = \Psi(x, y, z) \exp(-ikz), \quad (2.15)$$

where Ψ is a slowly varying complex function which represents the difference between a laser beam and a plane wave, namely: a nonuniform intensity distribution, expansion of the beam with distance of propagation, curvature of the phase front. By inserting (2.15) in (2.14) we obtain:

$$\frac{\partial^2 \Psi}{\partial x^2} + \frac{\partial^2 \Psi}{\partial y^2} - 2ik \frac{\partial \Psi}{\partial z} = 0, \quad (2.16)$$

where it has been assumed that ψ varies so slowly with z that its second derivative $\partial^2 \Psi / \partial z^2$ can be neglected. Explicitly the solution Ψ has the following expression:

$$\Psi = \exp \left\{ -i \left(P + \frac{k}{2q} r^2 \right) \right\}, \quad (2.17)$$

where $r^2 = x^2 + y^2$.

The parameter $P(z)$ represents a *complex* phase shift which is associated with the propagation of the light beam, and $q(z)$ is a *complex* beam parameter which describes the Gaussian variation in beam intensity with the distance r from the optical axis, as well as the curvature of the phase front which is spherical near the axis.

2.1.3 Propagation laws for the fundamental beam

A coherent light beam with a gaussian intensity profile is not the only solution of eq. (2.16), but it is the most important one. This beam is often called the *fundamental mode* as compared to higher order modes which will be discussed later. For convenience we introduce two *real* beam parameters R and w related to the complex parameter q by:

$$\frac{1}{q} = \frac{1}{R} - i \frac{\lambda}{\pi w^2}. \quad (2.18)$$

$R(z)$ represents the radius of curvature of the wavefront that intersects the axis at z , while $w(z)$ is a measure of the decrease of the field amplitude with the distance from the axis. This decrease is gaussian in form and w is the distance at which the amplitude is $1/e$ times that on the axis.

The parameter w is often called the beam radius or spot size. The gaussian beam contracts to a minimum diameter, $2w_0$ at the *beam waist* where the phase front is plane. In this situation the complex beam parameter is purely imaginary:

$$q_0 = i \frac{\pi w_0^2}{\lambda}, \quad (2.19)$$

while at a distance z away from the waist parameter it is:

$$q = q_0 + z = i \frac{\pi w_0^2}{\lambda} + z. \quad (2.20)$$

The propagation laws for $w(z)$ and $R(z)$ are the following:

$$w^2(z) = w_0^2(z) \left[1 + \left(\frac{\lambda z}{\pi w_0^2} \right)^2 \right] \quad (2.21)$$

and

$$R(z) = z \left[1 + \left(\frac{\pi w_0^2}{\lambda z} \right)^2 \right]. \quad (2.22)$$

The beam contour is a hyperbola with asymptotes inclined to the axis at an angle:

$$\theta = \frac{\lambda}{\pi w_0}. \quad (2.23)$$

After some calculations we obtain the final expression for 2.15:

$$u(r, z) = \frac{w_0}{w} \exp \left\{ -i(kz - \Phi) - r^2 \left(\frac{1}{w^2} + \frac{ik}{2R} \right) \right\}, \quad (2.24)$$

where

$$\Phi = \arctan \left(\frac{\lambda z}{\pi w_0^2} \right). \quad (2.25)$$

2.1.4 Higher order modes

In the preceding section we discussed about only one solution of eq. (2.16), but this equation has also other solutions with similar properties to the fundamental beam. These solutions form a complete and orthogonal set of functions and are called the *modes of propagation*. Every arbitrary distribution of monochromatic light can be expanded in terms of these modes.

For a system with a rectangular geometry (x, y, z) eq. (2.16) is satisfied by a solution of the form:

$$\Psi = g \left(\frac{x}{w} \right) \cdot h \left(\frac{y}{w} \right) \cdot \exp \left\{ -i \left(P + \frac{k}{2q} r^2 \right) \right\}, \quad (2.26)$$

with

$$g \cdot h = H_m \left(\sqrt{2} \frac{x}{w} \right) H_n \left(\sqrt{2} \frac{y}{w} \right), \quad (2.27)$$

where H_m and H_n are the Hermite polynomials of order m and n , the transverse mode numbers.

In fig. 2.2, 2.3, 2.4 we show the intensity profile of the fundamental mode and of two higher order modes on a plane which is orthogonal to the propagation direction: as we can see the number of zeros in a mode pattern is equal to the corresponding mode number and the area occupied by the mode increases with the mode number.

The parameter $R(z)$ is the same for all modes, while the phase shift Φ is a function of the mode numbers:

$$\Phi(m, n; z) = (m + n + 1) \arctan(\lambda z / \pi w_0^2). \quad (2.28)$$

This means that the phase velocity increases with increasing mode number.

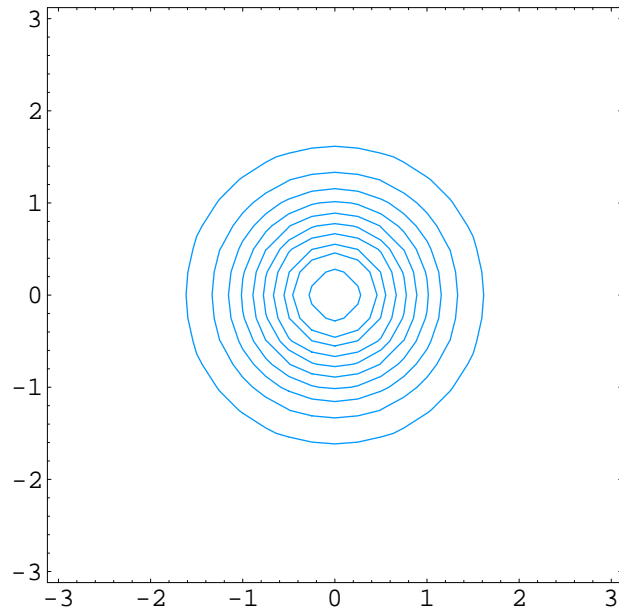


Figure 2.2: Intensity profile of the $TEM_{0,0}$ mode on a plane orthogonal to the propagation direction.

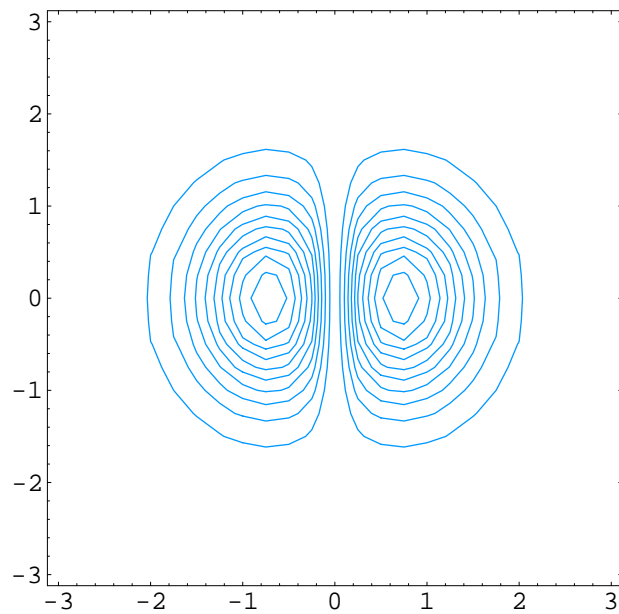


Figure 2.3: Intensity profile of the $TEM_{1,0}$ mode on a plane orthogonal to the propagation direction.

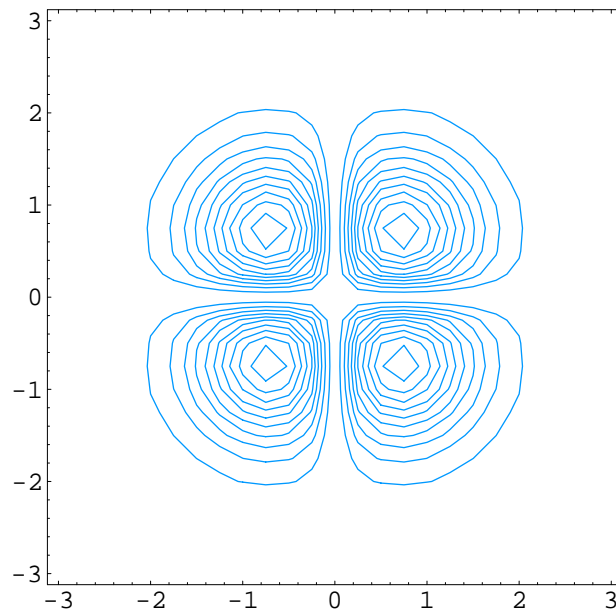


Figure 2.4: Intensity profile of the $TEM_{1,1}$ mode on a plane orthogonal to the propagation direction.

2.1.5 Optical cavities

In the previous sections we have described the phenomenon of interference and the nature of laser beams.

In this section we want to talk about the most important parameters of optical cavities and their common applications in various fields of physics, before than describing in detail the geophysical ones.

A Fabry Perot cavity [7] [8] [9] is composed by two mirrors aligned in such a way that a beam of light is reflected in a closed path, such that after one round trip it interferes perfectly with the incident wave. The light is reflected many times around the cavity: each round trip generates a partial wave, and all these waves interfere.

For the case that $2L$, with L length of the cavity, is an integer multiple of the wavelength of the incident light a strong field will be built up inside the cavity due to constructive interference, the cavity is on resonance.

The transmitted power is very similar to eq.2.13:

$$P_n = \frac{A_n}{1 + \frac{4}{\pi^2} F^2 \sin^2 \frac{\phi_n}{2}}, \quad (2.29)$$

where:

$$F = \frac{\pi \sqrt[4]{R_1 R_2}}{1 - \sqrt{R_1 R_2}} \quad (2.30)$$

is the cavity *finesse*, R_1 and R_2 being the reflectivity of the mirrors, and A_n the power transmitted on the resonance. As we can see the magnitude of the enhancement of the field and the width of the resonance depend on the reflectivities of the mirrors.

As for laser beams even the cavity has its fundamental mode and the higher order modes. The funda-

mental beat frequency, the frequency spacing between successive longitudinal frequencies, is given by the so called *free spectral range*:

$$\nu_0 = \frac{c}{2L} = FSR. \quad (2.31)$$

The transmission figure repeats every FSR: it is equivalent to say that every time the length of the cavity changes of $\lambda/2$ the same transmission figure repeats.

The frequencies of the higher orders resonant modes are:

$$\nu = \nu_0 \left[(q+1) + \frac{1}{\pi}(m+n+1) \arccos \sqrt{\left(1 - \frac{L}{R_1}\right) \left(1 - \frac{L}{R_2}\right)} \right], \quad (2.32)$$

where R_1 and R_2 represent the radius of curvature of the cavity mirrors, m and n are the transverse mode numbers defined in the previous section, while q is the longitudinal mode number, that is the number of nodes of the standing wave pattern.

Moreover the cavity itself produces its own waist in a particular position, according to the geometry of the mirrors and to its length. We mention as an example the main features of the two most used optical systems: a plane concave cavity and a concentric cavity.

The plane concave cavity is made up of a plane and a concave mirror, with radius of curvature R_c , put at the distance L . The cavity waist is situated on the plane mirror and the square of its radius w_0 is given by:

$$w_0^2 = \frac{\lambda}{\pi} \sqrt{L(R_c - L)}. \quad (2.33)$$

The concentric cavity is made up of two mirrors with equal radius of curvature R_c , put at the distance L . In this case the cavity waist is situated at the center of the cavity and the square of its radius w_0 is given by:

$$w_0^2 = \frac{\lambda}{2\pi} \sqrt{L(2R_c - L)}. \quad (2.34)$$

An important problem encountered when using a cavity is the matching of the mode of the laser beam with the mode of the optical structure we inject it into: this is usually accomplished with one or more thin lenses, as we will describe in the following chapter.

Another important feature of cavities is their stability: cavities are stable when light rays that bounce back and forth between the mirrors experience a periodic focusing action, that is to say when mirror apertures are large compared to the spot size of the beams. For a generic cavity, whose mirrors' radius of curvature are R_{c1} and R_{c2} , the condition of stability is written:

$$0 < \left(1 - \frac{R_{c1}}{L}\right) \left(1 - \frac{R_{c2}}{L}\right) < 1. \quad (2.35)$$

Cavities are used for various purposes: the laser itself is a cavity with an active medium inside to provide the gain, a cavity can be used as a very stable reference for the frequency of the light, a cavity can be used as a filter for the geometrical fluctuations of laser beams, or to study the fine structure of spectral lines.

2.2 Optical interferometers as seismic sensors

In this section we will tell a bit of history on some interesting applications for Michelson, first, and then for Fabry Perot interferometers in seismic noise measurements.

- One of the first proposals about the use of a Michelson interferometer as a strainmeter took place in California [10] [11]. The authors, Berger and Lovberg, installed a 800-meter laser strainmeter above the surface of the ground.

The light source for the interferometer was a single frequency, unimode, He-Ne laser: the exact output frequency could be tuned by applying a voltage to a piezo-electric translator on which one of the cavity mirrors was mounted.

The laser source, the beam splitter, and a reflector were put on one pier, and the remote reflector on another. These piers were 3-meter-long columns of black granite with a cross section of approximately 1 meter and cemented into holes drilled in the rock along the lower 1 meter. The optical path between the ends was provided by an evacuated stainless steel tube.

The interferometer was used as an optical comparator, measuring changes in the length with reference to some integral multiple of the optical wavelength standard. The reference element was a passive Fabry-Perot optical resonator with a finesse of over 100.

This Michelson strainmeter had a strain least count of 10^{-10} , required no calibration, and had a flat and linear response from zero to 1 MHz. The linearity and large dynamic range offered unprecedented versatility in the recording of seismic strains associated with earthquakes and nuclear blasts and provided a mean of making crustal strain measurements and mapping the strain field distributions.

- A similar use of a Michelson strainmeter took place in England in 1974 by Goult et al. [12] [13] [14]. They installed the interferometer in a disused railway tunnel at Queensbury.

The optical components of the interferometer were a semireflecting mirror and two corner cube reflectors, all in vacuum to avoid contamination; one corner cube was rigidly connected to the beam splitter by a low expansion Invar mount to provide a reference arm: the interferometer arms were 54 m. long.

The laser illuminating the interferometer was a slave laser: one laser mirror was mounted on a piezo-electric cylinder so that the laser cavity length could be altered by the application of a voltage on it. This length and, as a consequence, the laser frequency, were dynamically adjusted in order to keep the fringe constant at the output of the interferometer.

A second laser stabilized by saturated absorption in iodine vapour and characterized by an extremely good frequency stability over very long periods was used as a reference for the slave laser.

The strain in the interferometer was finally obtained with very high resolution and linearity by means of the beat frequency technique, that is the measure of the frequency difference between the slave laser and the stabilized laser described in this paper with great detail.

By using this kind of interferometer the authors recorded twelve weeks of tidal datas and several small earthquakes: moreover they found in this device excellent instrumental characteristics for monitoring secular strain and for studying the free oscillations of the earth.

- After some years in 1993 Aleshin et al. described the performances of various laser strainmeters installed in geophysical test tunnels during the period 1981-1990 [15] [16] . These instruments had similar designs and measurements methods: the operation principle was based on the registration of small relative displacements between two optical elements of the interferometer attached at opposite ends of the area being studied; the optical arrangement was based on a non-equal-arm Michelson interferometer with arm lengths from 10 to 20 m.

The strainmeters consisted of three optical units (frequency stabilized laser unit, interferometer unit, reflector unit) and a control unit to keep the working point constant.

The authors listed the various operating strainmeters and the respective performance. The best representative observation series was collected in 1981-85 using a 16 m laser strainmeter at Protvino: this instrument recorded pulsations of the two main diurnal tidal waves.

Subsequent strainmeters installations in 1986-90 were made for studies of high frequency seismic and acoustic processes in the crust for both natural and other anthropogenic components. Another objective was to study the application conditions of these instruments for calibration of various types of seismic monitoring devices.

A laser strainmeter installed in the coastal zone at 50-70 m from the shoreline at the depth of 3 m was used to study deformation processes in a transient sealand region.

Other two strainmeters had interesting applications: the first one, with measurement arms of 7 m, was installed at the seismic station of the Institute of Earth Physics at Borovoye (North Kazakhstan) at a depth of ≈ 16 m. The second one, with measurement arms of 12 m, was installed in the Lomonosov underground laboratory of the Institute of Metrology at a depth of ≈ 45 m. These strainmeters were used to monitor seismic signals in the range 0.1-100 Hz.

At the end the authors emphasized the possibility of obtaining accured measurement of tidal deformations and to isolate the intrinsic oscillation of the earth by the use of this kind of laser strainmeters placed deep under ground.

- In 1993 Tsubono et al. [17] developed a wideband (dc to 2 kHz) and highly sensitive seismometer which could detect the horizontal component of the acceleration of the ground using a Michelson laser interferometer. One of the mirrors of the interferometer was put on the ground while the other mirror was suspended on a simple pendulum mass, in order to act as a free mass in the frequency range after the natural resonance of the pendular suspension.

Assuming that the fixed mirror moved together with the ground they detected the relative displacement between the ground and the pendulum mass from the fringe signal of the interferometer. This signal was fed-back to the suspension in order to keep the interference on: the feedback force was proportional to the horizontal component of the acceleration.

This interferometer had portable size (27cm×24cm×15cm) and the main factors limiting its sensitivity were the shot noise, intensity and frequency noise of the laser, and the thermal fluctuations of air.

With this kind of interferometer the authors measured seismic noise level at two sites: at the standard gravity room of the university of Tokio and at the Kamioka mine.

The results showed a sensitive measure of seismic vibration at the sites: the minimum measurable displacement was $3 \times 10^{-11} \text{m}/\sqrt{\text{Hz}}$ at 1 Hz and $2 \times 10^{-15} \text{m}/\sqrt{\text{Hz}}$ above 2 kHz.

- In 1997 Crescentini et al. re-proposed and described the use of a Michelson interferometer as a strainmeter [18] [19].

They installed a geophysical interferometer beside the Gran Sasso Tunnel (10.4 km long), in the vicinity of an underground laboratory of INFN, taking advantage of the galleries that surrounded the main halls of the lab, where an important fault was situated: this fault was expected to have some modest level of activity. The galleries were extended to constitute a triangle located at 1100 m under the free surface.

The interferometer was planned to measure relative displacements of three 1m^3 blocks, each sitting on a 8m^3 underground cubic platform, by the analysis of the transmitted intensity; a vacuum system enclosed the all device.

The authors recorded signals during the transit of a surface wave and also analyzed a 70 day-long stretch of typical data in order to obtain the noise level of the interferometer: the instrument showed a good dynamical range and the lack of hysteresis.

- Fabry Perot interferometer has already been used as a strainmeter, too [20] [21] .

In 1972 Levin and Hall designed with accuracy a 30 meter Fabry Perot interferometer in order to obtain a long term measurement of the earth tides and also a measurement of the power spectrum of the earth's vibrations.

This interferometer was located into a dismissed gold mine: the mirrors and the optical path were enclosed in a vacuum tight tube at a pressure around 10 mtorr. The small changes in the length of the cavity were monitored through the transmission figure of the interferometer. The authors used two lasers and the beat frequency technique, repropoed 2 years after by Gouly et al.: the first laser was an helium-neon laser with adjustable length and frequency in order to keep interference on following the strain in the cavity; the second laser was a very stable reference through molecular absorption frequency in methane.

In their paper Levin and Hall showed the various features of this long-path device and the advantages over the conventional mechanical instruments: excellent sensitivity, wide bandwidth and essentially no drift.

By using this instrument, the authors were able to monitor the earth tides for 42 days, with a noise power of about $5 \times 10^{-21}(\Delta L/L)^2/\text{Hz}$, about a factor 10 lower than the noise power found for Benioff type strainmeters.

- Another interesting application of a Fabry Perot interferometer was the speed-meter one.

In 2003 Angela Di Virgilio et al. [22] proposed and analyzed the use of a suspended cavity as speed-meter. The authors found a method to evaluate the relative speed and position of the LFF cavity mirrors from the transmitted power only, obtaining a displacement spectral density of the order of $3 \times 10^{-10}\text{m}/\text{Hz}^{-1/2}$ at 10 Hz.

- In 2006 Ricciardi et al. [23] studied in detail the optical response of a suspended and misaligned Fabry Perot cavity. They presented a five degree of freedom dynamical model of the fluctuations of the longitudinal and transverse mirror coordinates. This model has been used to design a cavity with a suspended mirror, the seismometer developed in this work.

2.3 The Fabry Perot interferometer as a speed-meter

An interesting application of a Fabry Perot interferometer is the speed-meter one [22]. In this section we will describe a method to evaluate the relative speed of the two mirrors of a Fabry Perot interferometer from the transmitted signal.

The application of this method requires a very stable transmission power: the cavity has to be isolated from the external environmental noises, suspending it to a multipendular chain and putting it under vacuum.

We know from the previous section that in accordance with the motion of the two mirrors of an optical cavity a pattern of several spatial modes TEM_{lm} are transmitted. Let us call for simplicity mode n any TEM_{lm} having the same $l+m=n$. For each mode n the power transmitted by cavity depends on the phase detuning ϕ_n between the light and cavity length.

We know that the transmitted power P_n is described by the well known Airy function:

$$P_n = \frac{A_n}{1 + \frac{4}{\pi^2} F^2 \sin^2 \frac{\phi_n}{2}}. \quad (2.36)$$

Imposing the transmitted power to be below 10% of the maximum for $\phi_n = 0.25$ rad (the sine function can be approximated with 1% error for arguments below 0.25 rad), the above formula can be simplified as follows (for $F > 40$):

$$P_n = \frac{A_n}{1 + F^2 \frac{\phi_n^2}{\pi^2}}. \quad (2.37)$$

The absolute value of the detuning ϕ_n can be directly extracted from P_n ; while ϕ_n derivative $\frac{d\phi}{dt} = \frac{4\pi v}{\lambda}$ is proportional to v , the relative speed of the mirrors. We also know that the transmitted pattern repeats every free spectral range FSR , i.e., every $\phi = \phi_n + 2m\pi$, (m integer).

Let us see now how absolute value of the relative speed of the two mirrors can be reconstructed. The time derivative of the Airy function is:

$$\frac{dP}{dt} = \frac{dP}{d\phi} \frac{d\phi}{dt} = \frac{dP}{d\phi} \left(\frac{2\pi}{\lambda} v \right), \quad (2.38)$$

neglecting light amplitude, frequency fluctuations and time dependent misalignments. The maximum and minimum of this first derivative with respect to ϕ , respectively MAX and MIN , occur at $\phi = \frac{\pi^2}{\sqrt{3}F}$. In the case of constant speed the amplitude of the time derivative is:

$$MAX = \frac{A_n 3\sqrt{3}F}{8\pi} \frac{2\pi}{\lambda} v. \quad (2.39)$$

Thus the measurement of the amplitudes MAX and MIN yields an immediate evaluation of the absolute value of the speed v .

This method applies also in the case of non-constant speed of the mirrors. In order to show the effect of a variable speed let us consider the case of a constant phase acceleration α :

$$\phi_n = \phi_0 + v_0 t + \alpha t^2 / 2, \quad (2.40)$$

where t is the time. Since ϕ_n is the detuning with respect to the resonance, we set $\phi_0 = 0$ for $t = 0$ and v_0 at $t = 0$. The phase ϕ_n can be more conveniently expressed using only one parameter α :

$$\phi_n = \alpha t'^2 + t', \quad (2.41)$$

the speed v and t being:

$$v = (2\alpha t' + 1) \frac{v_0 \lambda}{2\pi}, \quad t' = t v_0, \quad (2.42)$$

In their paper Angela Di Virgilio et al. show that for $\alpha < 1000$ the error between the expected speed and the theoretical one is below 5%.

The sign of the velocity can be determined by the mode sequence, since the position of each mode is fixed inside each FSR .

2.4 Fabry Perot seismic interferometers

In this section we will introduce a simple model for the use of a Fabry Perot interferometer in seismic noise measurements and derive the transfer function of this device.

As mentioned in the above section the transmitted intensity by the interferometer is linked to the phase shift Φ between the laser light and the length of the cavity:

$$\Phi(t) = \frac{4\pi n}{\lambda} \Delta L(t). \quad (2.43)$$

We assume that the position of the input cavity mirror is centered around zero, while the position of the output mirror is centered around L_c . Let $n_i(t)$ and $n_o(t)$ be the noise sources on the input and output mirror, respectively.

Let us suppose that a seismic wave $s(t)$ with velocity v_s , whose wave propagation vector k lies at an angle α with the optical axis, arrives on the input mirror of the interferometer at the time $t = 0$. After a time t_p for the propagation inside the cavity, the seismic wave will arrive at the output mirror attenuated by a factor a_s ($0 < a_s < 1$). The expression for t_p is:

$$t_p = \frac{L_c + n_o(t) - n_i(t)}{v_s} \cos \alpha^{(F/\pi)}, \quad (2.44)$$

where the factor (F/π) takes into account the cavity *finesse*, to obtain the real optical path inside the Fabry Perot. In this configuration the phase shift in eq. (2.43) becomes:

$$\Phi = \frac{4\pi n}{\lambda} \left\{ L_c + n_o(t) - n_i(t) + [s(t) - a_s s(t - t_p)] \cos \alpha^{(F/\pi)} \right\}. \quad (2.45)$$

Let now $\Delta L(t) = L_c(t) + n_o(t) - n_i(t)$ be the length change in absence of seismic signal. The relationship in the Laplace domain between the seismic signal $s(t)$ and the phase Φ is:

$$\Phi(s) = \frac{4\pi n}{\lambda} \left[\Delta L(s) + S(s)(1 - a_s e^{-t_p s}) \cos \alpha^{(F/\pi)} \right]. \quad (2.46)$$

The transfer function of the system that links the input seismic signal $S(s)$ with the output Fabry Perot phase $\Phi(s)$ can be written as:

$$H(s) = \frac{\Phi(s)}{S(s)} = \frac{4\pi n}{\lambda} (1 - a_s e^{-t_p s}) \cos \alpha^{(F/\pi)}. \quad (2.47)$$

In the limit of short cavity length respect to the seismic wave wavelength we can expand $e^{-t_p s}$ in eq. (2.47) in Taylor series, obtaining:

$$\begin{aligned} H(s) &= \frac{4\pi n}{\lambda} \cos \alpha^{(F/\pi)} \left[1 - a_s \sum_{k=0}^{\infty} \frac{s^k}{k!} \frac{d^k e^{-t_p s}}{ds^k} \Big|_{t_p=0} \right] \\ &= \frac{4\pi n}{\lambda} \cos \alpha^{(F/\pi)} \left[(1 - a_s) + a_s \sum_{k=1}^{\infty} \frac{s^k}{k!} \frac{d^k e^{-t_p s}}{ds^k} \Big|_{t_p=0} \right]. \end{aligned} \quad (2.48)$$

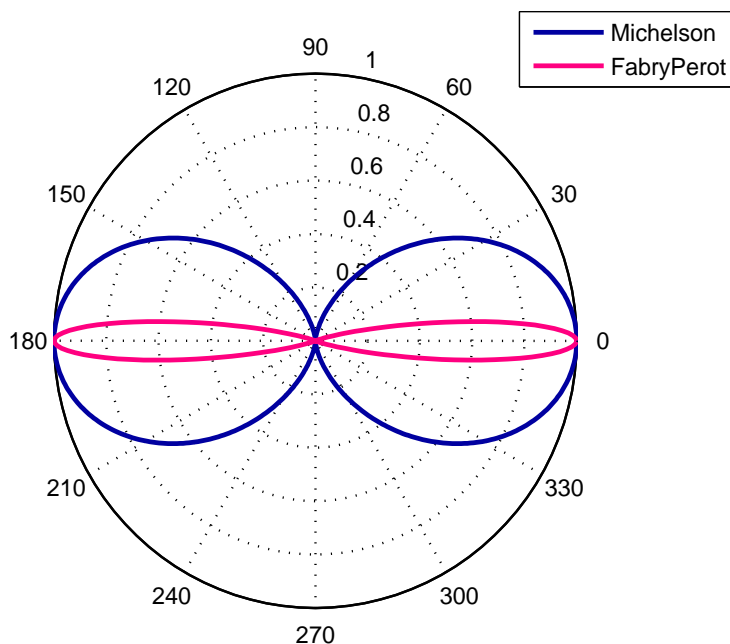


Figure 2.5: Sensitivity diagram for the Michelson and Fabry Perot interferometers.

Since we are considering an interferometer with short arms, we can retain only the term for $k = 1$ of Taylor series and approximate the attenuation factor $a_s = 1$; eq. (2.46) becomes:

$$\Phi(s) = \frac{4\pi n}{\lambda} \cos \alpha \left(\frac{F}{\pi}\right) t_p s S(s). \quad (2.49)$$

Using the explicit expression for t_p in eq. (2.44) we finally obtain for the transfer function:

$$H(j\omega) = \frac{4\pi n}{\lambda v_s} j \omega \cos \alpha^{(2F/\pi)}. \quad (2.50)$$

Fig. 2.5 shows the comparison between the normalized sensitivity diagrams of the Fabry Perot and the Michelson interferometer. Both diagrams show the maximum sensitivity for the angles of incidence $\alpha = 0$ and $\alpha = \pi$, but the Fabry Perot response is much more sensitive to the signal direction than the Michelson one.

Chapter 3

Reading and actuation systems for suspended mass control

In the previous chapter we described several applications of interferometers in the field of geophysics. This thesis work aims to describe the performances of a Fabry Perot interferometer with a suspended mass as a very sensitive device in seismic noise measurements.

In order to keep interference on between the Fabry Perot mirrors we need to fine control their longitudinal position and orientation. For this purpose in this chapter we will concentrate on the problem of mirror position control.

We will first describe the optical levers used to read the position of the mirrors and then we will describe the actuation systems. In particular we will point out the limitations of the most currently used system of actuation (coil-magnet) and introduce an alternative system based on the electrostatic actuation.

We will develop in detail the theoretical model for the electrostatic actuation, refine this model and compare the new theoretical data with the experimental ones.

Our results show that there is a concrete possibility of replacing the magnetic actuation system with the electrostatic one in situations where some force of the order from μN to mN is needed.

3.1 Optical reading system for suspended mass

The output mirror of the Fabry Perot interferometer is suspended to a double pendulum suspension, in order to isolate it from the motion of the ground in the band of frequencies after the mechanical resonances of the pendulum.

In order to obtain a sensitive error signal about the position of the suspended mass on the various degree of freedom we use an optical lever reading system (fig: 3.1).

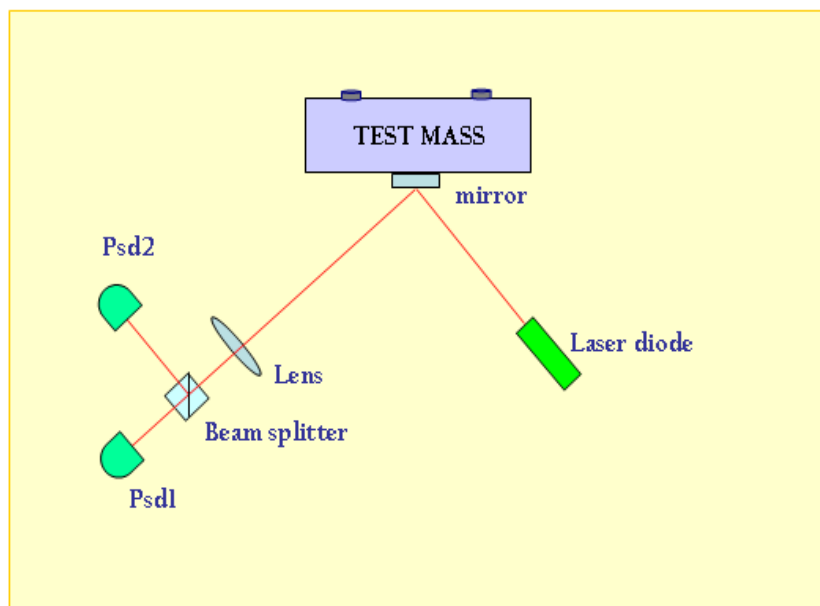


Figure 3.1: A schematic view of the reading system used to decouple the rotational motions of the mirror from the longitudinal ones.

The working principle of an optical lever is the following: an auxiliary laser diode at the wavelength of 670 nm impinges on the centre of a mirror put on the suspended mass and the reflected beam is detected by a position sensing photodiode (PSD), whose signal contains informations about the displacements of the mass.

The photodiode has a spectral response in the wavelength range from $\approx 200nm$ to $\approx 1200nm$. The sensing surface of the PSD contains four electrodes from whose signals we can obtain the coordinates (x, y) of the illuminated point, as follows:

$$x = \frac{x_2 + x_3 - x_1 - x_4}{x_1 + x_2 + x_3 + x_4}, \quad (3.1)$$

$$y = \frac{x_1 + x_2 - x_3 - x_4}{x_1 + x_2 + x_3 + x_4}. \quad (3.2)$$

Moreover, in order to decouple the translational motions from the longitudinal ones, a lens with focal length f and a beam splitter are added in the path between the mass and the photodiode. In this way the beam reflected from the mass is splitted in two beams detected by two photodiodes Psd1 and Psd2. The lens is put at a distance a from the mass we want to control. The distance $d1 = f$ from Psd1 and the distance $d2 = -af/(f - a)$ from Psd2 are chosen to read only the rotational motions or the translational motions, respectively.

The sensitivity of the PSD from precedent studies is affected only by ADC noise and is:

$$\Delta y = \Delta x = \sqrt{\left[\frac{1}{4V_0}\right]^2 \left(\sum_i \Delta V_i\right)^2} \cdot \frac{L}{2} = 1.2 \cdot 10^{-8} \frac{m}{\sqrt{Hz}}, \quad (3.3)$$

where L represents the active width of the photodiode, ΔV_i the variations in the tensions of the four electrodes of the Psd and $V_0 = 5V$ represents the half of the ADC dynamics.

3.2 Coil-magnet system of actuation: description and limitations

The most used system of actuation for suspended mass control is the coil-magnet one (3.2).

The working principle of this system is the following: four permanent magnets are attached to the back of the mirror whose position we want to control; four coils where current flows are put in the correspondence of the magnets. Through the application of the magnetic field created by the coils we can control the mirror position on the various degrees of freedom.

This system of actuation presents two negative aspects:

- Alteration of the Q factor of the mirrors
- Difficulty in the fine control of the position due to the Barkhausen noise in the magnets

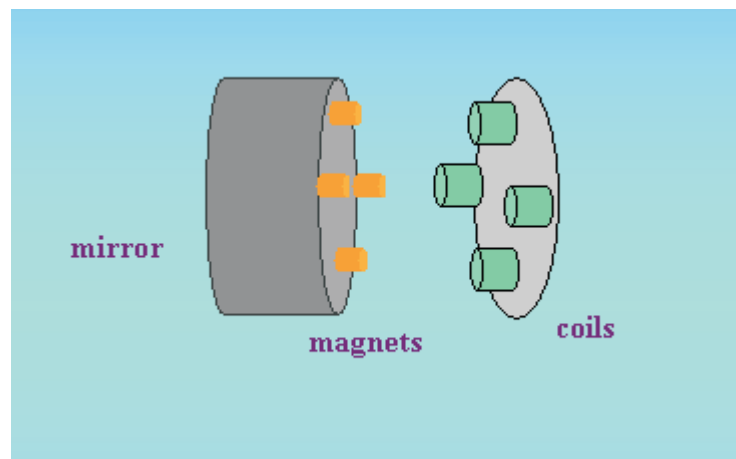


Figure 3.2: A schematic view of the coil-magnet system of actuation.

The first aspect is linked to the attachment of permanent magnets on the back of the mirrors. The magnets alter the symmetry of the mechanical configuration of the mirror and its resonance frequency: the mechanical factor of quality Q of this oscillator is degraded. As a consequence we have an increase of thermal noise which can limit the performance of the suspension system.

The second aspect is linked to the Barkhausen effect: it consists of a series of sudden changes in the size and orientation of ferromagnetic domains that occurs during the process of magnetization or demagnetization. This effect shows the direct evidence that the magnetization of a ferromagnetic substance by an increasing magnetic field takes place in discontinuous steps, rather than continuously. Fig. 3.3 shows a typical magnetization curve with B , the flux density, appearing to be a continuous function of the magnetic field H : but, if we examine the figure more closely, we find that the $B - H$ curve consists of small, discontinuous changes of B as H varies. These changes are the results of the Barkhausen effect, which has been studied in detail for various materials [24], and may cause a sort of noise in the force applied to the magnets limiting the precision in the fine control of the mirrors [25] [26].

At last the coil-magnet system is sensitive to environmental electromagnetic noises.

3.3 Current model for electrostatic actuators

In the previous section we talked about the coil-magnet system of actuation and its limitations.

An alternative to this system is the electrostatic one, already used for the suspended test mass control in some current experiments [27] [28] [29]. This system does not imply the degradation of the Q factor of the mirrors and is not subjected to Barkhausen noise at all: the use of an electrostatic actuator just needs a dielectric mounting for the mirror.

In this section we will describe the model used to obtain the force exerted by this device as a function of

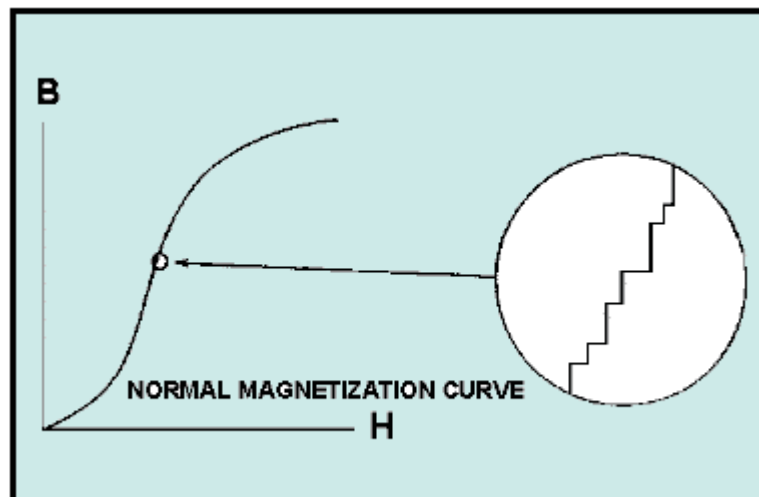


Figure 3.3: Magnetization curve: in the zoom we can note the sudden changes in the size and orientation of ferromagnetic domains.

the distance from the mirror.

3.3.1 Periodic sequence of strips at alternate potentials

An electrostatic actuator is composed by a periodic sequence of plane electrodes at alternate potentials lying on a dielectric substrate [30]. We schematize the electrostatic actuator as an array of plane electrodes (fig. 3.4) whose most important geometrical parameters are:

- width of the strips a
- length of the strips L
- semiperiod of the potential b
- gap between the strips $b - a$
- number of electrodes N

The mirror is schematized as a dielectric of constant permittivity ϵ_m and the actuator substrate as a dielectric of constant permittivity ϵ_{sub} , the system being uniform along the y direction, as the potential is independent of this coordinate (fig. 3.5).

Hence, if we want to obtain the force exerted by this device we have to solve a $2D$ electrostatic problem to find the potential $V(\omega)$, then calculate the capacity of the entire system in the presence of the various dielectrics and at the end calculate the force.

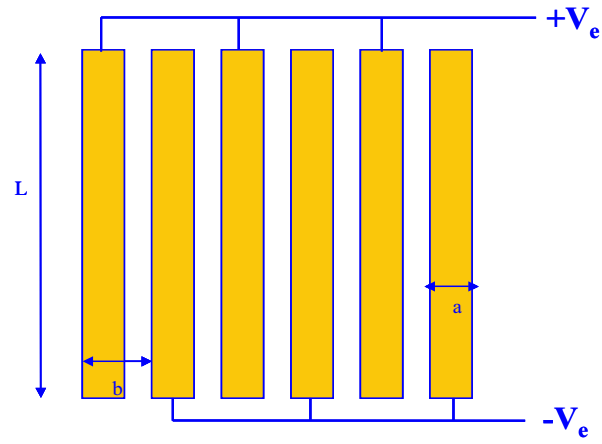


Figure 3.4: A schematic view of the electrostatic actuator: we note the various strips and the geometrical parameters a , b , L .

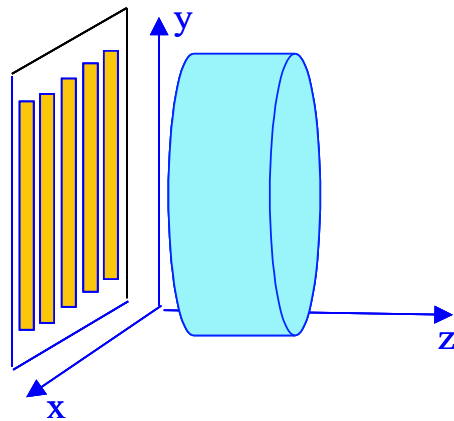


Figure 3.5: Electrostatic actuator placed in the correspondence of the mirror to be controlled.

Let us first consider the integral of our electrostatic problem $V(\omega)$, which is the real or imaginary part of an analytic function of the complex variable $\omega = (x - \zeta) + i(z - \xi)$. $V(\omega)$, as the actuator structure is periodic along the direction x , is a periodic function of period $2b$:

$$V(\omega + nb) = (-1)^n V(\omega). \quad (3.4)$$

We will approach the problem by relying on the integral relation between the charge distribution on each electrode and their respective potential V_e . Indicating by $\rho(x)$ the surface charge density on a reference electrode at potential V_e and extending from $x = -a/2$ to $x = a/2$ the potential on the plane $z = d/2$ can be expressed as:

$$V(d/2, x) = \int_{-a/2}^{a/2} \rho(\zeta) G(x - \zeta) d\zeta, \quad (3.5)$$

where $G(x - \zeta)$ is the potential on the electrode plane relative to the point x , created by a periodic array of linear charge distributions:

$$\tilde{\rho}(\zeta) = \delta(\zeta) - \delta(\zeta + b) - \delta(\zeta - b) + \delta(\zeta + 2b) + \delta(\zeta - 2b) - \delta(\zeta + 3b) - \delta(\zeta - 3b) \cdots \quad (3.6)$$

placed in front of the dielectric at a distance $d/2$.

In particular the kernel G is a periodic function of x :

$$G(x + nb) = (-1)^n G(x). \quad (3.7)$$

In view of the symmetry of the electrode array, $\rho(\zeta) = \rho(-\zeta)$ eq. (3.5) simplifies as:

$$V(d/2, x) = \frac{1}{2\pi\epsilon_0} \int_{-a/2}^{a/2} \rho(\zeta) M(x, \zeta) d\zeta, \quad (3.8)$$

where $M(x, \zeta) = 2\pi\epsilon_0[G(x - \zeta) + G(x + \zeta)]$. The capacity C , related to a couple of consecutive electrodes at potentials $+V_e$ and $-V_e$ respectively:

$$C = \frac{L}{V_e} \int_0^{a/2} \rho(\zeta) d\zeta, \quad (3.9)$$

with L length of the single strip.

The total capacity of the array is $C_T = N/2 \cdot C$, N being the number of electrodes. The force on the mirror can be expressed by:

$$F = \frac{1}{2} \left| \frac{dC_T}{dz} \right| (2V_e)^2. \quad (3.10)$$

The first step is to find the expression for the kernel G in eq. (3.5) in the free space and successively in the presence of the various dielectrics. This procedure is made up of three steps:

- calculus of the expression for G_{fs} related to an array of electrodes in the free space
- calculus of the expression for G_{sub} related to an array lying on a dielectric substrate of finite thickness

h

- modification of G_{sub} in G_{m} by applying the method of the image charges to take into account the presence of the dielectric mirror

All the above points have been revisited and refined in the present work (see Appendix A).

3.4 New theoretical simulations and experimental results

Once we have refined the model for the electrostatic actuator, we made several simulations of the capacity as a function of the various geometrical parameters in order to optimize the actuator design.

This section contains all these simulations and the experimental results obtained by the use of this new actuation system: the most important results are the locking of a Michelson interferometer with both suspended arms and the first control of a double pendulum suspension driving the actuator in alternate current.

3.4.1 Optimization of the algorithm to calculate the capacitance

In appendix A we have introduced a matrix formalism for the capacity of the array of electrodes and as a consequence for the force. This formalism is based on the discretization of the integration period $[0, \pi/2]$.

To this end we have made simulations of the capacity in the free space as a function of N in order to optimize the value of this parameter.

As we can see from fig. 3.6 there is no appreciable change in the value of the capacity starting from $N = 600$: for this reason we fixed $N = 600$ for next simulations.

3.4.2 Optimization of the actuator design

In order to optimize the actuator design we have made two different kinds of simulations:

- Simulations of the capacity versus the dielectric substrate thickness h
- Simulations of the capacity versus the ratio amplitude-gap a/b of a couple of electrodes

The first simulations (fig. 3.7) show that there is no appreciable change in the capacity for thickness $h > 1.7\text{mm}$. This is due to the fact that the field lines do not penetrate the dielectric over this value of the thickness. The second simulations (fig. 3.8) show that a reasonable range for the ratio a/b is $[0.7, 0.9]$. Hence we have fixed the value of h at 1.7mm and the value of the ratio a/b at 0.8 for our next simulations and for the design of the actuator.

In table 3.1 we find all the geometrical parameters fixed for our actuator.

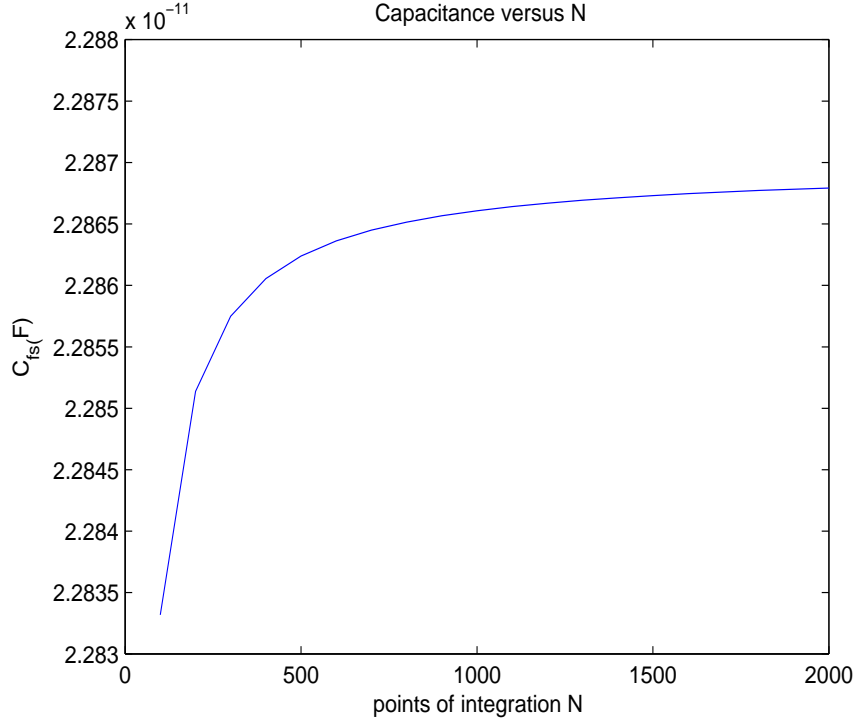


Figure 3.6: Simulation of the capacity versus the number of integration points N .

Strip width a	$3.2 \cdot 10^{-3} m$
Strip length L	$8 \cdot 10^{-2} m$
Strip gap $b - a$	$0.8 \cdot 10^{-3} m$
Substrate thickness h	$1.7 \cdot 10^{-3} m$
Number of electrodes N	20

Table 3.1: Geometrical parameters for the simulated electrostatic actuator

3.4.3 Refined theoretical model

Once we have fixed the best geometrical parameters for the design of the electrostatic actuator, we refined the theoretical model including a bigger number of images in the expression for the kernel G_m in the presence of the mirror in eq. (A.18). The expression used until now for G_m was:

$$G_m(\hat{\omega}) \approx (1 - \gamma_s)G_{fs}(\hat{\omega}) - \gamma_m G_{fs}(\hat{\omega} - i\hat{d}) + \gamma_m \gamma_s G_{fs}(\hat{\omega} + i\hat{d}). \quad (3.11)$$

We have made simulations of the capacity adding in eq. (3.11) terms as:

$$\gamma_s^{(2n-1)} \gamma_s' \gamma_s'' G_{fs}(\hat{\omega} + 2in\hat{h}), \quad n = 1, 2, 3, \quad (3.12)$$

including the various images of the dielectric substrate.

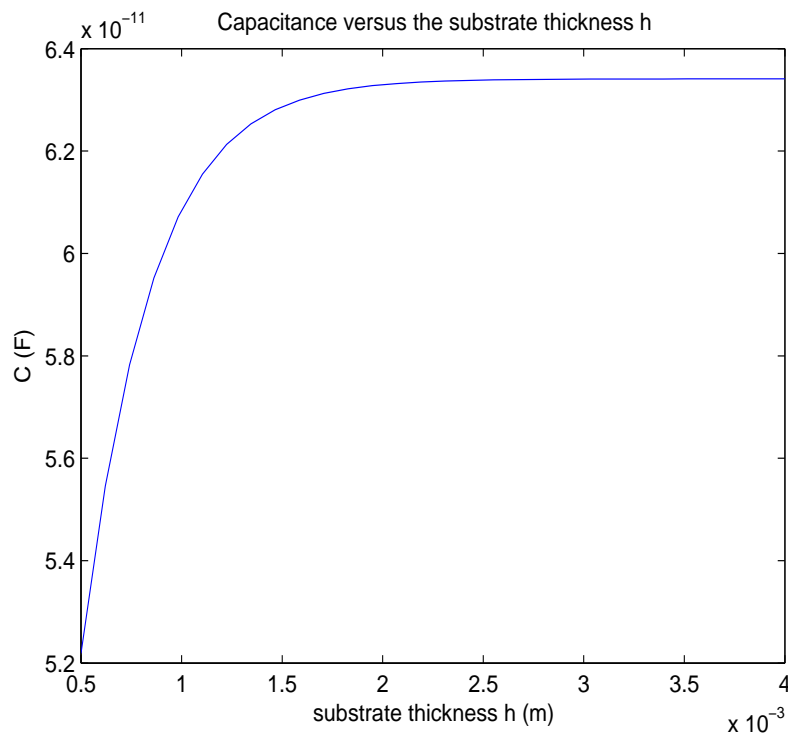


Figure 3.7: Simulation of the capacity versus the substrate thickness h .

In fig. 3.9 we can see four different simulations for the capacity of an actuator with the same geometrical parameters, but including different number of images.

Fig. 3.10 shows a zoom of the above simulation: as we can see the process seems to converge after the use of three images, our choice for the last simulations.

From fig. 3.11 we can make the same considerations in the simulation of the force.

3.4.4 Simulations of the force

This subsection contains various simulations of the force exerted by an actuator as a function of the distance from the mirror in correspondence of various potentials V_e . As we can see from fig. 3.12 by the use of $V_e = 1kV$, positioning the actuator at a distance from the mirror in the range of $2 - 5mm$ we can obtain forces of the order of tens of mN .

3.5 Experimental set up, measures and results

First experimental tests

We analyze now our first tests for the electrostatic actuator on a double pendulum suspension. The position of the upper stage of the suspension, which is suspended baricentrically, is controlled with a coil-magnet

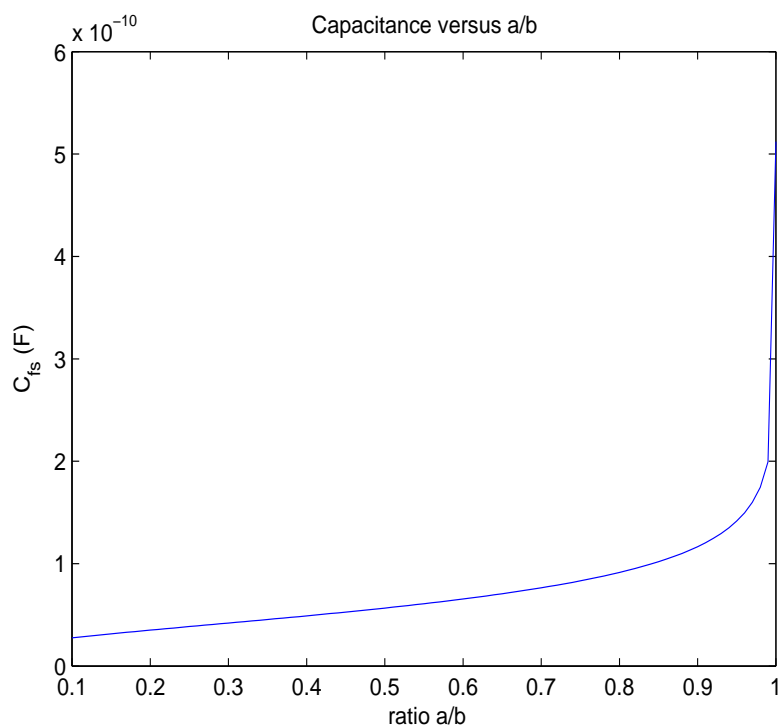


Figure 3.8: Simulation of the capacity versus the ratio a/b .

system, while the second stage, suspended through the use of four wires, is controlled with an electrostatic actuator (fig. 3.13). To this end the aluminum support mass for the mirror has been replaced with a plexiglass one. A scheme of the actuator is shown in fig. 3.14.

The parameters of the single strips of this new actuator are shown in table 3.2, the alimentation is fixed at 1500 V and the force on the mirror has been measured as a function of the distance from the actuator.

The comparison between the simulated force and the experimental one is shown in fig. 3.15.

Strip width a	$4 \cdot 10^{-3}m$
Strip length L	$4 \cdot 10^{-2}m$
Strip gap $b - a$	$1 \cdot 10^{-3}m$
Substrate thickness h	$1.7 \cdot 10^{-3}m$
Number of electrodes N	8

Table 3.2: Geometrical parameters for the newly designed electrostatic actuator.

Michelson interferometer locking

This subsection describes the first important result obtained with the use of the electrostatic actuation: the locking of a Michelson interferometer with both suspended arms (fig. 3.16). The first arm optics (beam

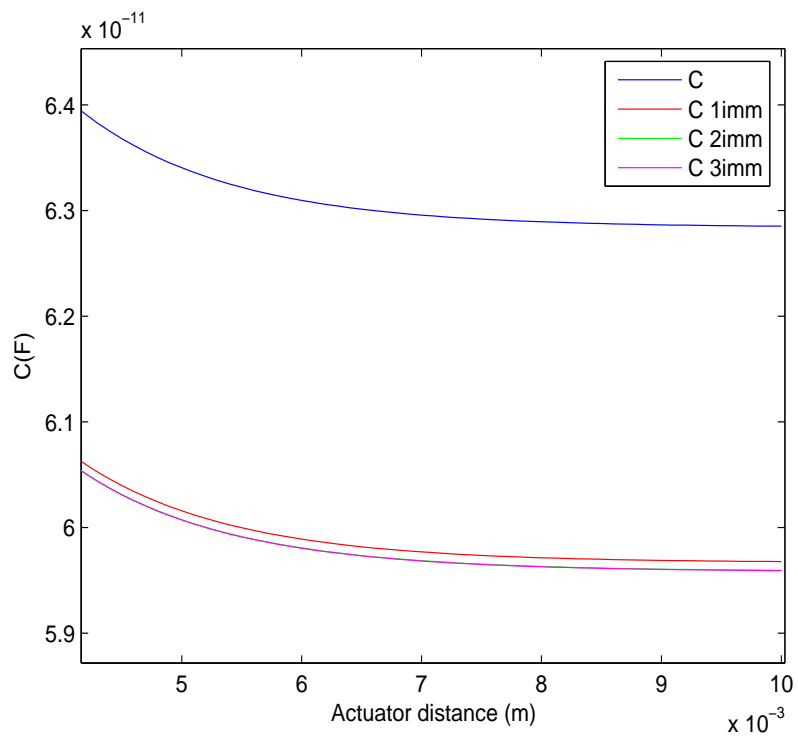


Figure 3.9: Simulations of the capacity in the correspondence of different numbers of images.

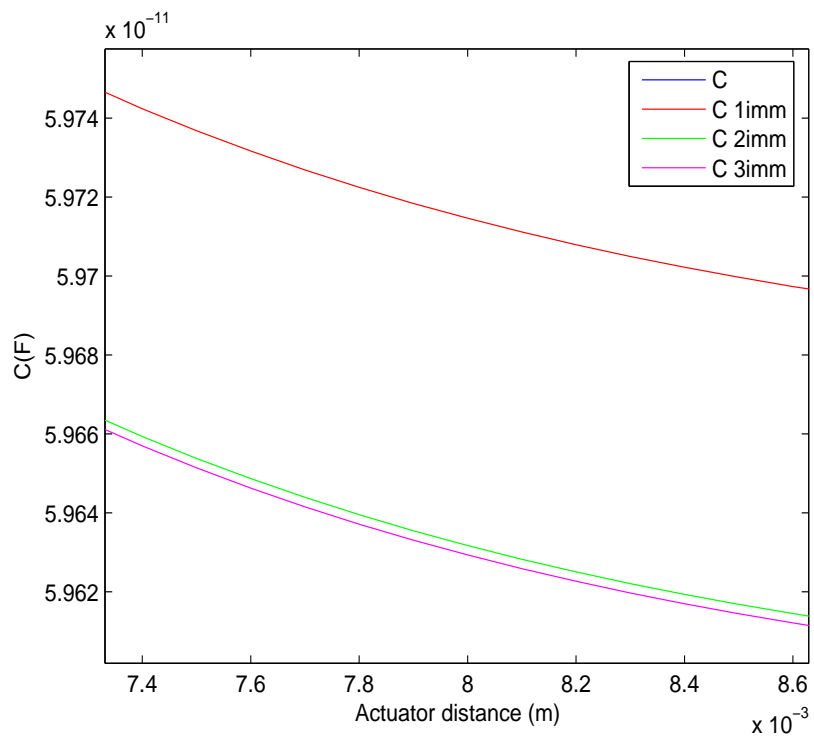


Figure 3.10: A zoom of the above graphics.

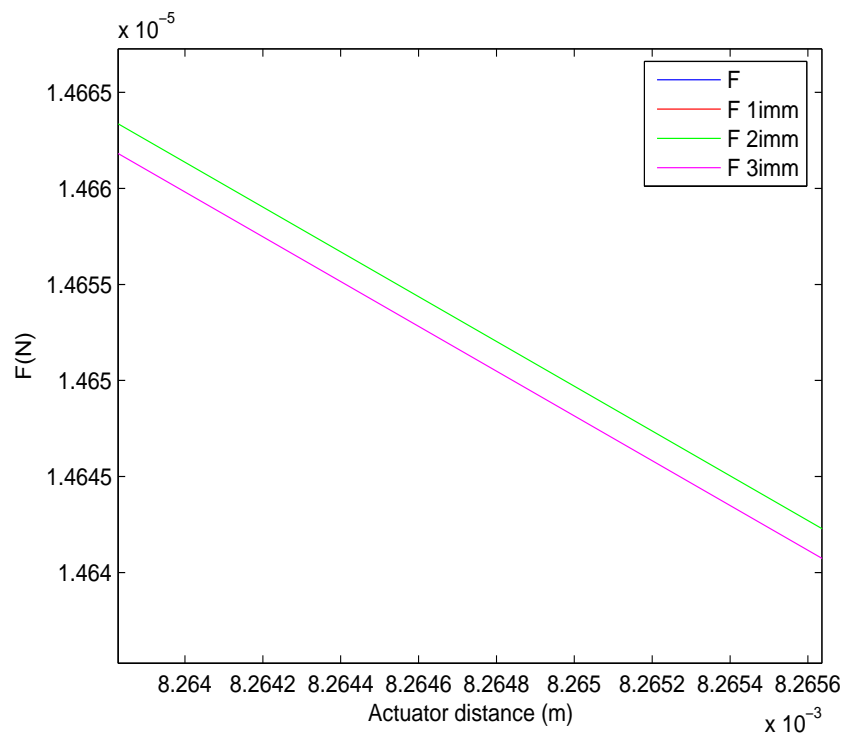


Figure 3.11: A zoom of the equivalent simulation of the force.

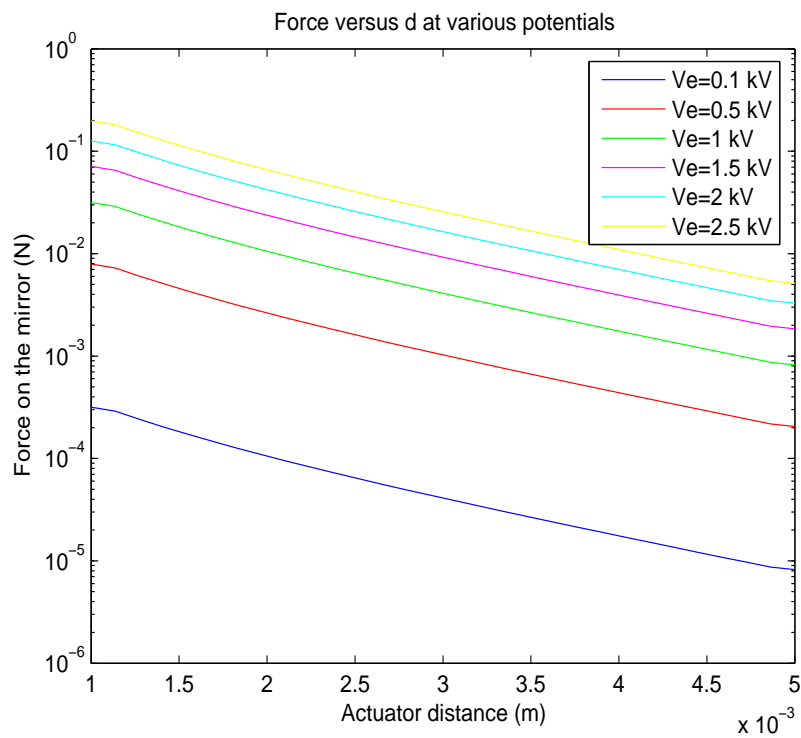


Figure 3.12: Force versus the actuator distance at various potentials.

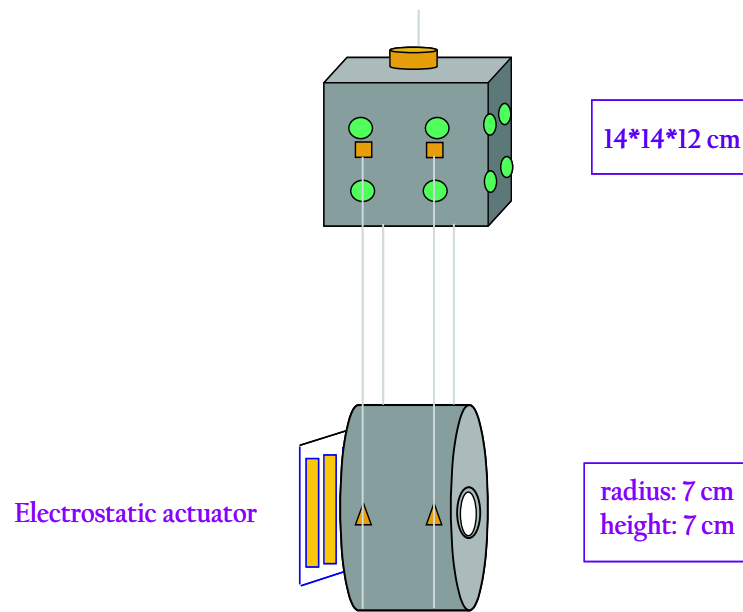


Figure 3.13: A scheme of the double pendulum suspension used to test the electrostatic actuator.

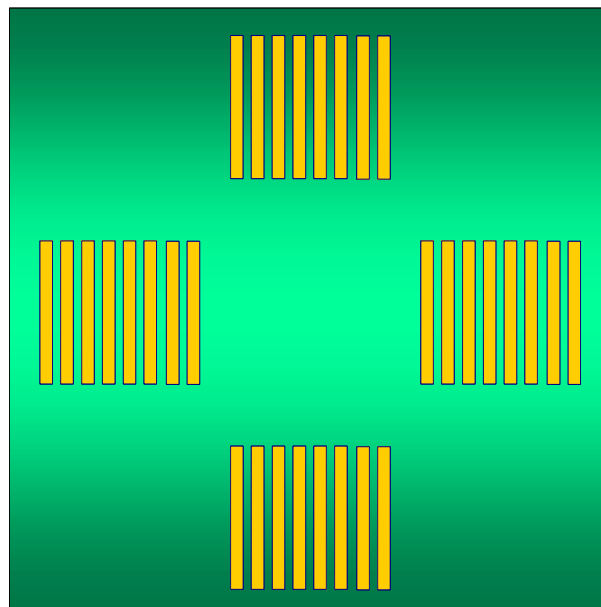


Figure 3.14: New electrostatic actuator designed to control the longitudinal and rotational degrees of freedom: we can note four different groups of strips of electrodes, each one with its independent alimentation.

splitter, first interferometer mirror IM1 and the two mirrors MA and MB) are all mounted on the lower stage of a double pendulum suspension, as we can see in fig. 3.17. This arm of the interferometer has been bent in order to suspend all the optical components to the same suspension: L_1 , the total length of this arm from the beam splitter BS to IM1, is given by $L_1 = a + b + c$. This interferometer arm is free to move

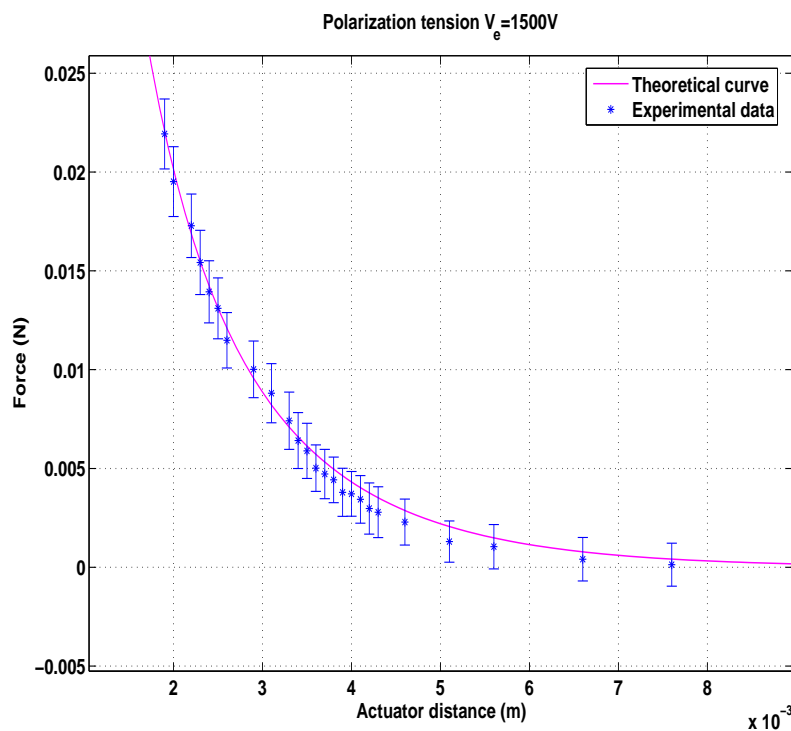


Figure 3.15: Comparison between theoretical force as a function of the distance and experimental data for the designed electrostatic actuator.

longitudinally, while the position of its upper stage is controlled in both rotational and pendular degrees of freedom. The second interferometer mirror IM2 is suspended independently to the lower stage of a similar double pendulum suspension, and its position is controlled, in both rotational and longitudinal degrees of freedom, by the use of the electrostatic actuator. The length of this arm L_2 is simply the distance from the beam splitter BS to IM2.

Fig. 3.18 shows the fringes of interference before and after the locking of the interferometer.

First driving of the electrostatic actuator in AC

This subsection contains the last important result obtained in this work about the electrostatic actuation. The actuator is sensitive to electrostatic charges present on the dielectric mirror mass: this causes a low frequency drift in the position of the mirror.

This limitation has been removed by applying a sinusoidal voltage instead of a continuous voltage to the actuator to put the mirror in the working position.

Fig. 3.19 shows the time evolution and the corresponding spectrum of the rotational (tx and ty) and longitudinal (zd) degrees of freedom of the double pendulum suspension with the upper stage controlled using the coil-magnet system and the lower stage without control: as we can see the amplitude of the free

pendulum motion of the lower stage is about $10\mu m$.

Fig. 3.19 shows the time evolution and the corresponding spectrum of the same quantities with the upper stage controlled using the coil-magnet system and the lower stage controlled using the electrostatic actuator driven in AC: in this situation the amplitude of pendulum motion of the lower stage reduces to $1\mu m$.

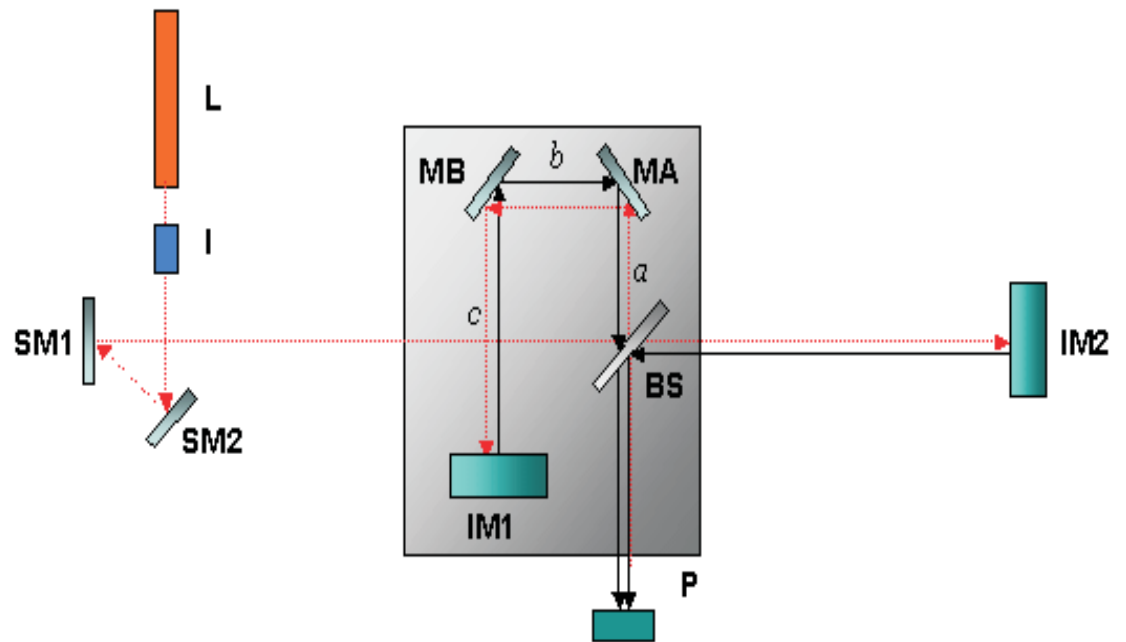


Figure 3.16: A view from the above of the suspended Michelson interferometer: L represents the laser source, a He-Ne @ 632.8 nm, I is the Faraday isolator, SM1 and SM2 are two steering mirrors used to match the laser beam into the interferometer, BS is the beam splitter, IM1 and IM2 the terminal mirrors, P is the photodiode. The first arm of the interferometer is bent by the use of the mirrors MA and MB and suspended to the same pendulum suspension. The second arm mirror IM2 is suspended independently to a similar pendulum suspension.

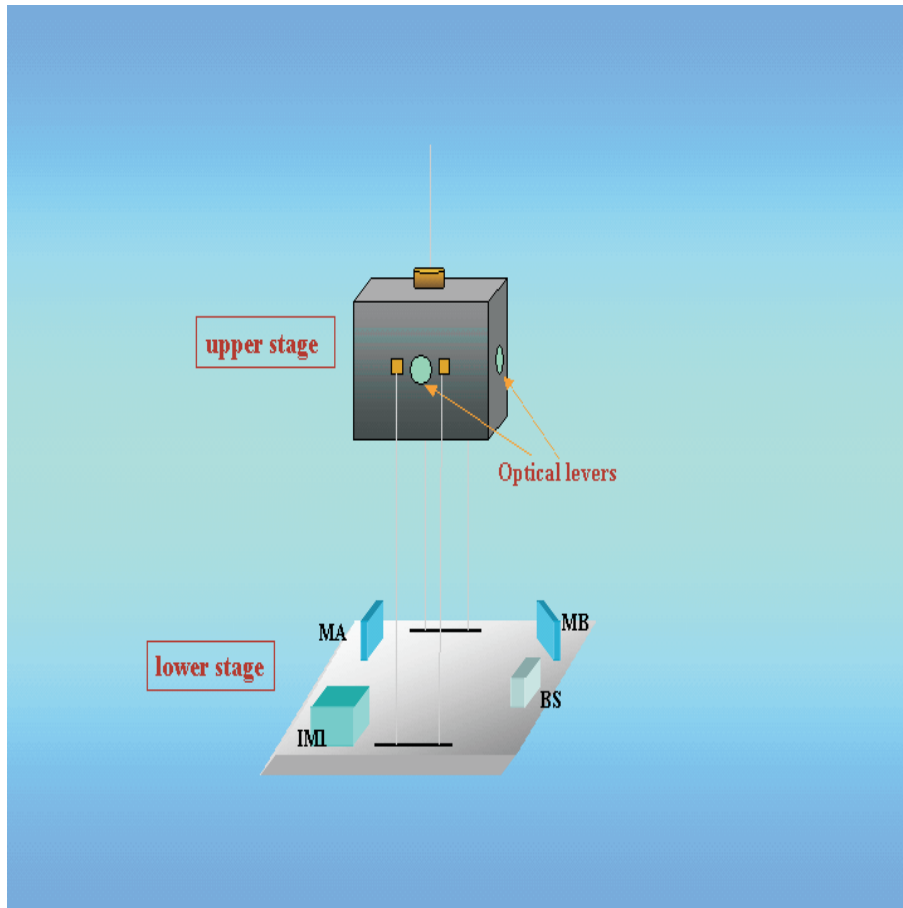


Figure 3.17: First arm optics for the Michelson interferometer suspended to the lower stage of a double pendulum: IM1 represents the first terminal mirror, the mirrors MA and MB are used to bent this first arm and suspend it all to the same pendulum.

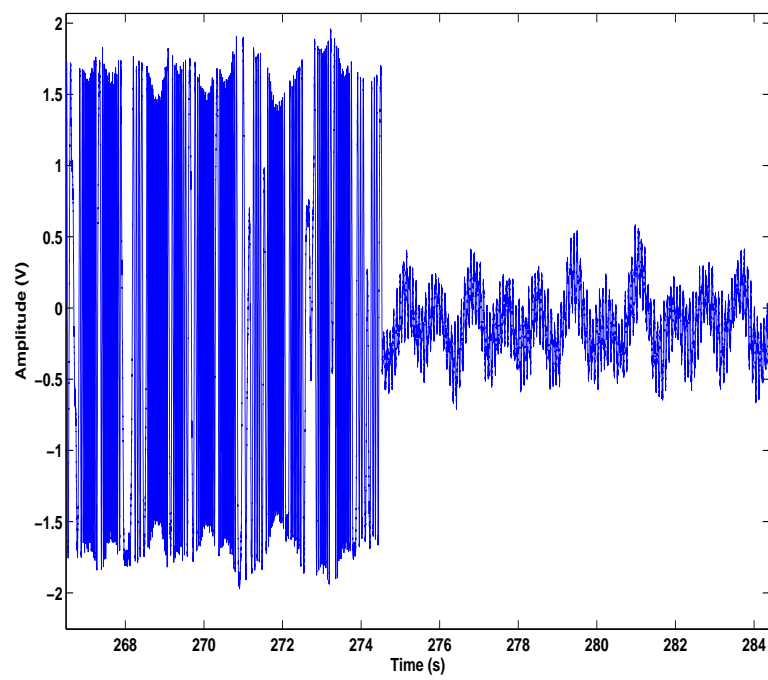


Figure 3.18: The transmission figure of the suspended Michelson interferometer before and after the locking.

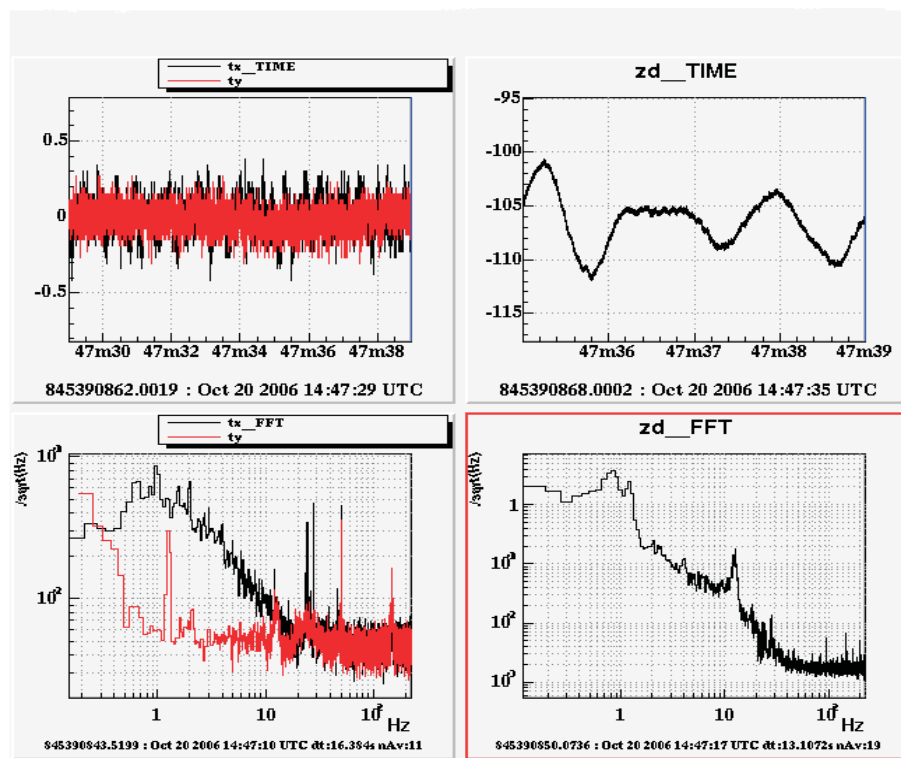


Figure 3.19: Time evolution (upper pictures) and the corresponding spectrum (lower pictures) of the rotational (tx and ty) and longitudinal (zd) degrees of freedom of the double pendulum suspension with the lower stage without control.

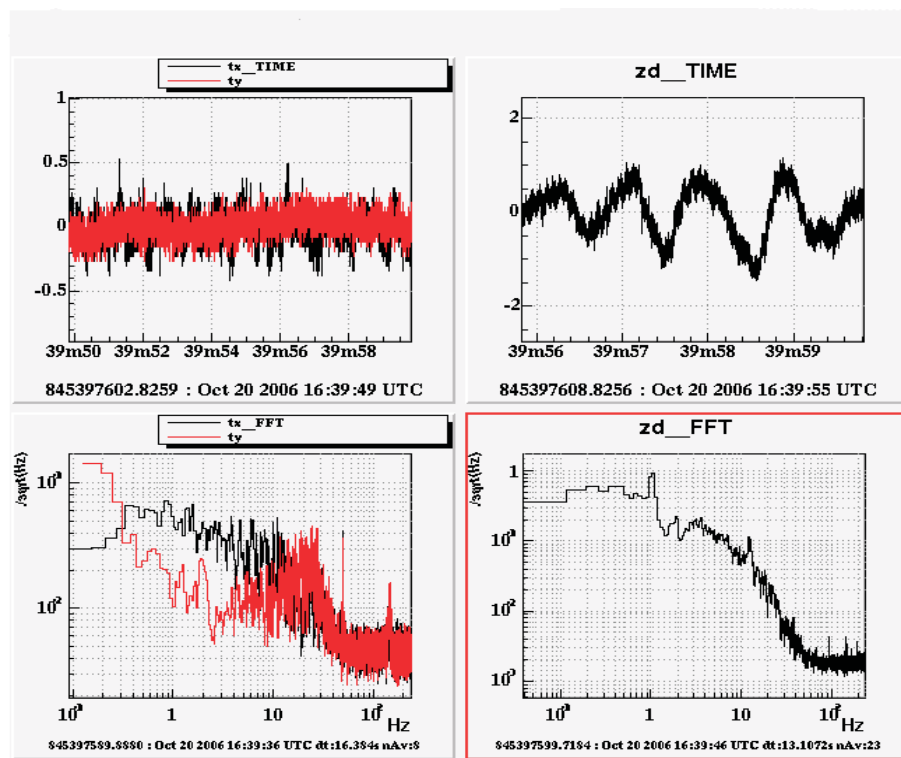


Figure 3.20: Time evolution (upper pictures) and the corresponding spectrum (lower pictures) of the rotational (tx and ty) and longitudinal (zd) degrees of freedom of the double pendulum suspension with the lower stage controlled using the electrostatic actuator driven in AC.

Chapter 4

Fabry Perot seismic sensor and experimental data

In this chapter we will describe in detail the seismic sensor, made up of a Fabry Perot interferometer developed in this thesis work.

The Fabry Perot interferometer and its working principle have already been described in chapter 2, while we will now investigate the use of this particular and very sensitive instrument as a seismometer.

We will thus describe the experimental set-up and the various steps required to acquire the motion of the ground with respect to a fixed reference (in a given band of frequencies).

At the end we will show the experimental data and discuss about possible future application for this device.

4.1 Experimental set-up

4.1.1 Optical components for the Fabry Perot interferometer

A scheme of the Fabry Perot interferometer is shown in fig. 4.1.

The path of the light is the following: the laser light @ 532 nm passes through the half wave plate $\Lambda/2$ and the polarizer P, then enters the Faraday Isolator FI; at this point the direction of the laser beam into the cavity is optimized through the use of the three steering mirrors S1, S2, S3, while the transverse dimension is optimized through the use of the matching lense ML.

The light enters the beam splitter BS, which sends a part of the light reflected by the cavity to the photodiode Pd1 through the lense DL1.

Finally the light enters the cavity and the transmitted light is collimated on a second photodiode Pd2 by the use of the lense DL2.

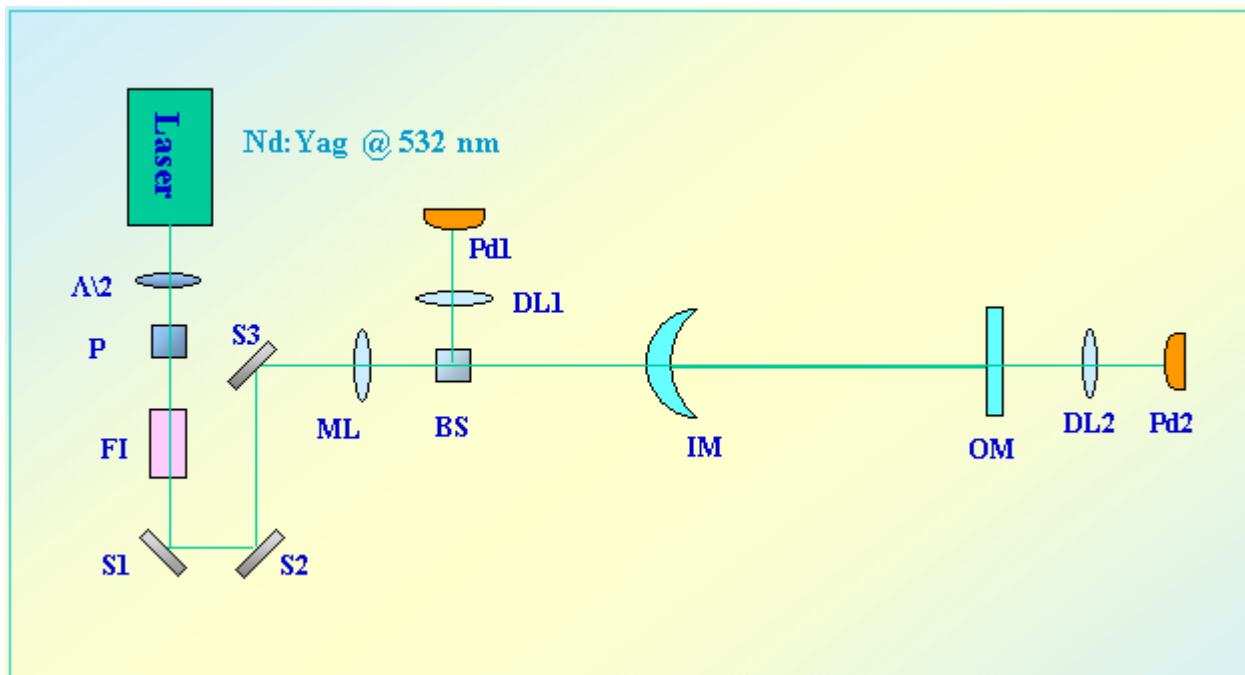


Figure 4.1: A scheme of the Fabry Perot seismometer.

In the following section we will analyze the optical properties of the various components used to build up our interferometer.

Laser source

The laser source is a Nd:YAG laser [31] [32] produced by Innolight emitting 2 Watts @ 1064 nm and 0.5 Watts @ 532 nm. This laser system consists of three self contained units: the laser head, the laser control electronics unit, and the frequency doubling electronics unit.

This laser (fig. 4.2) contains basically the following components: two diode lasers which are electrically driven and provide the pump radiation for a monolithic Nd:YAG laser crystal. Some optics are required to focus the pump light into the Nd:YAG laser's fundamental mode. The fundamental emission of the monolithic Nd:YAG ring laser is single frequency at a wavelength of 1064 nm in the near infrared.

This infrared radiation is then sent through various optics into another resonator: this resonator contains a nonlinear crystal to generate the second harmonic wavelength at 532 nm and is electronically stabilized to the frequency of the infrared laser. This kind of laser has peculiar characteristics:

- very stable emission on a single longitudinal frequency
- extremely small spectral linewidth
- possibility to tune the laser frequency by changing the temperature of the monolithic laser crystal or

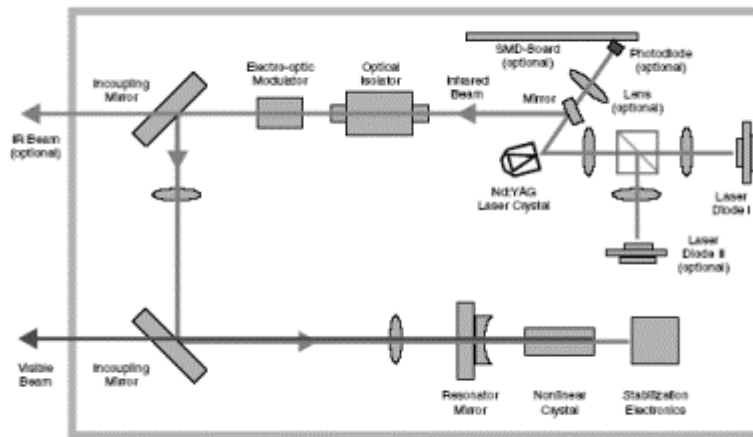


Figure 4.2: A scheme of the optical circuit of the laser: we note the YAG crystal for the emission of the infrared light at 1064 nm and the doubling cavity for the generation of the green light at 532 nm.

by applying a high voltage signal to a PZT crystal element on the laser crystal

- possibility to reduce the intensity noise of several orders of magnitude through a feedback noise reduction system: by the use of the so called *noise eater* the noise level is lowered into the proximity of the quantum noise limit

Power attenuation system: half wave plate and polarizer

As we mentioned in the previous section, the laser source emits 500 mW @ 532 nm. It is convenient in this situation to reduce somehow the optical power during the preliminary alignment of the various optics. For this reason we used a passive power attenuator, made up of a half wave plate and a polarizer. The behaviour of the wave plates is based on the physical phenomenon of birefringence, that is the change of the refractive index with the polarization of light. In this sense birefringence is used to modify the polarization state of light, through the birefringence of retardation plates.

The working principle of a passive attenuator is the following: we can ever decompose the polarization of the light on two basical directions, the *s*-direction, that is to say the vertical one, and the *P*-direction, that is to say the horizontal one.

Our laser light, linearly polarized in the *P*-plane, enters the half wave plate: the plate rotates the polarization of the light according to its rotation angle with respect to the vertical direction. In this way the light exiting the plate will have both components of the polarization, *s* and *P*, and enters the polarizer.

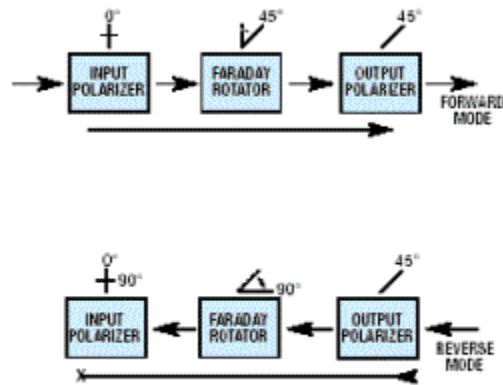


Figure 4.3: A scheme for the rotation of the polarization of the light in the forward and reverse path of light across the Faraday isolator.

This polarizer is a High Energy Nd:YAG laser polarizing cube beamsplitter produced by Newport Corporation. It is made of BK7 optical glass and is designed to provide efficient narrowband polarization for high power lasers. The polarizer consists of a pair of precision right-angle prisms optically contacted together. The incoming beam is split into two orthogonal, linearly polarized components: P -polarized light is transmitted, while s -polarized light is reflected, both with negligible absorption.

In this way, according to the rotation of the half wave plate, we can vary in a continuous way the transmitted intensity of the laser beam.

Faraday isolator

A fundamental device put on the path of the laser beam is the Faraday isolator. This instrument transmits light in one direction only, thus it is used to reduce or eliminate optical feedback, that is reflections of the laser energy back to itself, whose effects are amplitude fluctuations, noise, limitation of modulation bandwidth.

The working principle of a Faraday isolator is based on the so called Faraday effect, according to which an optically transparent piece of glass placed between two magnets becomes *optically active*, that is it can rotate the plane of polarized light that passes through it. This amount of rotation is proportional to the strength of the magnetic field and to the distance the light must pass through the medium, and is not dependent on the direction of light propagation.

A Faraday isolator is thus composed of:

- An input polarizer, oriented along the plane of the laser source, to select the initial polarization of light
- The Faraday rotator, that will rotate the plane of polarization by 45° ccw sense

- An output polarizer, oriented at 45° ccw

In this configuration we distinguish the forward mode, in which laser light enters the input polarizer and becomes linearly polarized, then enters Farady rotator and is rotated by 45° ccw and is then completely transmitted by the output polarizer.

On the contrary, in the reverse direction, light enters the output polarizer, then enters the rotator and is further rotated by another 45° , making a total of 90° with respect to the input polarizer: at this point it will be extinguished with respect to the input polarizer.

As we can see, by the use of this device, the laser light has no possibility to go back into the laser cavity.

Steering, collimation and detection optics

The three steering mirrors are commercial mirrors produced by Newport Corporation. They are circular plane mirrors with 2.54 cm diameter made with Pyrex substrate and their coating is an enhanced aluminum one with average reflectivity greater than 99 % in the wavelength range between 450-700 nm.

The matching lens and the collimation lenses on the two photodiodes are commercial lenses produced by Newport Corporation. They all are bi-convex lenses made of BK7 optical glass and their coating is an antireflection one in the wavelength range from 650-1000 nm. The focal length of the matching lens is 25 cm, while the focal lengths of DL1 and DL2 are 3.8 cm.

Cavity mirrors

We accurately designed the cavity mirrors because the performance of the Fabry Perot interferometer is strictly linked to the geometrical and optical features of these mirrors.

Our Fabry Perot is a plane-concave one: the input mirror is the concave one, with a radius of curvature $R=514$ mm, while the output mirror is plane, with infinite radius of curvature. Such asymmetric configuration gives us the capability of distinguishing the behavior of the two mirrors, and, as a consequence, what happens to the reference or to the free mirror.

The substrate of these mirrors is made of BK7 optical glass and the coating is a dielectric one with reflectivity around 98 % @ 532 nm: the theoretical *finesse* of the cavity is around 70.

4.2 Fabry Perot with two fixed mirrors: first experimental data

4.2.1 Optical bench transfer function

The whole optical circuit has been mounted on an optical bench: this means that the optical cavity is sensitive to displacements on the optical bench. As our final target is a measure of the motion of the ground, we measured the transfer function of the optical bench with respect to the ground.

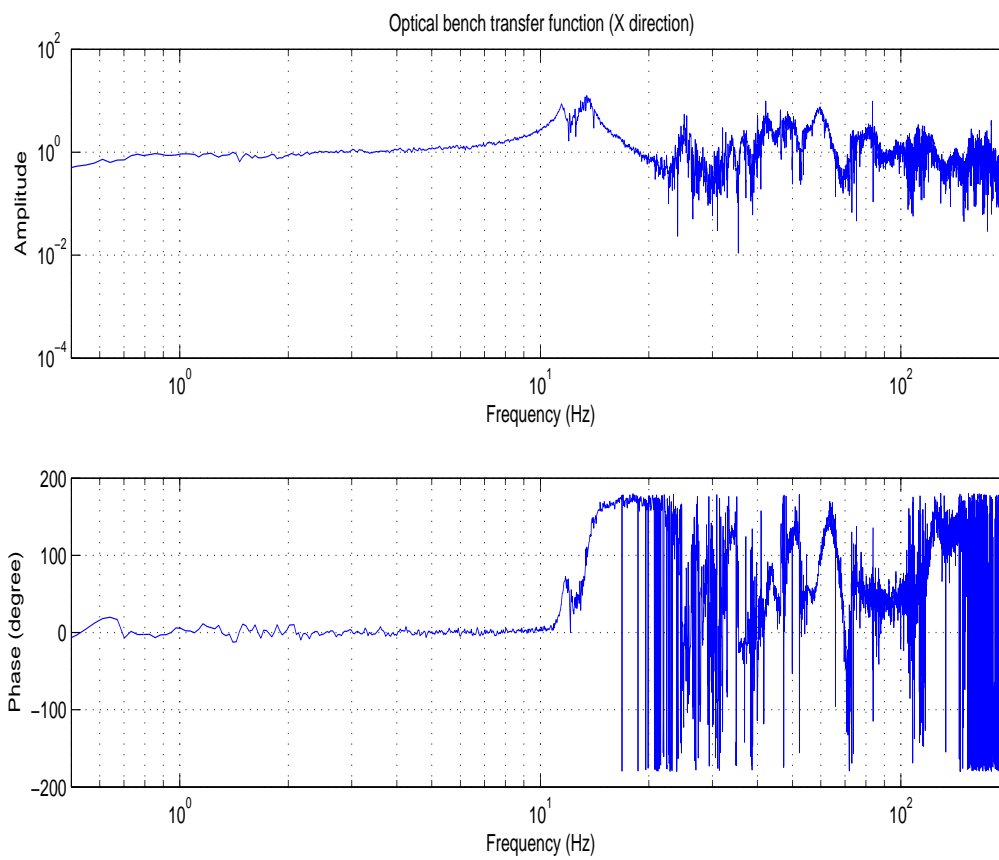


Figure 4.4: Optical bench transfer function along the Episensor X -axis (rigid bench respect to the ground).

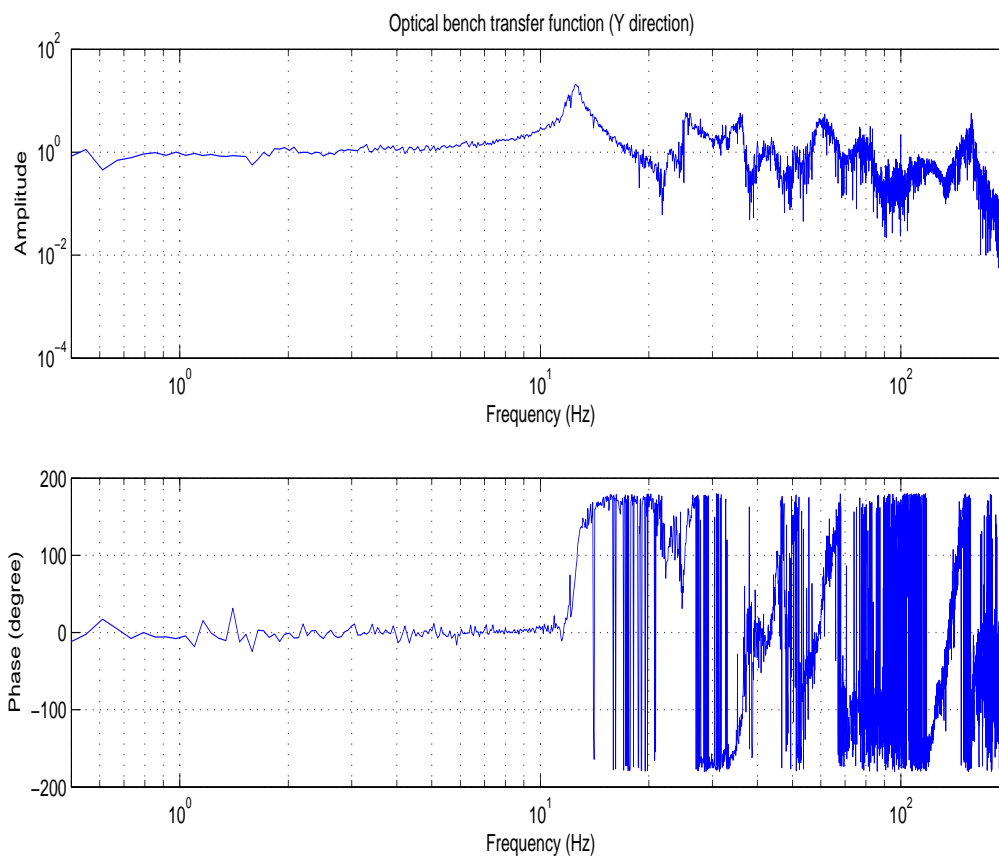


Figure 4.5: Optical bench transfer function along the Episensor Y -axis (rigid bench respect to the ground).

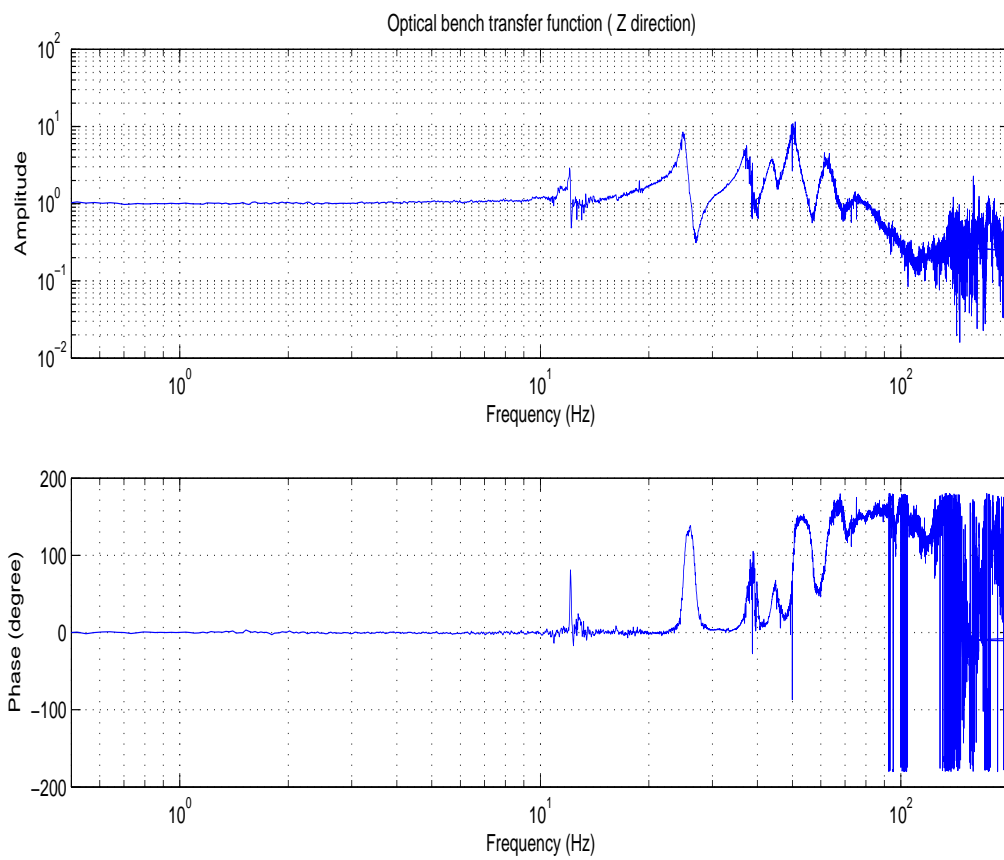


Figure 4.6: Optical bench transfer function along the Episensor Z-axis (rigid bench respect to the ground).

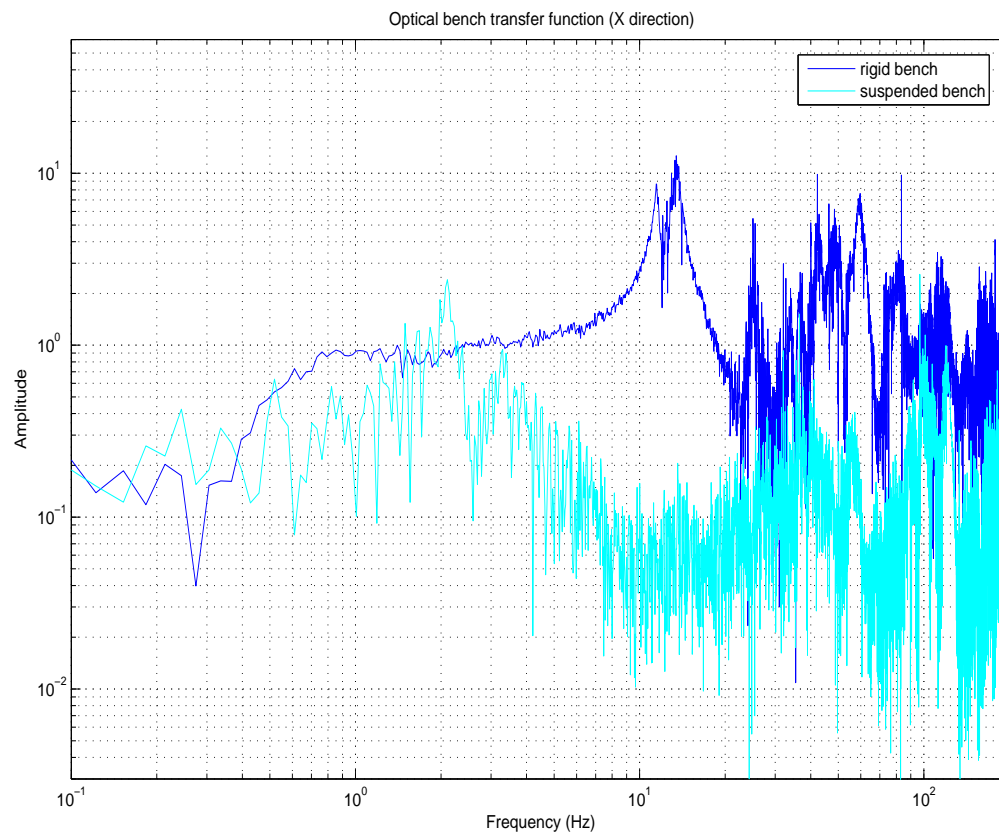


Figure 4.7: Optical bench transfer function along the Episcensor X -axis: comparison between rigid and suspended bench.

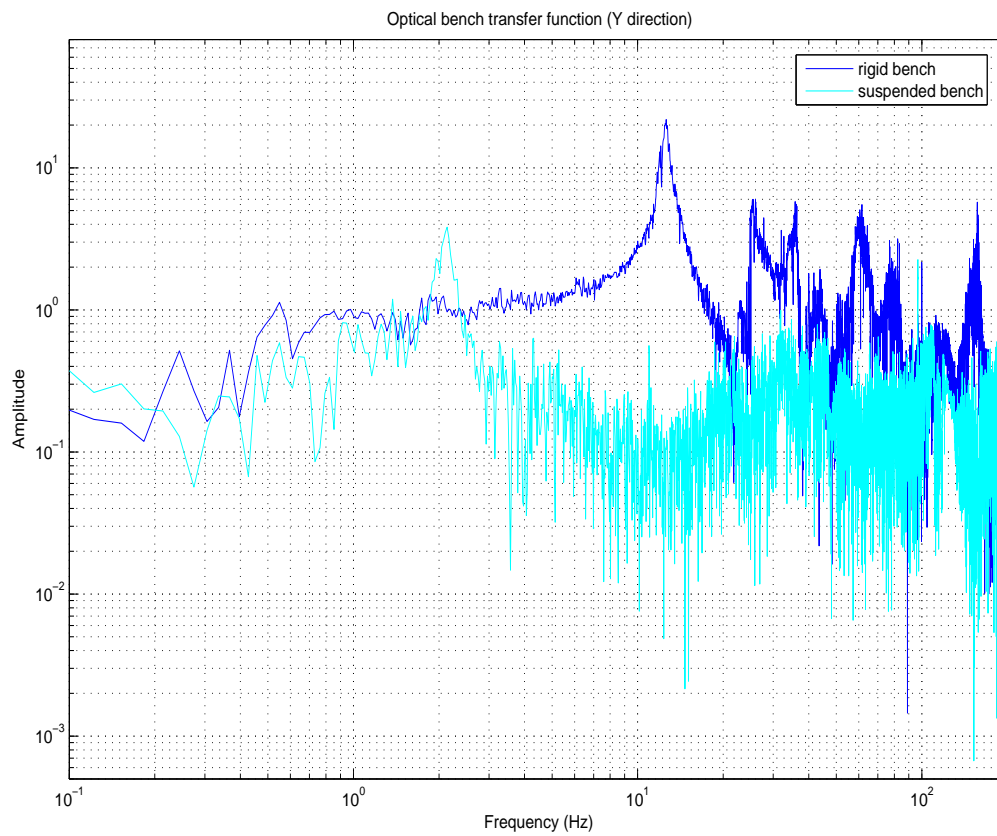


Figure 4.8: Optical bench transfer function along the Episensor Y -axis: comparison between rigid and suspended bench.

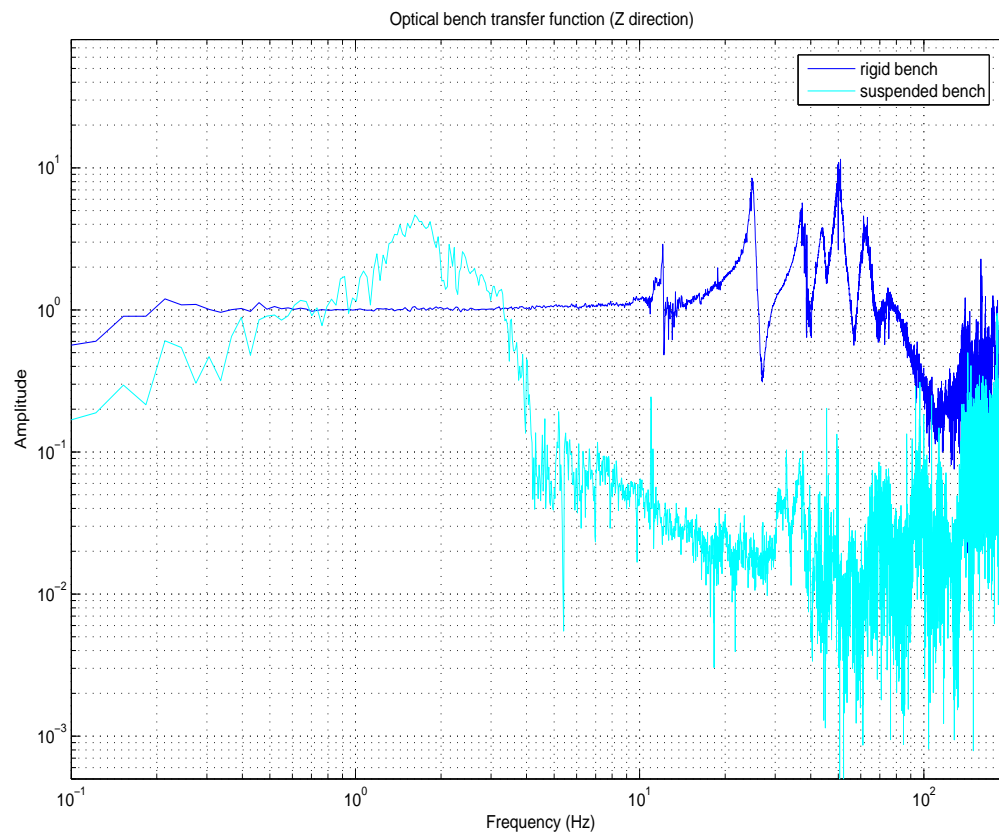


Figure 4.9: Optical bench transfer function along the Episensor Z -axis: comparison between rigid and suspended bench.

We used two Episensor FBA ES-T, triaxial accelerometers optimized for earthquake recording with bandwidth from DC to 200 Hz. One Episensor has been mounted on the optical bench, with the Y -axis oriented along the optical axis of the Fabry Perot, while the other one has been put on the ground, in the proximity of the optical bench, oriented as the first one.

We computed the transfer function using several hours of data acquired in two different conditions. In the first configuration, the optical bench was rigidly connected to the ground; in the second configuration the optical bench was disconnected from the ground using the damping mechanism of the table legs: in this way the bench results *suspended* from the ground the frequency band after its mechanical resonance.

In fig. 4.4, 4.5, 4.6 we show the measured transfer functions on the X, Y and Z direction computed with the optical bench connected to the ground.

In fig. 4.7, 4.8, 4.9 we show the comparison between the same transfer functions computed in the two different conditions of rigid and suspended bench. As we can see, the configuration with the suspended bench offers a better isolation from the ground noise, except for the region around 2 Hz, corresponding to the mechanical resonance frequency of the bench structure.

4.2.2 Piezo actuator transfer function

In the first phase of mounting and alignment of the Fabry Perot cavity we positioned both the input and output mirror on the optical bench by means of ordinary mechanical supports for this kind of optics.

In this configuration the input mirror is provided of a piezoelectric crystal to adjust the length of the cavity L on the resonance one. This piezo is produced by Physik Instruments: it is a multi axis tip/tilt platform and Z-positioner based on a piezo tripod design. All three piezo linear actuators can be driven individually by a three-channel amplifier servo-controller. This kind of device provides longitudinal movement up to 12 μm and tilt movement up to 1.2 mrad with sub-msec response.

In order to characterize the dynamical response of the actuation system we measured the transfer function of the piezo actuator: we sent to the piezo driver white noise filtered at 50 Hz and used a simple optical lever with a Position Sensing Photodiode to read the displacements.

In fig. 4.10 we find the measured transfer function: as we can see there are two resonances, typical of a more complex system than a simple mechanical structure, as the piezo one. This particular shape of the transfer function is due to the combined system of the piezo and the mechanical mounting of the mirror.

4.2.3 Mode matching and alignment of the interferometer

After characterizing the various parts of the experimental set-up from an optical, mechanical and dynamical point of view, we aligned the cavity.

We know that the cavity waist for a plane concave resonator is situated on the plane mirror and its radius

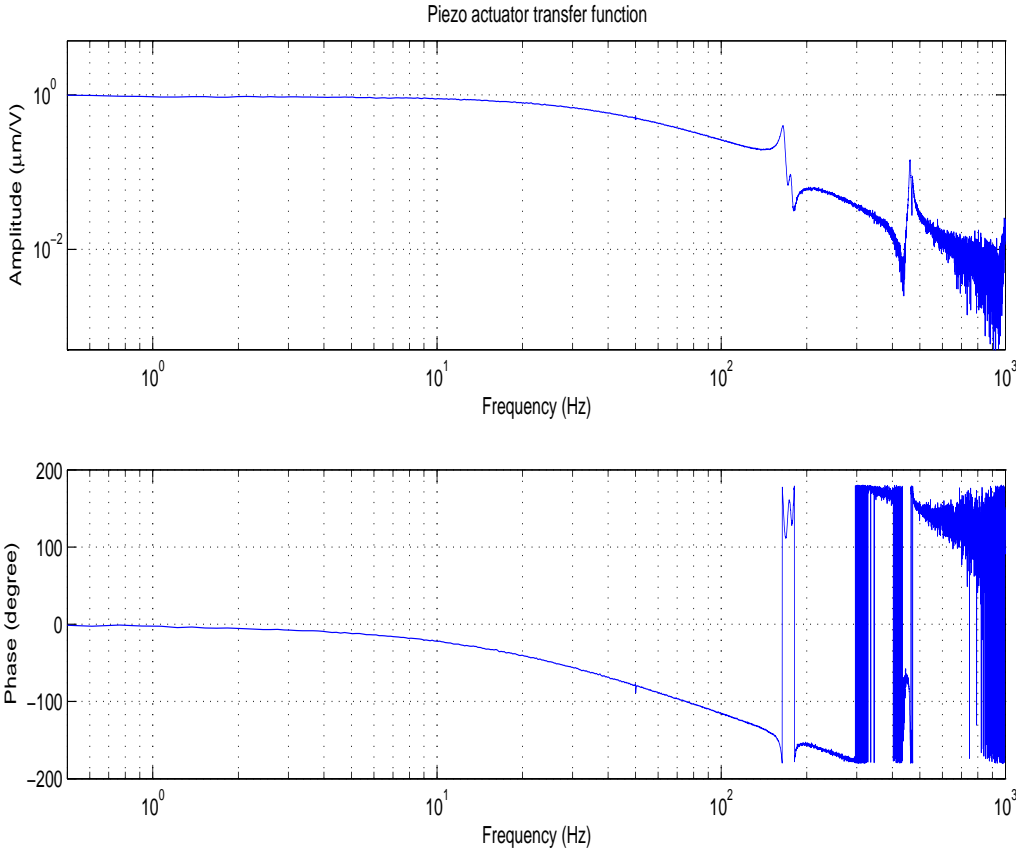


Figure 4.10: Piezo actuator transfer function.

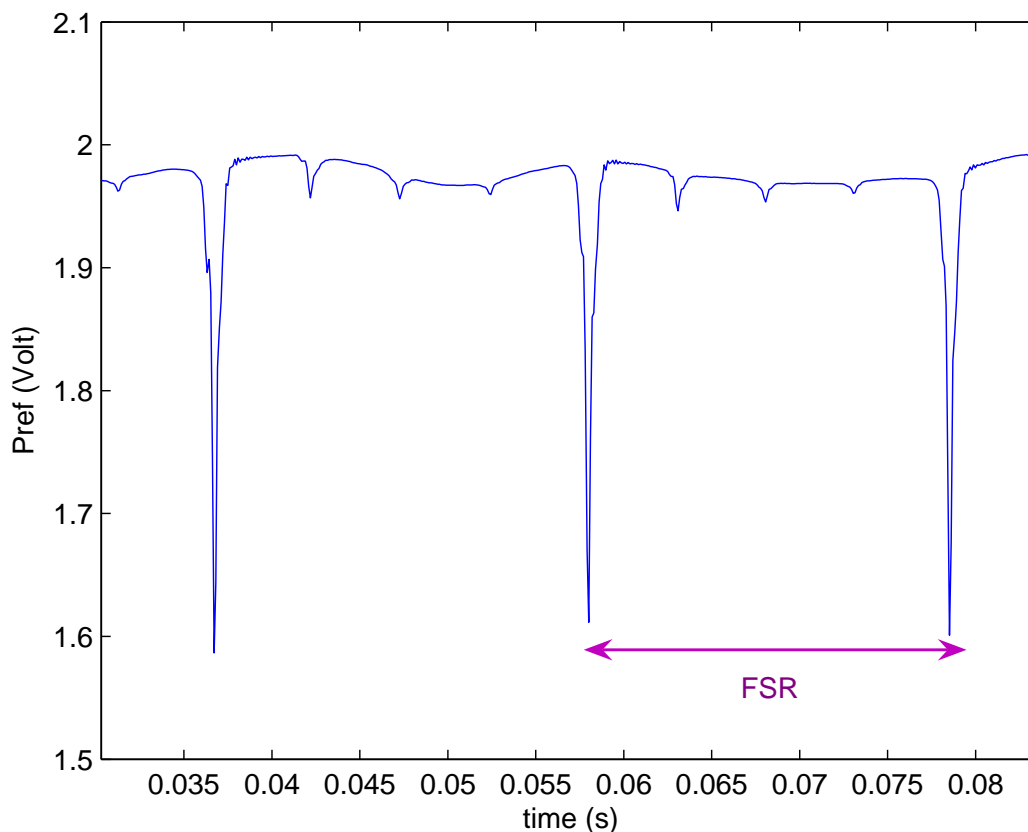


Figure 4.11: A detail of the power reflected by the cavity: it is indicated the Free Spectral Range (FSR), the frequency distance between two longitudinal frequencies.

is given by: $w_0^2 = \frac{\lambda}{\pi} \sqrt{L(R-L)}$. Its value is $147\mu m$.

Measurement of the cavity *finesse*

As we told before, one of the most important optical parameters of a cavity is its *finesse*, that is linked to the width of the resonances and to the number of reflections of the beam into the cavity: the higher the *finesse*, the higher the number of bounces of the laser beam into the Fabry Perot.

In order to obtain an experimental value for the *finesse* we made several acquisitions of the reflected cavity power. From the theory we know that the resonance peak has a lorentzian shape with expression:

$$g(\omega - \omega_0) = \frac{1}{1 + \left(\frac{\omega - \omega_0}{\Delta\omega_0/2}\right)^2}. \quad (4.1)$$

Thus we performed a lorentzian fit on the data to estimate the full width at half maximum $\Delta\omega_0$. Once obtained it, we can estimate the *finesse* from the simple formula: $F = FSR/\Delta\omega_0$. In fig. 4.11 we find the transmitted power with the indication of the free spectral range, while in fig. 4.12 we find the corresponding

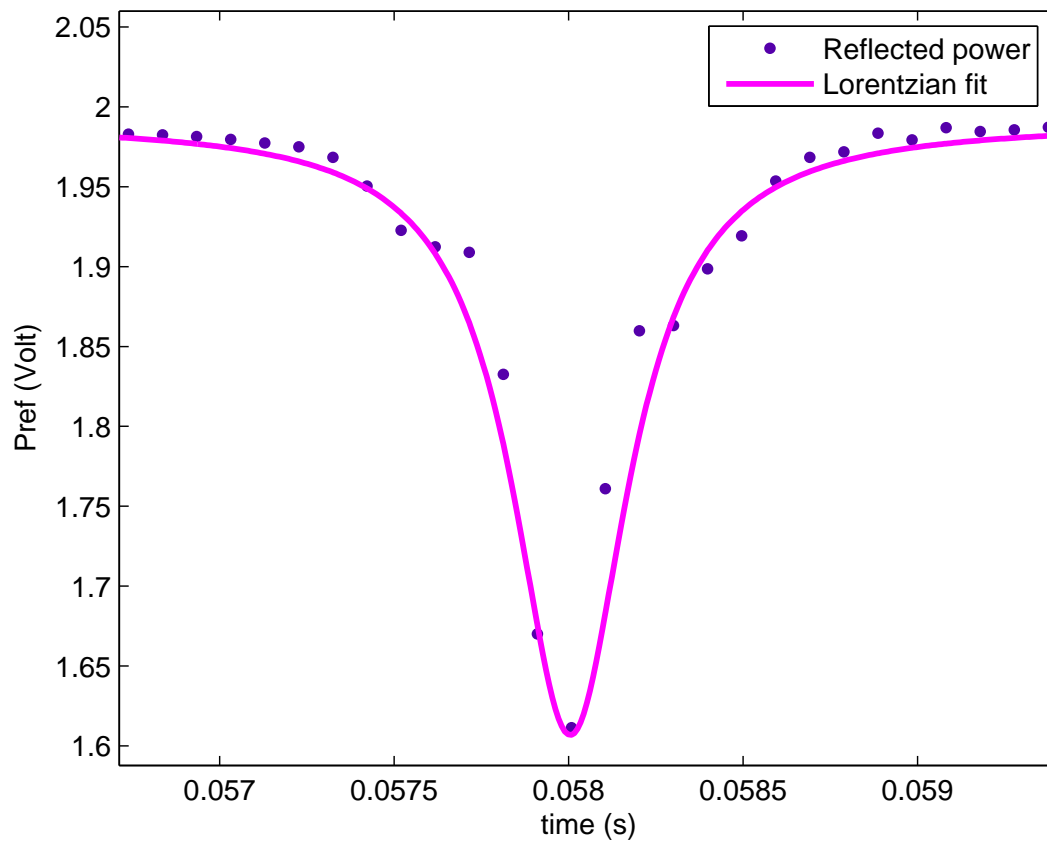


Figure 4.12: Comparison between the reflected cavity power and the corresponding lorentzian fit.

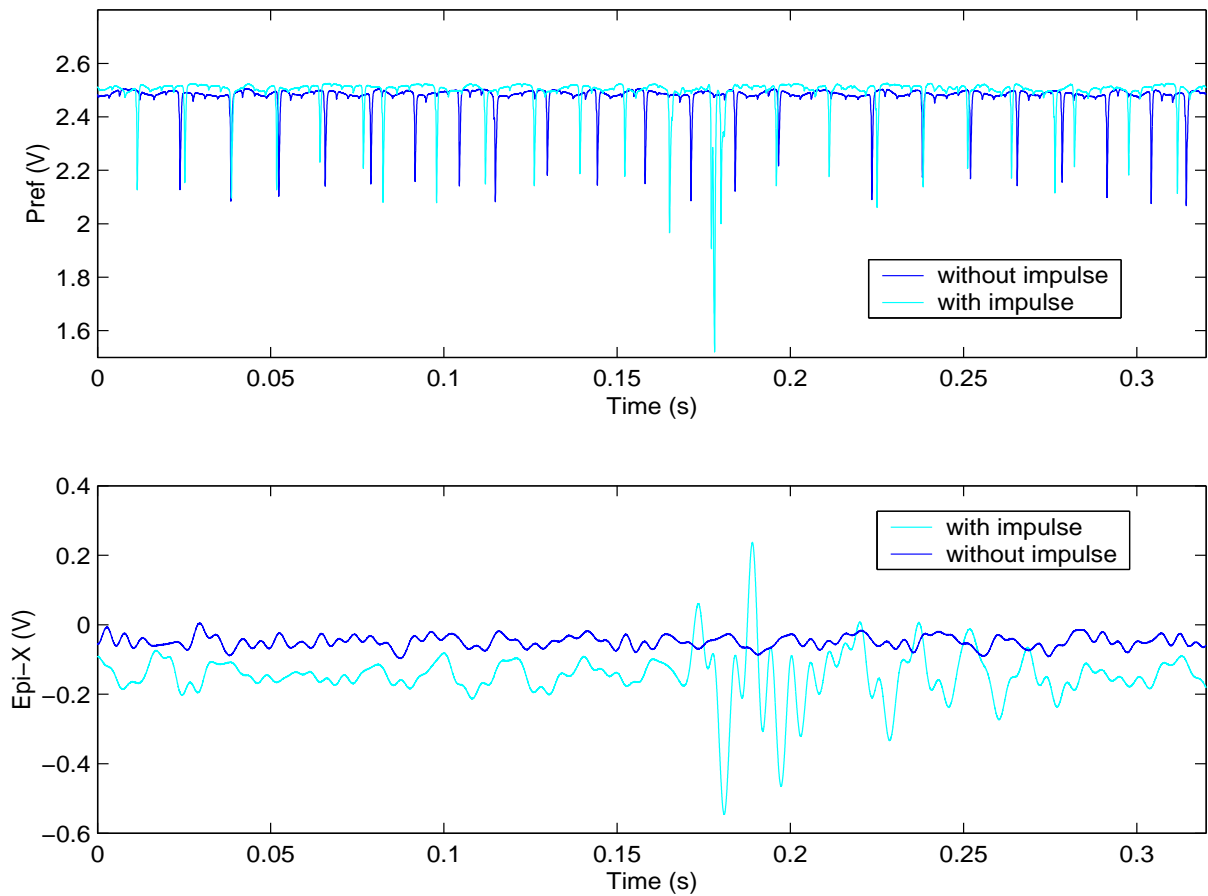


Figure 4.13: Comparison between the Fabry Perot response with and without an impulse from the ground (upper picture). The lower picture shows the same comparison for the Episensor response in the X -direction.

lorentzian fit on the peak used for the measure.

4.2.4 First comparison between Episensor and Fabry Perot

One of the first tests performed on the Fabry Perot cavity was to generate an impulse on the ground and study its response, together with the response of the Episensor along the various directions.

In fig. 4.13, 4.14, 4.15 we find the superposition of the reflected power with and without impulse and the same comparison for the Episensor response. As we can see the Fabry Perot cavity is very sensitive to the impulse: firstly the resonance peak becomes higher and secondly there is a change in the relative speed of the mirrors.

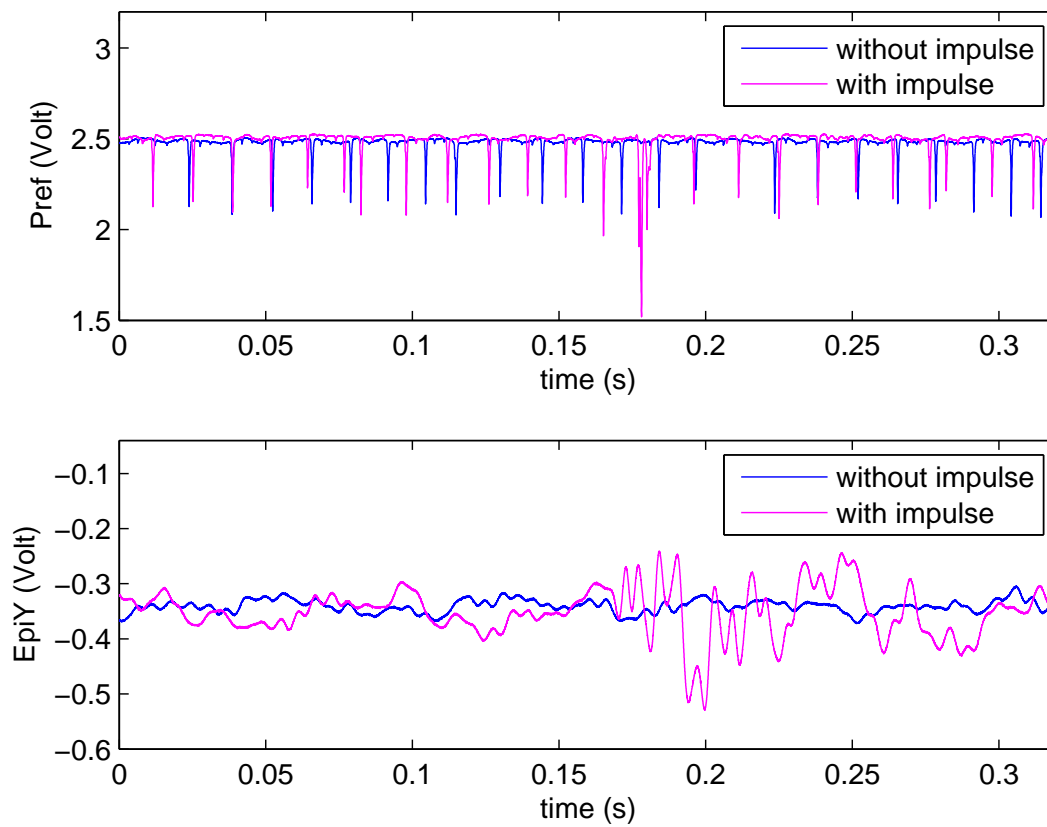


Figure 4.14: Comparison between the Fabry Perot response with and without an impulse from the ground (upper picture). The lower picture shows the same comparison for the Episcensor response in the Y-direction.

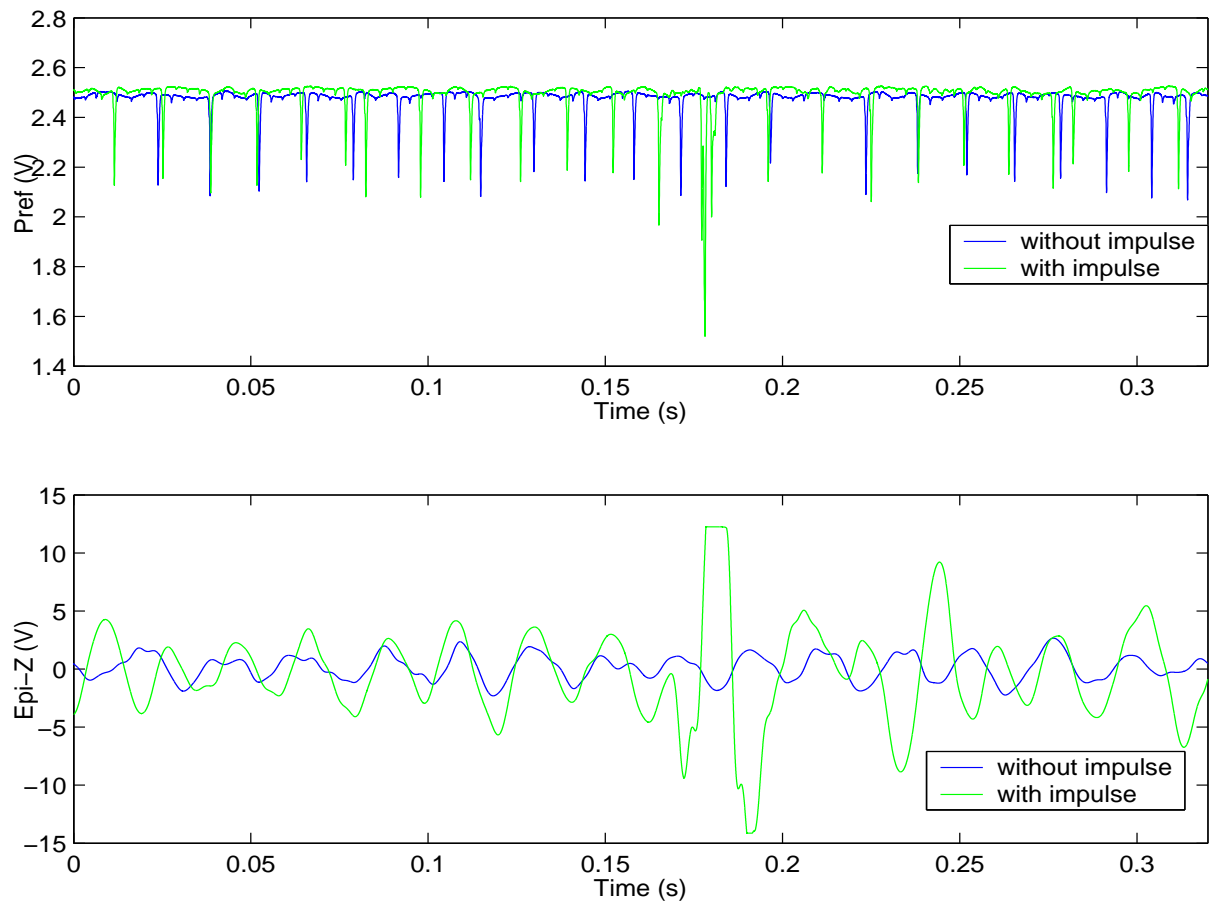


Figure 4.15: Comparison between the Fabry Perot response with and without an impulse from the ground (upper picture). The lower picture shows the same comparison for the Epi-Z response in the Z-direction.

4.3 Signal reconstruction algorithm: basic theory and experimental data

4.3.1 Signal reconstruction algorithm: basic theory

In this subsection we will describe the non-linear signal extraction technique used to obtain a signal proportional to the length of the Fabry Perot cavity [33]. This method is based on a mechanical frequency modulation plus a suitable fringe counting technique.

The basic assumptions for the correct application of this technique are:

- the laser linewidth is much smaller than the FWHM of the FP resonance, thus we can consider the source as monochromatic
- the mirror motion is much slower than the cavity storage time, so we can consider the cavity as adiabatic
- the laser beam is properly matched and aligned with respect to the cavity, so that we can consider only the fundamental mode and neglect the effect of the higher order modes

Signal extraction

We know from the theory that the transmitted or reflected intensity by the Fabry Perot cavity repeats every time we change the frequency of a FSR or the cavity length of $\lambda/2$.

Let us suppose that we add to the phase shift due to a round trip a term changing sinusoidally with an amplitude equal to π : this can be achieved either by changing the cavity length by $\lambda/4$ or shifting the laser frequency by $c/(4L)$. In this work we will change the cavity length using the piezoelectric actuator. In this way the phase δ can be expressed as:

$$\delta(t) = 2\pi \left(\frac{2L(t)}{\lambda} + \frac{1}{2} \cos(\omega_m t) \right), \quad (4.2)$$

where $L(t)$ is the deviation from the length corresponding to a given resonance peak, and we have neglected terms multiple of 2π .

The signal $V(t)$ at the output of the photodiode is proportional to the reflected power: if we choose a threshold $V_T = \alpha V_{\min}$, with $0 < \alpha < 1$, V_{\min} being the minimum photodiode voltage, corresponding to the minimum FP reflection, when the signal is below threshold we have:

$$\delta(t) \simeq 2N\pi \Rightarrow L(t) \simeq -\frac{\lambda}{4} \cos(\omega_m t) + N(t) \frac{\lambda}{2}. \quad (4.3)$$

The last expression is correct with a maximum error lower than $(\lambda/F)\sqrt{1/\alpha - 1}$.

The technique is based on the previous equality: all the times $t \equiv t_k$ at which the signal crosses the threshold, we sample the deviation from the nearest resonance by putting:

$$L'_{\text{out}}(t_k) = -\frac{\lambda}{4} \cos(\omega_m t_k). \quad (4.4)$$

In other words, when the signal is below the threshold we know that the sum of the instantaneous deviation resonance due to the relative motion of the low frequency mirrors plus the one due to the mechanical modulation is zero (apart an integer multiple of $\lambda/2$) and then, since the instantaneous modulation amplitude is known, the instantaneous FP motion can be extracted.

The choice of the modulation amplitude by exactly $\lambda/4$ implies that the signal crosses the threshold twice per modulation period, regardless of the actual free FP motion. A remarkable characteristic is that, thanks to the modulation, we can sample the FP low frequency motion also when the length is not an integer multiple of $\lambda/2$ and the cavity is out of resonance.

The signal $L'_{\text{out}}(t_k)$ is correct with an error that can be an integer of $\lambda/2$. For this reason the output signal jumps by $\lambda/2$ all the times that the FP is crossing one more fringe. By adding to L'_{out} the right number $N(t_k)$ of $\lambda/2$, with a suitable fringe counting technique, it is possible to recover completely the FP motion:

$$L_{\text{out}}(t_k) = L'_{\text{out}}(t_k) + N(t_k). \quad (4.5)$$

To count the fringes in the right way we have to impose the continuity of the FP length variations: all the times that L'_{out} has a discontinuity larger than $\lambda/4$ we count a new fringe. In particular if $L'_{\text{out}}(t_k) < L'_{\text{out}}(t_{k-1})$ we put $N(t_k) = N(t_{k-1}) + 1$, while if $L'_{\text{out}}(t_k) > L'_{\text{out}}(t_{k-1})$ we put $N(t_k) = N(t_{k-1}) - 1$.

In this way the FP motion is completely reconstructed according to eq. (4.5).

Constraints on modulation and sampling frequencies

If the FP length oscillates sinusoidally with an amplitude A_0 and frequency f_p , the number of counted fringes is:

$$N = \text{int} \left[\frac{2A_0}{\lambda} \sin(\omega_p t) \right], \quad (4.6)$$

with N an integer number; the maximum rate of fringe counting is:

$$\dot{N}_{\text{max}} = \omega_p \frac{2A_0}{\lambda}. \quad (4.7)$$

In the more general case that the motion is the superposition of various oscillation frequencies, we must substitute $\omega_p A_0$ with the maximum relative velocity \dot{L}_{max} .

As this technique is actually some kind of uneven sampling of the cavity length, according to the sampling theorem the minimum modulation frequency should be larger than twice the maximum frequency of fringe counting:

$$f_m \geq 2f_{\text{max}} = 8\pi \frac{A_0}{\lambda} f_p. \quad (4.8)$$

Similar arguments hold for the minimum sampling frequency for the digital system used to implement the algorithm. If we put the threshold at $V_T = \alpha V_{\min}$, the signal stays below threshold for the time necessary to shift by $(\lambda/2F)\sqrt{1/\alpha - 1}$. Then the minimum time is:

$$t_{\min} = \frac{\lambda}{2F\dot{L}_{\max}}\sqrt{1/\alpha - 1}. \quad (4.9)$$

As a consequence the minimum sampling frequency, in the assumption of sinusoidal motion, should be:

$$f_s \geq \frac{2F}{\lambda\sqrt{1/\alpha - 1}}\dot{L}_{\max} = \frac{4\pi F}{\sqrt{1/\alpha - 1}}\left(\frac{f_m}{4} + \frac{A_0}{\lambda}f_p\right). \quad (4.10)$$

If we use the minimum modulation frequency $f_m = 8\pi(A_0/\lambda)f_p$, we obtain for the minimum sampling frequency:

$$f_s \geq \frac{4\pi(2\pi + 1)F}{\sqrt{1/\alpha - 1}}\frac{A_0}{\lambda}f_p. \quad (4.11)$$

The closer the threshold to the resonance, the higher the required sampling frequency.

4.3.2 Reconstruction of longitudinal motions

In order to test the fringe counting algorithm and to optimize it, we made several measurements imposing different motions on the input cavity mirror and reconstructing them through the use of this algorithm.

Reconstruction of a sinusoidal motion

The aim of the first test was to impose through the piezo actuator a longitudinal sinusoidal motion, with frequency of 0.8 Hz, to the input cavity mirror. This frequency corresponds to the first resonance frequency of the double pendulum suspension planned to be used in the following set of measures. In fig. 4.16 we show the superposition of the real sinusoidal motion at 0.8 Hz with the one reconstructed by the use of the fringe counting algorithm with a modulation frequency of 30 Hz, while in fig. 4.17 we show the superposition of the real sinusoidal motion at 0.8 Hz with the one reconstructed by the use of the fringe counting algorithm with a modulation frequency of 50 Hz.

Reconstruction of a double sinusoidal motion

In a successive test we forced a double sinusoidal longitudinal motion on the input cavity mirror. The two frequency imposed are 0.8 Hz and 1.2 Hz, corresponding to the two resonance frequencies of the double pendulum suspension.

In fig. 4.18 and fig. 4.18 we show the corresponding experimental results.

Reconstruction of a random motion

In the last test we imposed a low frequency longitudinal random motion to the input cavity mirror, in order to study the low frequency response.

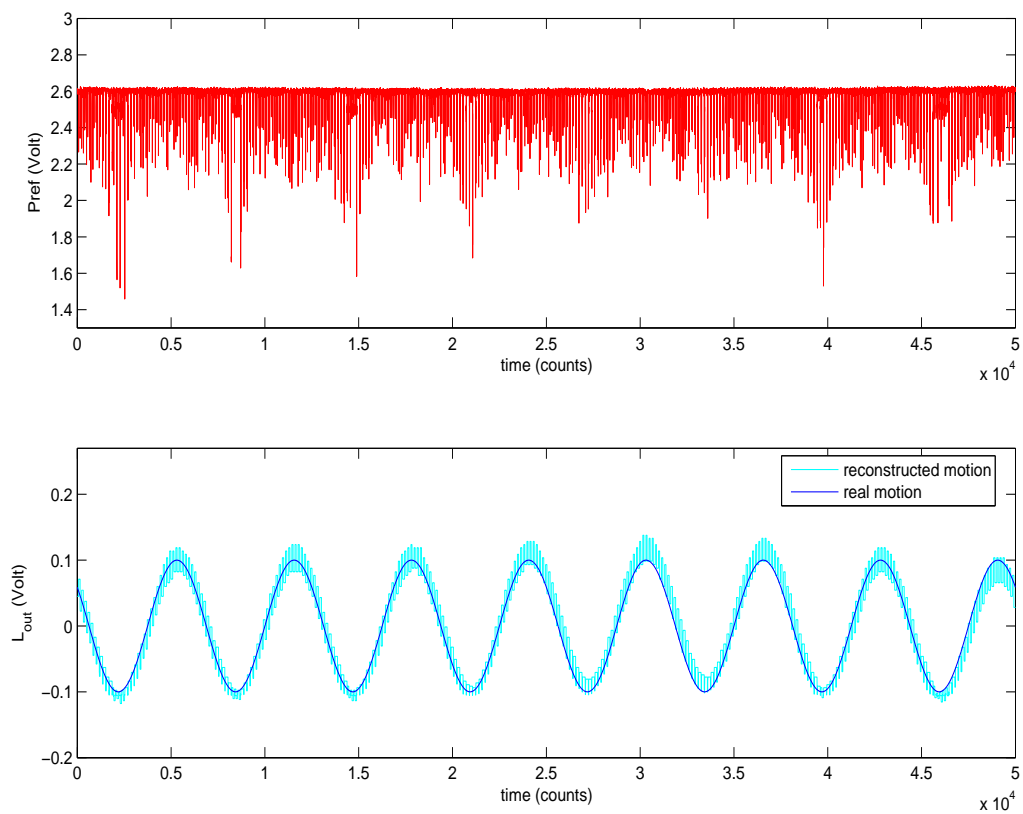


Figure 4.16: Reconstruction of a sinusoidal motion compared to the real one. The upper picture shows the reflected cavity power, while the lower picture shows the reconstructed motion (cyan) superimposed with the real one (blue).

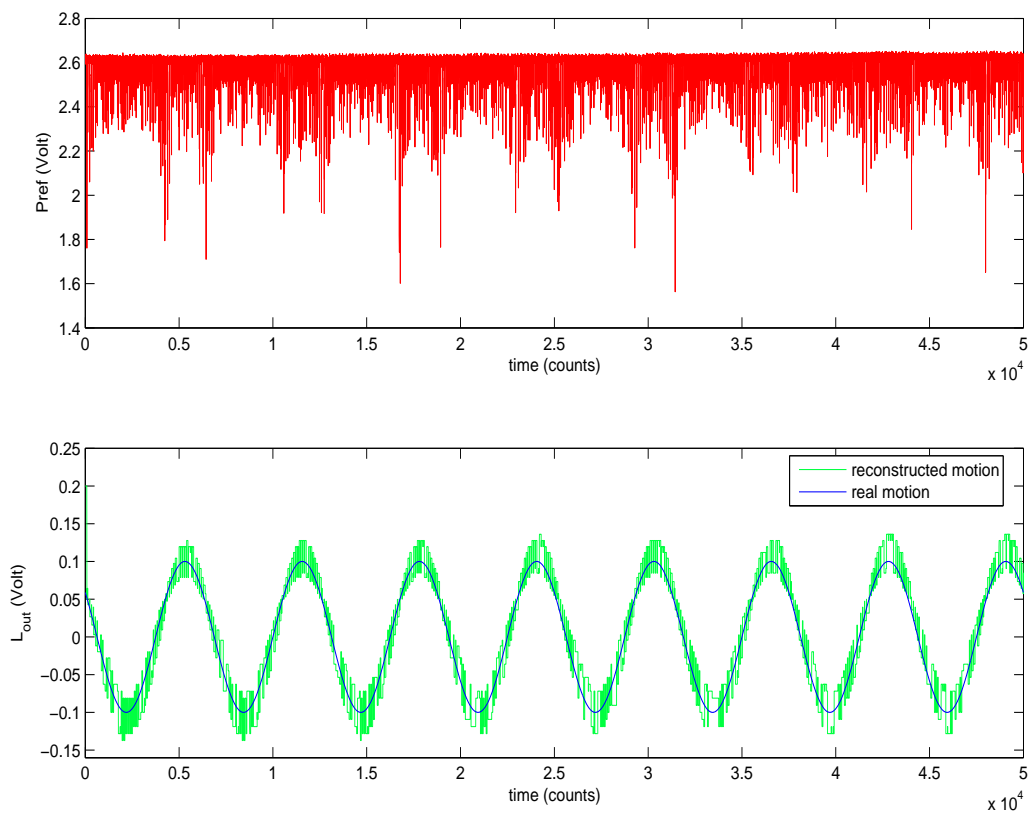


Figure 4.17: A second reconstruction of a sinusoidal motion compared to the real one. The upper picture shows the reflected cavity power, while the lower picture shows the reconstructed motion (green) superimposed with the real one (blue).

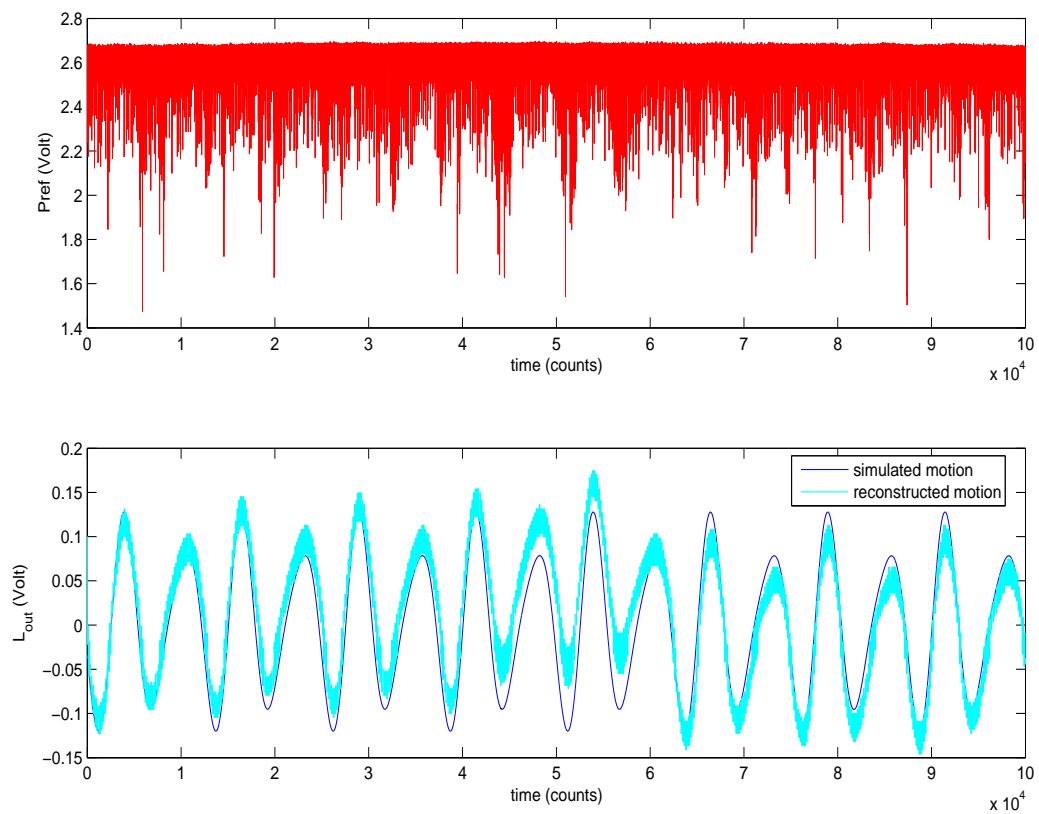


Figure 4.18: Reconstruction of a double sinusoidal motion compared to the real one. The upper picture shows the reflected cavity power, while the lower picture shows the reconstructed motion (cyan) superimposed with the real one (blue).

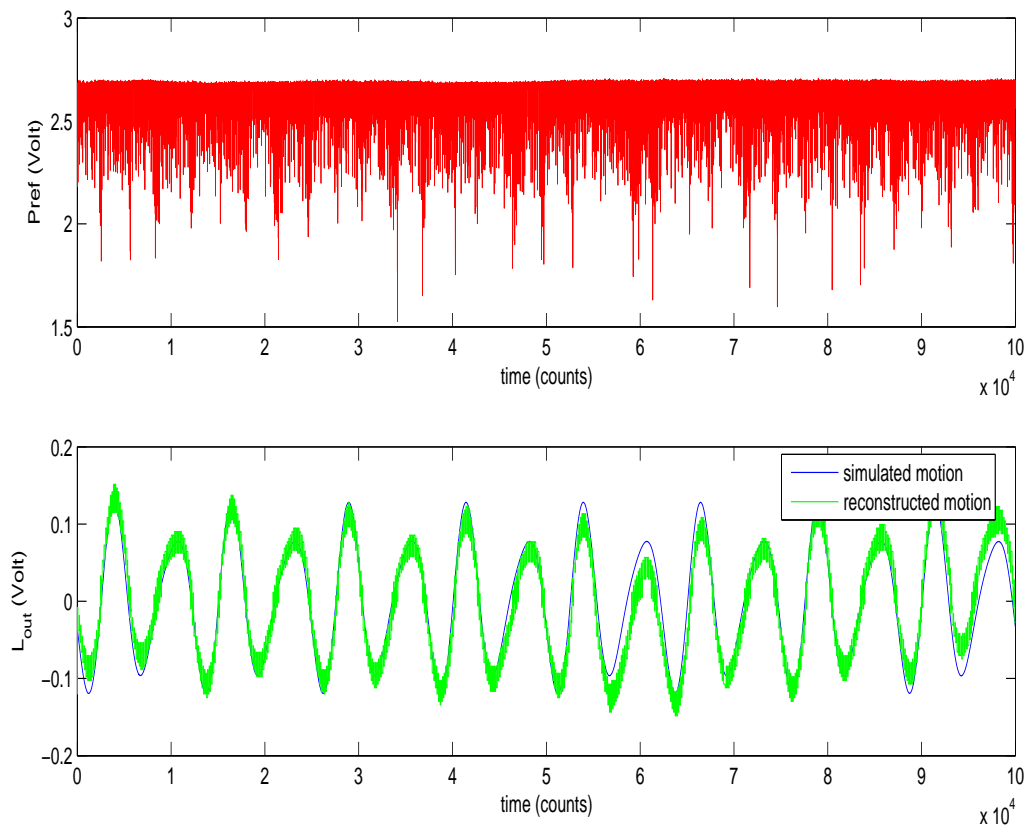


Figure 4.19: A second example of the reconstruction of a double sinusoidal motion compared to the real one.

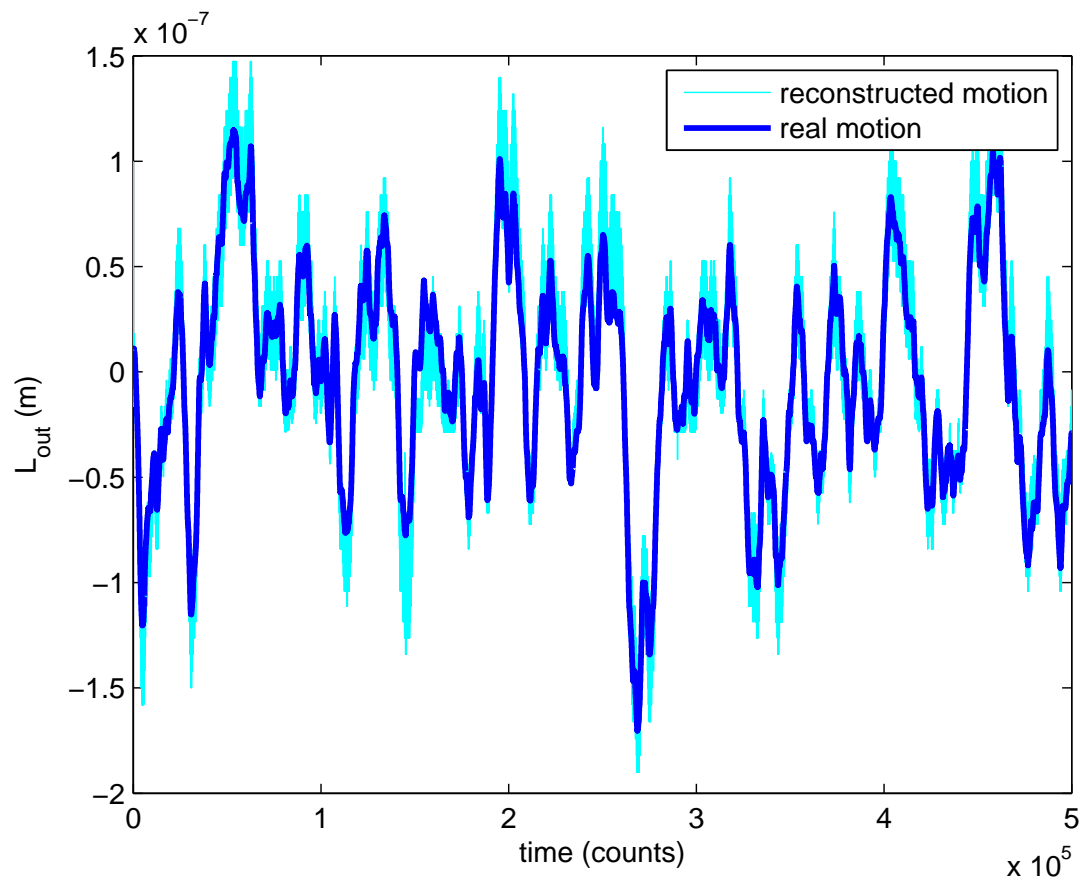


Figure 4.20: Reconstruction of a low frequency longitudinal random motion (cyan) compared to the real one (blue).

In fig. 4.20 we find the experimental results. Fig. 4.21 shows the spectrum of the real noise signal compared to the one of the simple reconstructed signal: as we can see, the reconstructed signal contains a frequency component at 50 Hz and its harmonics, that derive from the modulation imposed to the piezo to apply the fringe counting algorithm. In order to attenuate this frequency, we filtered the signal through a first order Butterworth filter: the results are shown in fig. 4.22.

Fig. 4.23 shows a second example of reconstruction of a longitudinal random motion, while fig. 4.24 shows the comparison between the random motion and the filtered reconstructed signal.

4.4 Fabry Perot with a suspended mirror: experimental data and critical analysis

Once we have tested the reconstruction algorithm on the Fabry Perot with fixed mirrors, we suspended the output cavity mirror to the last stage of a double pendulum (fig. 3.13), in order to isolate it from the ground

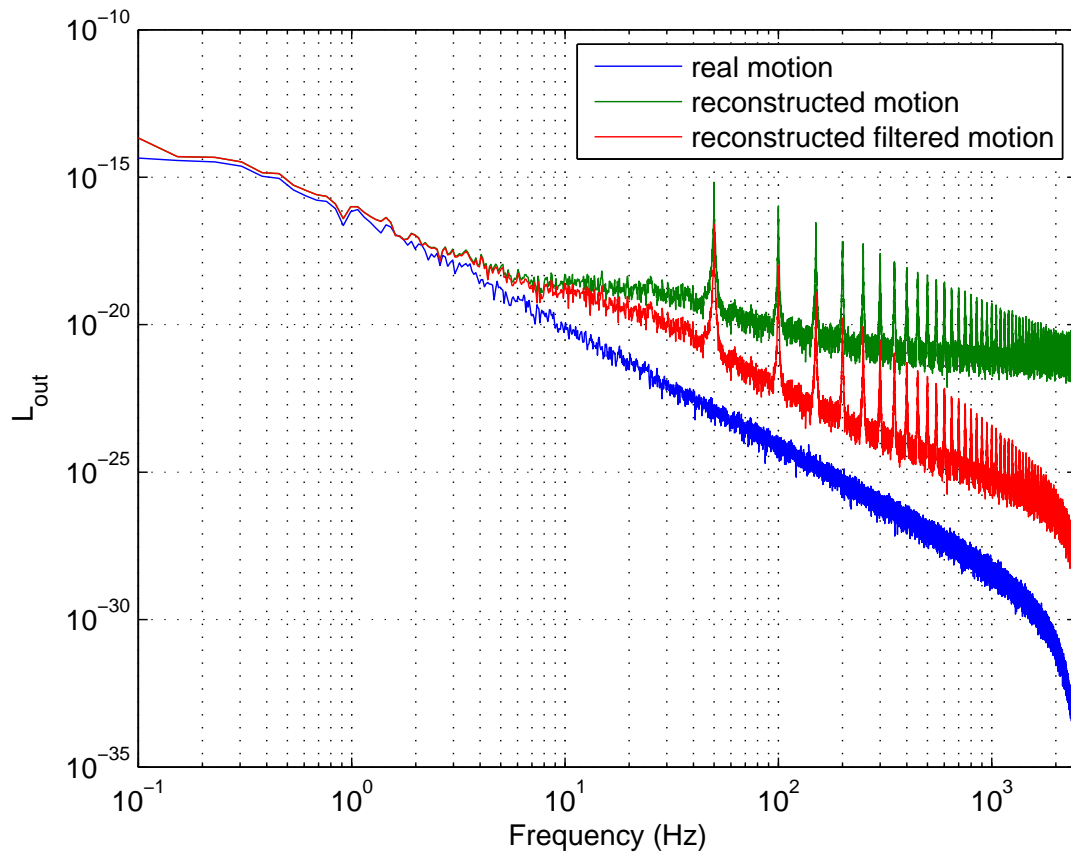


Figure 4.21: A spectrum of the real noise signal (blue) compared to the reconstructed one (green) and with the filtered reconstructed signal (red).

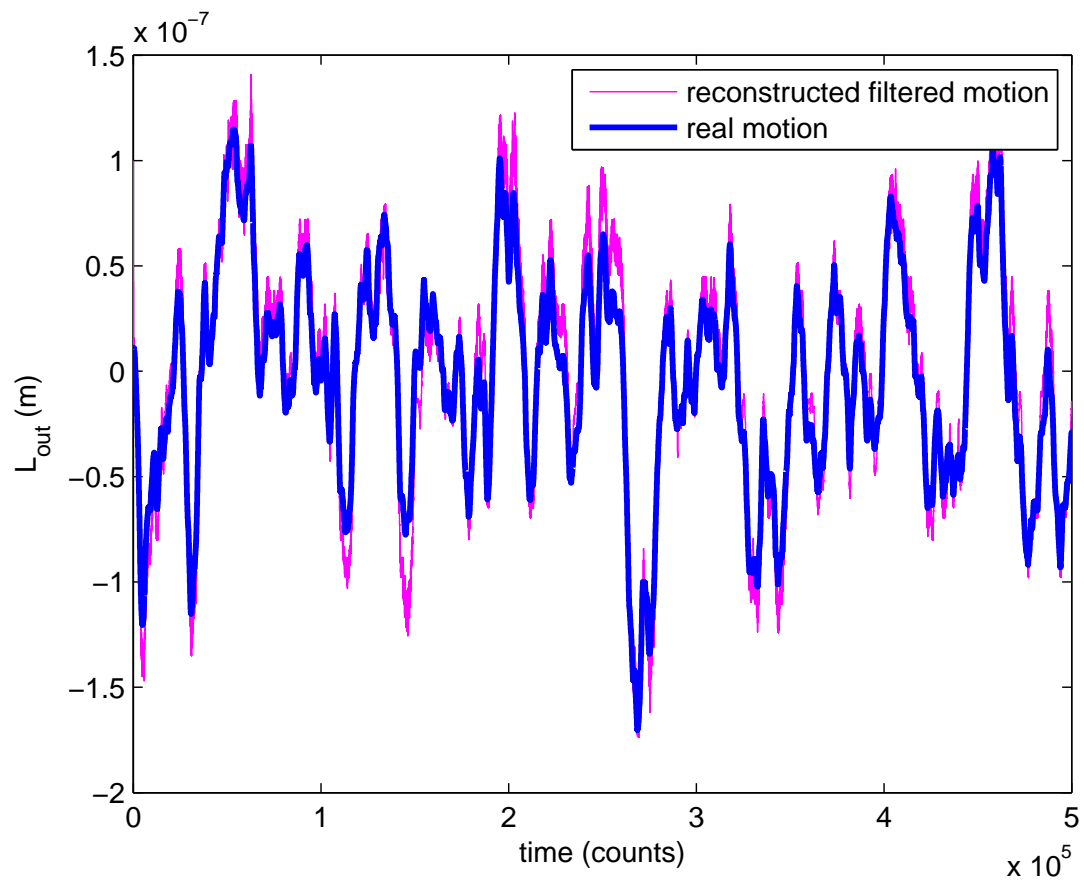


Figure 4.22: Comparison between the real random motion (blue) and the filtered reconstructed signal (pink).

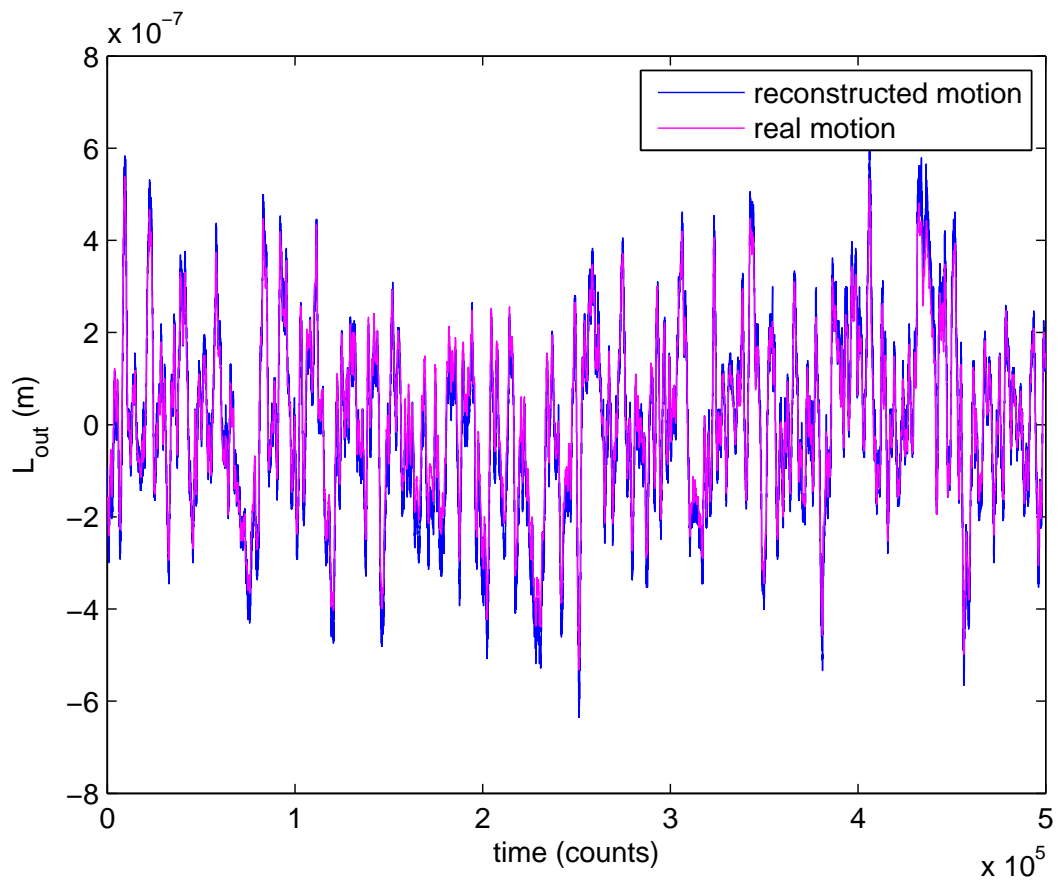


Figure 4.23: Another example of reconstruction of a random motion.

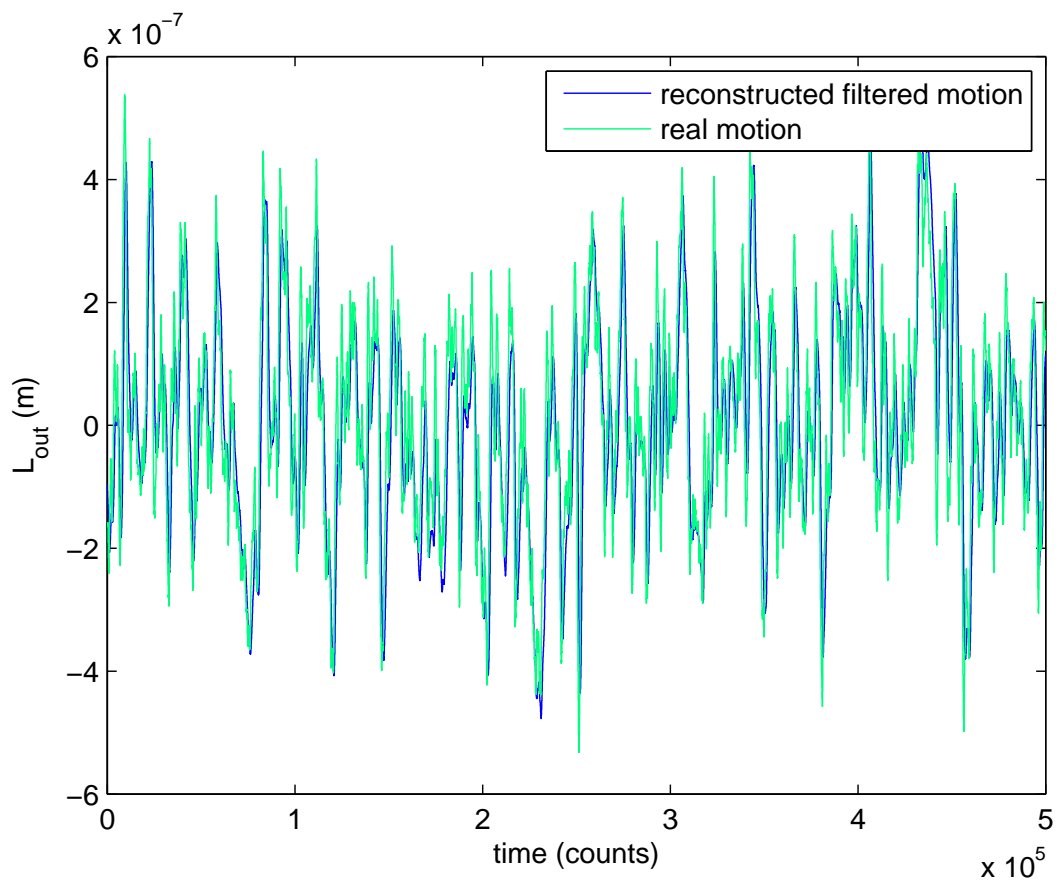


Figure 4.24: Comparison between the real random motion (green) and the filtered reconstructed signal (blue).

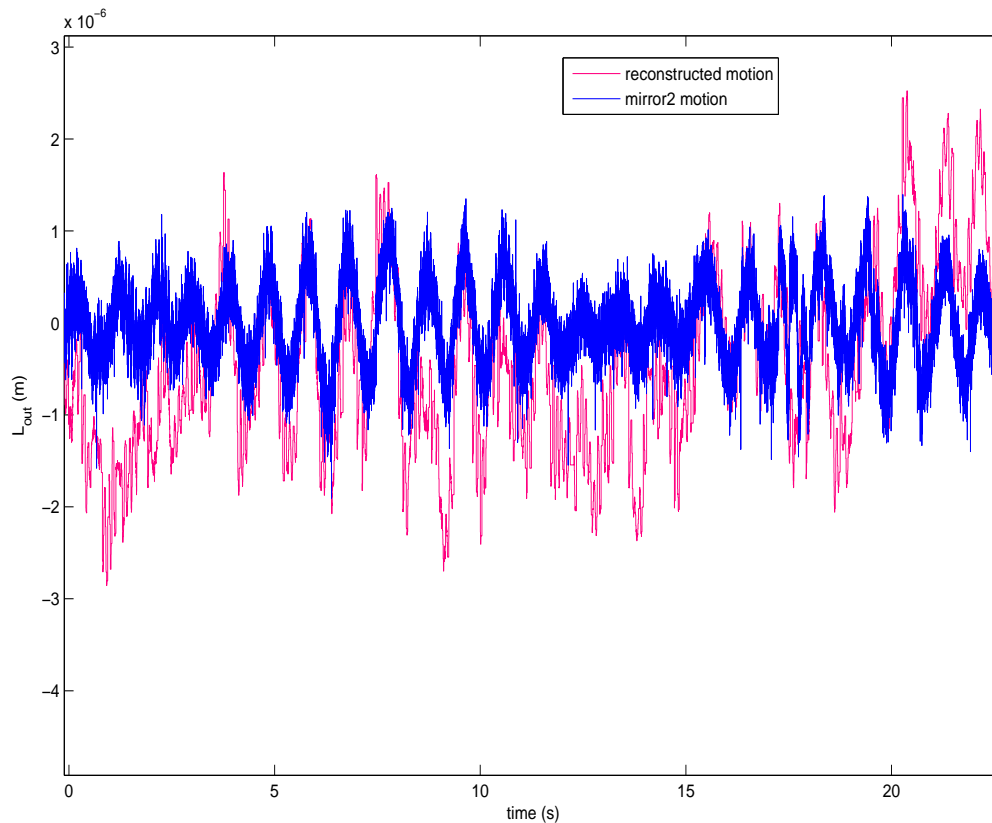


Figure 4.25: Reconstruction of the relative mirror motion (pink) compared to the motion of the output cavity mirror (blue).

motion in the frequency range following the mechanical resonances of the suspension system. The reading and actuation systems for the control of this suspension have been described in detail in chapter 3.

In this new configuration we performed various measurements to reconstruct the relative motion of the two mirrors using the reflected cavity power and the fringe counting algorithm.

Fig. 4.25 and 4.26 show two examples of reconstruction of the relative mirror motion compared to the motion of the suspended mirror. As we can see, the frequency of the reconstructed signal is in agreement with the suspended mirror motion. It is reasonable that the reconstructed signal is dominated by the suspended mirror motion, because the relative RMS is about $1 \mu\text{m}$, while it is much lower for the fixed mirror motion.

Fig. 4.27 shows the spectrum of the reconstructed signal, compared to the spectrum of the output mirror motion and to the spectrum of the Episensor signal. At low frequencies the reconstructed motion is in agreement with the Episensor signal, while at high frequencies we can see that the reconstructed signal does not contain the frequency components read by the Episensor: this behaviour is due to the fact that the reconstructed motion is dominated by the suspended mirror motion, that filters the frequencies following its

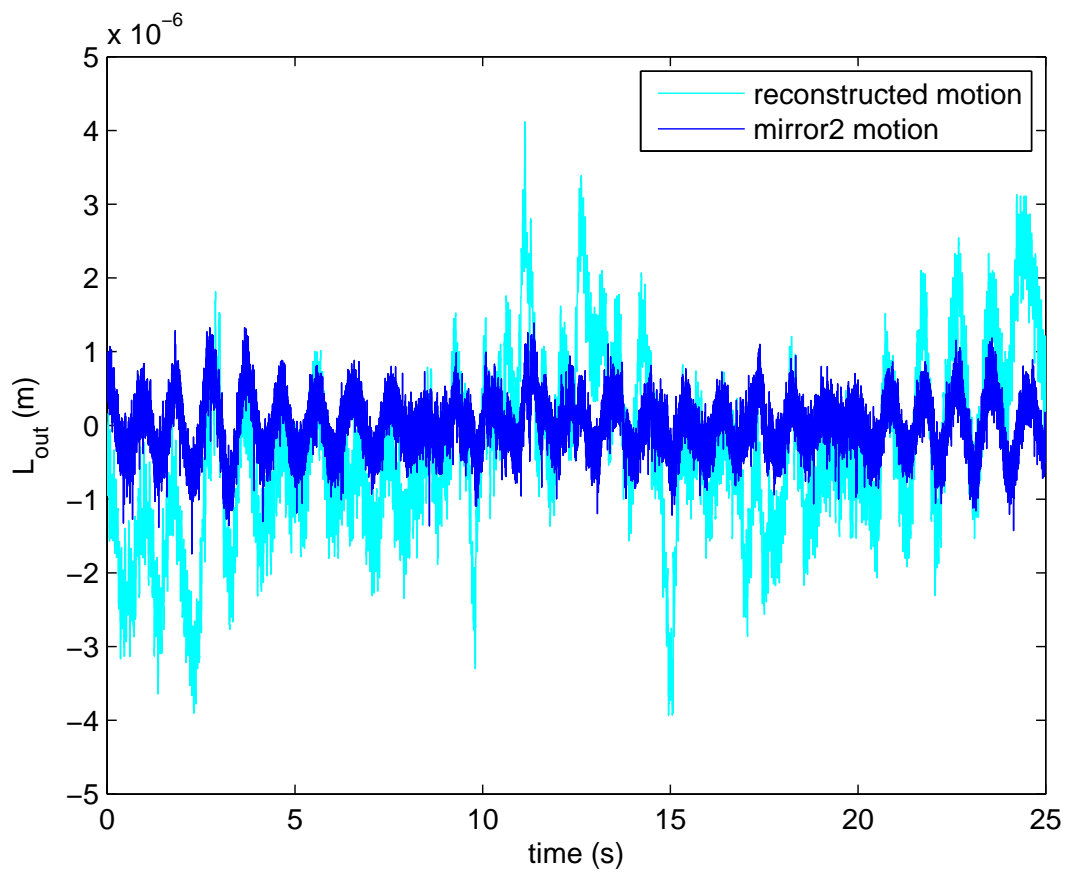


Figure 4.26: A second reconstruction of the relative mirror motion (cyan) compared to the motion of the output cavity mirror (blue).

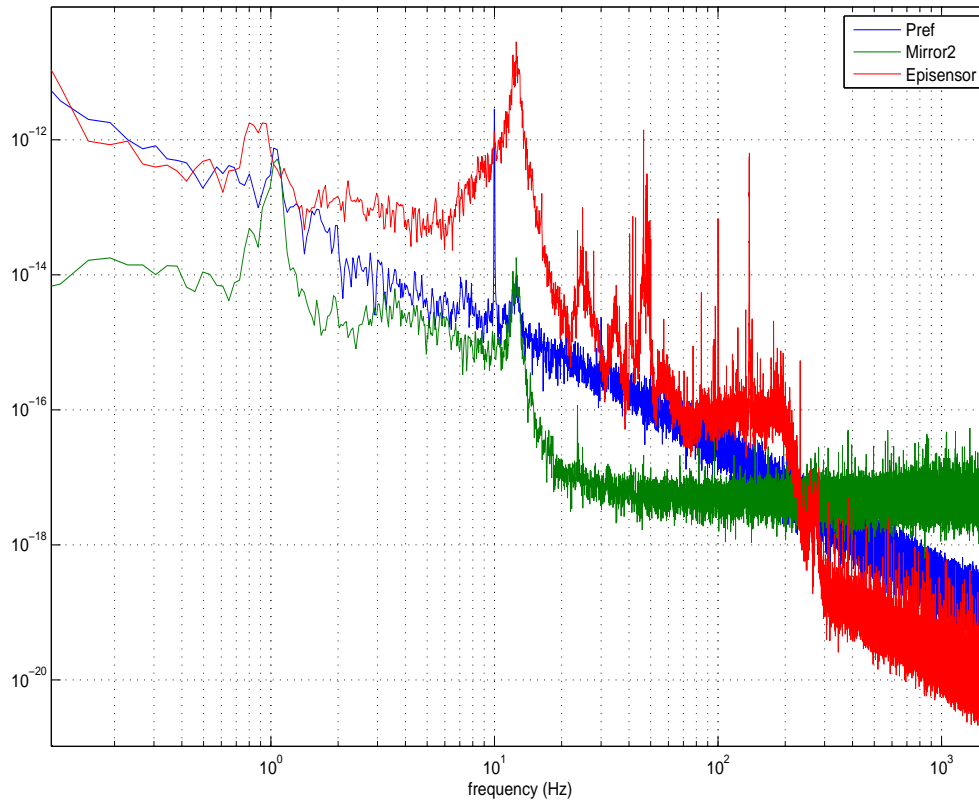


Figure 4.27: Spectrum of the reconstructed signal (blue) compared to the output mirror motion (green) and with the Episensor signal (red).

resonances.

4.4.1 Critical analysis

The set of measurements performed with the suspended cavity has pointed out the current limitations in the reconstruction of the relative mirror motion. These limitations are linked to:

- instantaneous variation of the modulation amplitude due to the residual motion of the suspended mirror
- narrow dynamical range of the piezoelectric actuator
- low sampling frequency in the digital acquisition system

The first limitation affects the reconstruction procedure and mainly the correct fringe counting.

Fig. 4.28 shows the modulation amplitude together with the reflected cavity power: as we can see there is an instantaneous variation in the number of the resonance peaks per modulation period, due to the angular

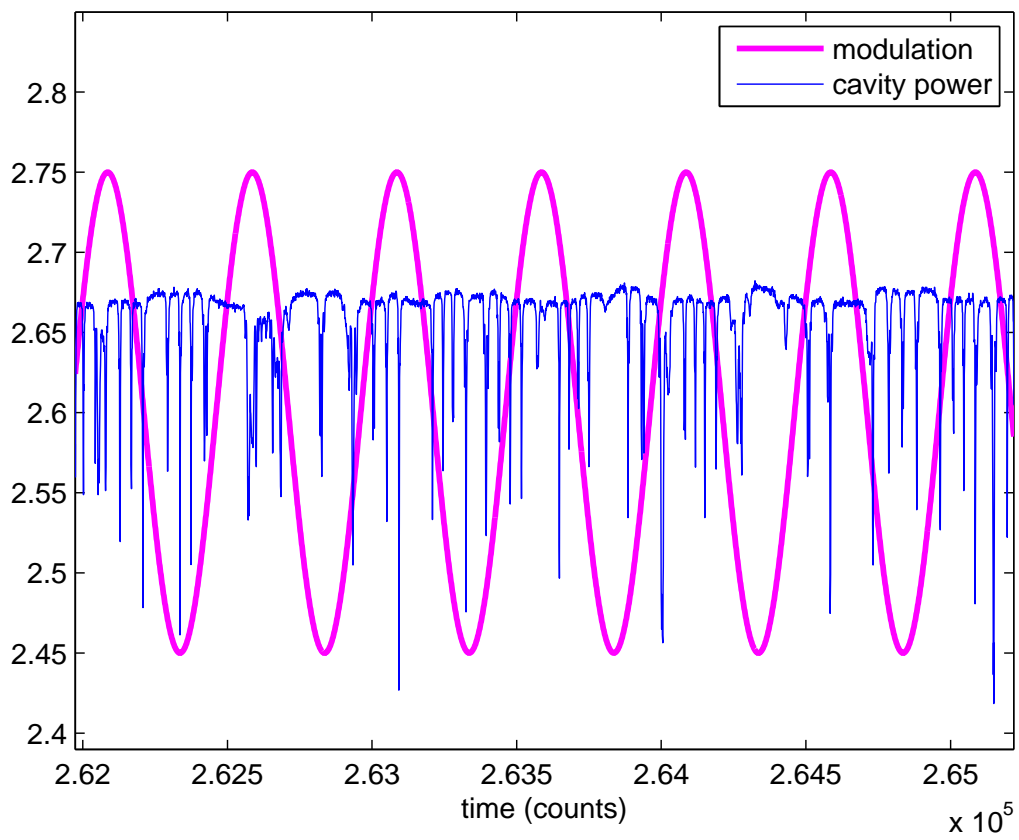


Figure 4.28: Superposition of the modulation amplitude with the corresponding reflected cavity power.

misalignments. As a consequence the fringe counting becomes more difficult, because the number of fringes per modulation period is no more constant.

Furthermore the dynamical range of the piezo actuator resulted too narrow for locking the cavity and acquire informations about the motion from the control signal.

At last, we know from eq. (4.11) that for the correct application of the fringe counting algorithm a minimum sampling frequency f_s in the digital acquisition system is required. The sampling frequency of 5000 KHz currently used in our digital acquisition system is sometimes low for our purposes.

All the above considerations lead to the conclusion that there is no theoretical limitation about the use of the device developed in this work as a sensitive seismometer, but variuos improvements are required in the experimental set-up.

These improvements involve the control of the angular degrees of freedom of the last stage of the double pendulum suspension, the use of a piezoelectric actuator with a wider dymanical range, the use of a higher sampling frequency in the digital acquisition system.

Chapter 5

Mechanical simulations and sensitivity curve of a 3mx3m Michelson interferometer

In the previous chapter we described the performance and limitations of the seismic sensor based on a Fabry-Perot cavity, developed in this work.

This chapter contains several simulations about the overall performance of a 3mx3m Michelson interferometer, currently under development in Virgo Lab in Napoli. This device has been designed to obtain sensitive measurements of secular strain, tides waves and for studying the free oscillations of the earth.

The main feature of our interferometer is the ULF (Ultra Low Frequency) system of suspension, which has been designed to isolate the optics from environmental noises. In order to attenuate seismic motion in this kind of interferometers, various mechanical filters are used: filters are realized by pendulum in the horizontal direction and by springs in the vertical direction [34] [35] .

The main parts of the ULF suspension system are: a horizontal pre-isolation stage with ultra-low resonance frequency (inverted pendulum), a pendulum stage and a suspension subsystem for the mirror (fig. 5.1).

The first part of the chapter is devoted to the lagrangian model and to the mechanical simulations of the suspension system, including several transfer functions, while the second part is devoted to the analysis of the sensitivity curve of the interferometer, with a list of the main expected noise contributions, among which seismic noise.

List of Constants

Here is a list of the parameters employed to derive the lagrangian model of the suspension system and the individual noise contributions to the sensitivity curve of the interferometer.

Physical Constantres

Gravitational acceleration	$g = 9.806 \text{ m} \cdot \text{s}^{-2}$
Temperature	$T = 300 \text{ K}$
Boltzmann constant	$K_B = 1.38 \times 10^{-23} \text{ J} \cdot \text{K}^{-1}$
Planck constant	$h_p = 6.26 \times 10^{-34} \text{ J} \cdot \text{s}$
Light speed	$c = 3 \times 10^8 \text{ m} \cdot \text{s}^{-1}$
Universal gravitational constant	$G = 6.67 \times 10^{-11} \text{ m}^3 \cdot \text{Kg}^{-1} \cdot \text{s}^{-2}$
Earth radius	$R_E = 6370 \times 10^3 \text{ m}$
Earth density	$\rho_E = 2 \times 10^3 \text{ Kg} \cdot \text{m}^{-3}$

Material Constants

Marval 18 maraging steel (upper wires and blades)

Density	$\rho_{\text{wu}} = 7.9 \times 10^3 \text{ Kg} \cdot \text{m}^{-3}$
Young modulus	$E_u = 1.86 \times 10^{11} \text{ N} \cdot \text{m}^{-2}$
Yield strength	$\sigma_b = 2 \times 10^9 \text{ N} \cdot \text{m}^{-2}$
Shear strength	$s_u = 7.3 \times 10^{10} \text{ N} \cdot \text{m}^{-2}$
Thermal expansion coefficient	$\alpha_{\text{stu}} = 16 \times 10^{-6} \text{ K}^{-1}$
Specific heat	$c_{\text{su}} = 468 \text{ J} \cdot \text{kg}^{-1} \cdot \text{K}^{-1}$
Thermal conductivity	$k_{\text{stu}} = 20 \text{ J} \cdot \text{m}^{-1} \cdot \text{K}^{-1} \cdot \text{s}^{-1}$
Marval 18 loss angle	$\phi_{\text{wu}} = 1 \times 10^{-4}$

Tungsten (lower wires)

Density	$\rho_{\text{wd}} = 1.93 \times 10^4 \text{ kg} \cdot \text{m}^{-3}$
Young modulus	$E_d = 4 \times 10^{11} \text{ N} \cdot \text{m}^{-2}$
Shear strength	$s_d = 17.5 \times 10^{10} \text{ N} \cdot \text{m}^{-2}$
Thermal expansion coefficient	$\alpha_{\text{std}} = 4.5 \times 10^{-6} \text{ K}^{-1}$
Specific heat	$c_{\text{sd}} = 138 \text{ J} \cdot \text{kg}^{-1} \cdot \text{K}^{-1}$
Specific heat/volume	$c_{\text{std}} = c_{\text{sd}} \rho_{\text{wd}}$
Thermal conductivity	$k_{\text{std}} = 164.4 \text{ J} \cdot \text{m}^{-1} \cdot \text{K}^{-1} \cdot \text{s}^{-1}$
Marval 18 loss angle	$\phi_{\text{wd}} = 1 \times 10^{-5}$

AISI 304 (suspensions)

Density	$\rho_s = 8030 \text{ kg} \cdot \text{m}^{-3}$
Young modulus	$E_s = 1.93 \times 10^{11} \text{ N} \cdot \text{m}^{-2}$
Thermal expansion coefficient	$\alpha_{\text{std}} = 17.8 \times 10^{-6} \text{ K}^{-1}$
Specific heat	$c_{\text{ss}} = 503 \text{ J} \cdot \text{kg}^{-1} \cdot \text{K}^{-1}$
Thermal conductivity	$k_{\text{sts}} = 16.27 \text{ J} \cdot \text{m}^{-1} \cdot \text{K}^{-1} \cdot \text{s}^{-1}$

Fused silica (mirrors)

Density	$\rho_m = 2202 \text{ kg} \cdot \text{m}^{-3}$
Young modulus	$E_m = 7.36 \times 10^{10} \text{ N} \cdot \text{m}^{-2}$
Poisson ratio	$\sigma_m = 0.17$
Thermal expansion coefficient	$\alpha_m = 0.54 \times 10^{-6} \text{ K}^{-1}$
Specific heat	$c_m = 682 \text{ J} \cdot \text{kg}^{-1} \cdot \text{K}^{-1}$
Thermal conductivity	$k_m = 2.1 \text{ J} \cdot \text{m}^{-1} \cdot \text{K}^{-1} \cdot \text{s}^{-1}$
Suprasil loss angle	$\phi_m = 1 \times 10^{-7}$

Geometrical Parameters***Inverted pendulum parameters***

Payload mass	$M_p = 70 \text{ Kg}$
IP leg mass	$m_l = 11.64 \text{ Kg}$
IP leg length	$L_1 = 1.455 \text{ m}$
Bell mass	$m_b = 8.71 \text{ Kg}$
Bell length	$L_b = 0.35 \text{ Kg}$
counter weight mass	$m_{\text{cw}} = 15 \text{ Kg}$
rotational spring constant of the flex joint	$k_\theta = 700 \text{ N} \cdot \text{m} \cdot \text{rad}^{-1}$

Filters parameters

Wire1 length (filter0-filter1)	$L_{w1} = 0.65 \text{ m}$
Wire1 diameter	$d_{w1} = 0.002 \text{ m}$
Wire1 mass	$M_{w1} = 0.016 \text{ Kg}$
Wire2 length (filter1-last stage)	$L_{w2} = 0.3 \text{ m}$
Wire2 diameter	$d_{w2} = 0.001 \text{ m}$
Wire2 mass	$M_{w2} = 0.002 \text{ Kg}$
Filter0 mass	$M_{f0} = 48 \text{ Kg}$
Filter1 mass	$M_{f1} = 18 \text{ Kg}$

Mirror suspension subsystem parameters

Suspension platform mass	$M_{\text{sp}} = 19.72 \text{ Kg}$
Intermediate mass and magnet box mass	$M_i = 3.2 \text{ Kg}$
Mirror mass	$M_m = 1.067 \text{ Kg}$
Mass of the recoil mass	$M_r = 0.98 \text{ Kg}$
Intermediate stage wires length	$L_{w3} = 0.25 \text{ m}$
Mirror wire length	$L_{wm} = 0.2 \text{ m}$
Lower wire diameter	$d_{w3} = 100 \times 10^{-6} \text{ m}$
Mirror wire diameter	$d_{wm} = 50 \times 10^{-6} \text{ m}$
Recoil mass wire diameter	$d_{rm} = 100 \times 10^{-6} \text{ m}$
Damping coefficient	$\gamma_0 = 0.1$

Mirror parameters

Mirror radius of curvature	$R_m = 4 \text{ m}$
Mirror radius	$R_{\text{mir}} = 0.05 \text{ m}$
Mirror thickness	$h_m = 0.06 \text{ m}$

Laser and Interferometer Parameters

Interferometer arm length	$L_{\text{arm}} = 3 \text{ m}$
Laser power	$P_{\text{las}} = 2 \text{ W}$
Photodiode efficiency	$\eta = 0.7$
Laser wavelength	$\lambda = 1064 \times 10^{-9} \text{ m}$
Horizontal to vertical coupling angle	$\theta_0 = \frac{L_{\text{arm}}}{2R_E}$

5.1 Inverted pendulum**Role in seismic isolation**

We start analyzing the first important part of the suspension system: the inverted pendulum. An inverted pendulum is a horizontal pre-isolation stage with ultra low resonant frequency (below 100 mHz). The most important features of the inverted pendulum are:

- It provides attenuation at frequencies of microseismic peak (100 mHz to 300 mHz)
- It provides a mean to position the entire suspension system without requiring large force
- It provides a quasi-inertial stage to actively damp the motion of the suspended chain

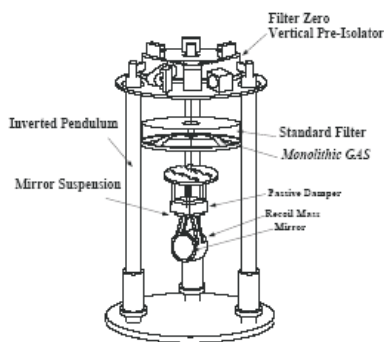


Figure 5.1: A view of the entire suspension system.

l	length of the IP leg
m	mass of the IP leg
I	momentum of inertia about the center of mass of the IP leg
M	mass of the payload
k_θ	rotational spring constant of the flex joint
(x, z)	position of the payload
(x_l, z_l)	position of the center of mass of the IP leg
(x_0, z_0)	position of the flex joint attachment to the ground
θ	angle of the IP leg with respect to the vertical axis

Table 5.1: Parameters for the simple inverted pendulum model.

5.1.1 Lagrangian model of the inverted pendulum

A schematic model of the IP is illustrated in fig. 5.2. The IP consists of a flex joint fixed to the ground, a rigid cylindrical leg connected into it and the payload on the top of the leg [36].

The payload, which is modeled as a point mass, is the object being isolated from the ground motion. The IP leg is represented as a completely rigid body and its internal resonances are omitted in the following model.

The lagrangian of the system as a function of the parameters shown in table 5.1 is expressed as:

$$L = K - U, \quad (5.1)$$

where

$$K = \frac{1}{2}M(\dot{x}^2 + \dot{z}^2) + \frac{1}{2}m(\dot{x}_l^2 + \dot{z}_l^2) + \frac{1}{2}I\dot{\theta}^2 \quad (5.2)$$

represents the kinetic energy contribute and

$$U = Mgz + mgz_l + \frac{1}{2}k_\theta\theta^2 \quad (5.3)$$

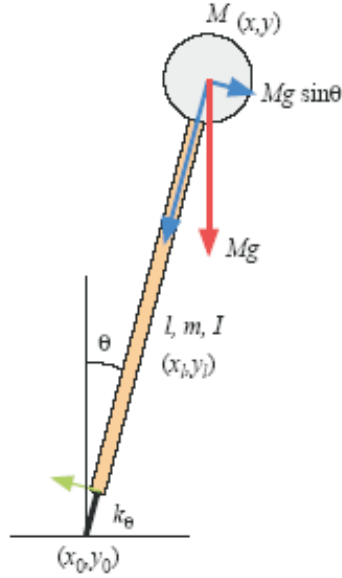


Figure 5.2: A schematic view of the IP, in the simple model.

the potential energy contribute, with the geometrical constraints:

$$\begin{aligned}
 x_l &= \frac{1}{2}(x + x_0) \\
 z_l &= \frac{z}{2} \\
 x &= l \sin \theta + x_0 \\
 z &= l \cos \theta.
 \end{aligned} \tag{5.4}$$

Under these conditions the kinetic and potential contribute in the Lagrangian are simplified by omitting the vertical component of the velocity:

$$K = \frac{1}{2}M\dot{x}^2 + \frac{1}{8}m(\dot{x} + \dot{x}_0)^2 + \frac{1}{2}I\left(\frac{\dot{x} - \dot{x}_0}{l}\right)^2, \tag{5.5}$$

$$U = Mgl \cos\left(\frac{x - x_0}{l}\right) + \frac{mgl}{2} \cos\left(\frac{x - x_0}{l}\right) + \frac{1}{2}k_\theta\left(\frac{x - x_0}{l}\right)^2 \tag{5.6}$$

The Euler-Lagrange equation of the motion is derived from:

$$\frac{d}{dt} \frac{\partial K}{\partial \dot{x}} = \frac{\partial U}{\partial x}. \tag{5.7}$$

We obtain:

$$\left(M + \frac{m}{4} + \frac{I}{l^2}\right)\ddot{x} + \left(\frac{m}{4} - \frac{I}{l^2}\right)\ddot{x}_0 = -\left\{\frac{k_\theta}{l} - \left(\frac{m}{2} + M\right)g\right\} \frac{x - x_0}{l}. \tag{5.8}$$

At the first order the previous equation has the form of the equation of motion of a harmonic oscillator, with an effective spring constant:

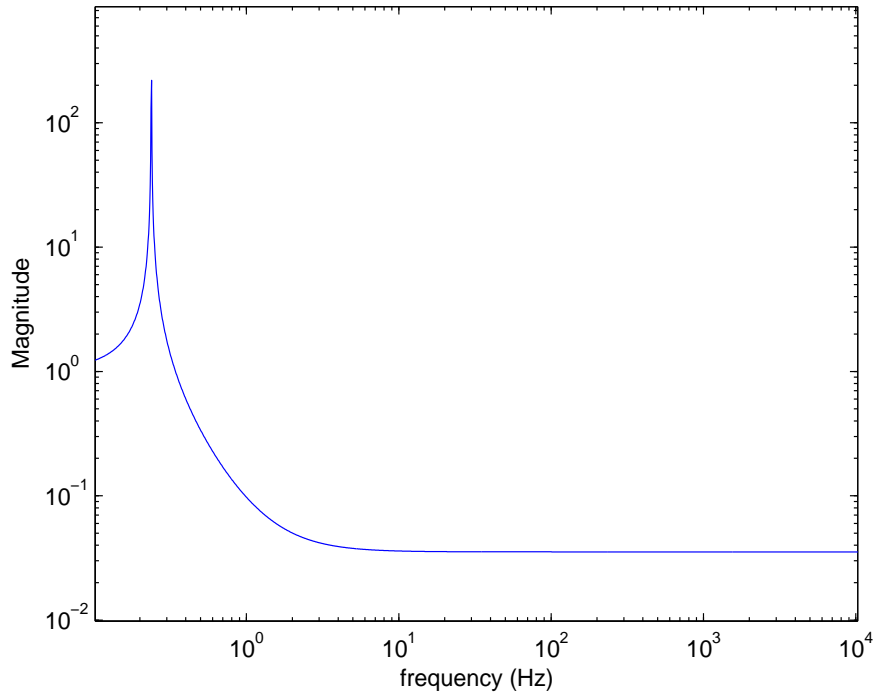


Figure 5.3: Inverted pendulum transfer function.

$$k_{\text{eff}} = \frac{k_{\theta}}{l^2} - \left(\frac{m}{2} + M\right)\frac{g}{l}. \quad (5.9)$$

The first term in k_{eff} corresponds to the elastic restoring force of the flex joint, while the rest represents a repulsive force, the so called *gravitational anti-spring force*. With the gravitational anti-spring effect the cumulative spring constant is effectively reduced. The effect of the anti-spring is proportional to the mass of the leg and the payload and can be tuned by changing the payload. The resonance frequency of the IP is given by:

$$f_0 = \frac{1}{2\pi} \sqrt{\frac{k_{\text{eff}}}{\frac{I}{l^2} + \frac{m}{4} + M}}. \quad (5.10)$$

By solving equation (5.8) in the Fourier domain we obtain the motion transfer function between the ground and the payload:

$$H_{\text{IP}}(\omega) = \frac{k_{\text{eff}} + \left(\frac{m}{4} - \frac{I}{l^2}\right)\omega^2}{k_{\text{eff}} - \left(M + \frac{m}{4} + \frac{I}{l^2}\right)\omega^2}. \quad (5.11)$$

The Bode plot of the transfer function of the simple IP is shown in fig. 5.3. This transfer function behaves similarly to the one of a harmonic oscillator up to the resonance frequency: while the standard oscillator shows infinite capability of attenuation, the IP transfer function saturates at a certain level of attenuation. In order to change this level of saturation we have to balance the mass distribution of the leg and its center of rotation: we can put a counter-weight (fig. 5.4) at the bottom of the IP leg.

l_1	length of the IP leg
m_1	mass of the IP leg
I_1	momentum of inertia about the center of mass of the IP leg
M	mass of the payload
l_2	length of the bell
m_2	mass of the bell
I_2	momentum of inertia about the center of mass of the bell
M_3	mass of the CW
k_θ	rotational spring constant of the flex joint
(x, z)	position of the payload
(x_l, z_l)	position of the center of mass of the IP leg
(x_0, z_0)	position of the flex joint attached to the ground
θ	angle of the IP leg respect to the vertical axis

Table 5.2: Parameters for the inverted pendulum model with the counter weight.

In table 5.2 we find the new parameters used in the model with the counter weight. The new transfer function of the IP is:

$$H_{IPcw}(\omega) = \frac{A + B\omega^2}{A - C\omega^2}, \quad (5.12)$$

where A, B, C depend on the geometrical parameters of the pendulum:

$$A = \frac{k_\theta}{L_1^2} - \frac{g}{L_1} \left(M_p + \frac{m_1}{2} - \frac{m_b L_b}{2L_1} - \frac{m_{cw} L_b}{L_1} \right), \quad (5.13)$$

$$B = -\frac{I_{IP} + I_b}{L_1^2} + \frac{m_1}{4} - \frac{L_b m_b (2L_1 + L_b)}{4L_1^2} - \frac{L_b m_{cw} (L_1 + L_b)}{L_1^2}, \quad (5.14)$$

$$C = M_p + \frac{m_1}{4} + \frac{m_b L_b^2}{4L_1^2} + \frac{m_{cw} L_b^2}{L_1^2} + \frac{I_{IP} + I_b}{L_1^2}. \quad (5.15)$$

The plateau level in the transfer function is determined by B and C , while the parameters related to the bell and the CW can be used to tune the maximum attenuation at high frequencies.

5.2 Pendular mirror suspension subsystem

We analyze now the other fundamental parts of the suspension system: the first pendulum stage and the mirror suspension subsystem, which can be modeled as a triple pendulum.

In this section we will introduce a detailed lagrangian model of the entire suspension system in order to obtain the single resonance frequencies of the various stages and to take into account the internal dynamics of the suspension wires.

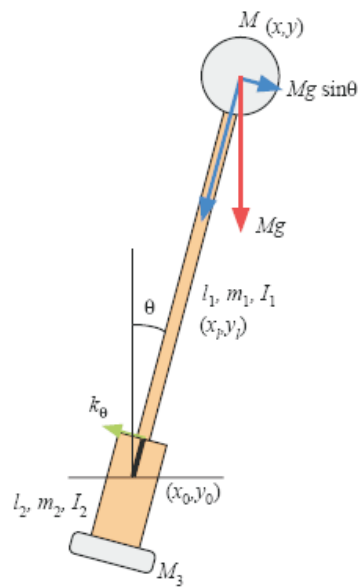


Figure 5.4: A schematic view of the IP with the counter weight mounted at the bottom of the leg.

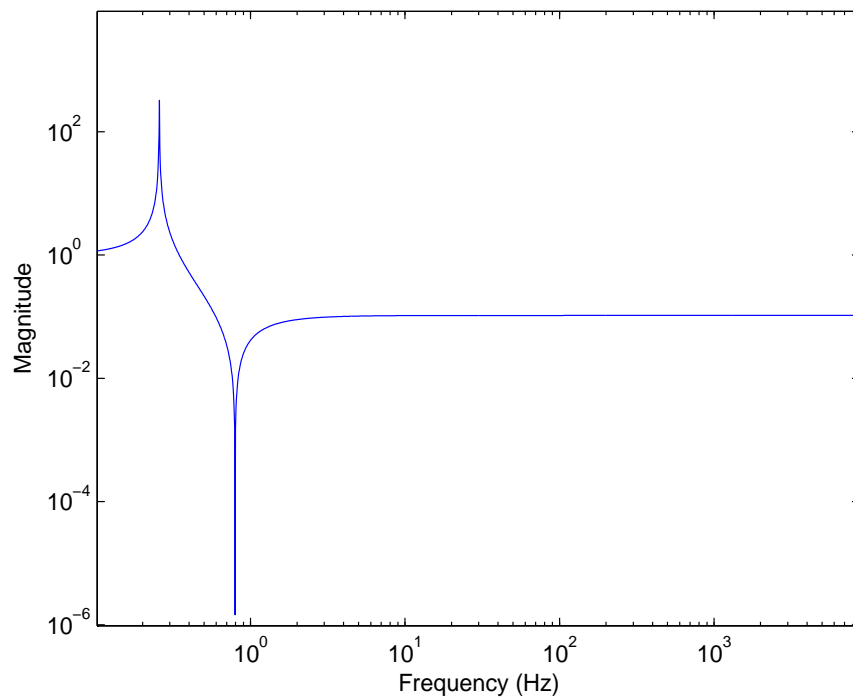


Figure 5.5: Inverted pendulum transfer function (model with the counter weight).

5.2.1 Lagrangian model

An attenuation system is characterized by the alternance of relatively rigid elements (masses, filter bodies,..) and comparatively elastic elements (suspension wires, blades..). This means that rigid parts can be considered

elementary, that is described only in terms of their rigid translations and rotations. These elements are connected by the elastic ones, whose internal mechanical stresses give rise to the recalling forces which make the system behave as a multiple oscillator.

In the following we will write the full lagrangian for our suspension system, masses and wires, in the approximation of no cross coupling between the vertical and horizontal motion, starting from the general treatment of a single wire under a certain tension T as a connector of two stages of a suspension system, that can be found in Appendix B.

5.2.2 Static Lagrangian

We consider now the Lagrangian for the transversal motion of our suspension system. As we can see in fig. 5.6 and fig. 5.7 our suspension system, except for the IP, is composed of:

- a filter (the first pendulum stage)
- a subsystem of suspension for the mirror, which can be modeled as a triple pendulum

We may treat the entire system as a pendulum composed of four stages. The first stage is the standard filter, the second stage is the suspension platform, the third stage is the intermediate mass and the last one is composed by the mirror and the recoil mass. The i_{th} stage has mass M_i and is connected to the $(i+1)_{th}$ stage by a wire of length L_{i+1} . The clamping point of the first stage has coordinates (x_0, y_0, z_0) . We choose the origin of z at the upper end of each wire separately.

The two upper masses are suspended baricentrically while the remaining masses are suspended through four wires. The tensions T_i on the various stages are given by:

$$\begin{aligned}
 T_1 &= g(M_1 + M_2 + M_3 + M_4), \\
 T_2 &= g(M_2 + M_3 + M_4), \\
 T_3 &= g(M_3 + M_4), \\
 T_4 &= gM_4.
 \end{aligned} \tag{5.16}$$

5.2.3 Total Lagrangian

The total Lagrangian [37] [38], including the violin modes (see Appendix B), for the transversal motion of the four masses connected by wires under tension, for both variables x and y is:

$$\mathcal{L} = K_{M1} + K_{W1} + U_{W1} + K_{M2} + K_{W2} + U_{W2} + K_{M3} + K_{W3} + U_{W3} + K_{M4} + K_{W4} + U_{W4}, \tag{5.17}$$

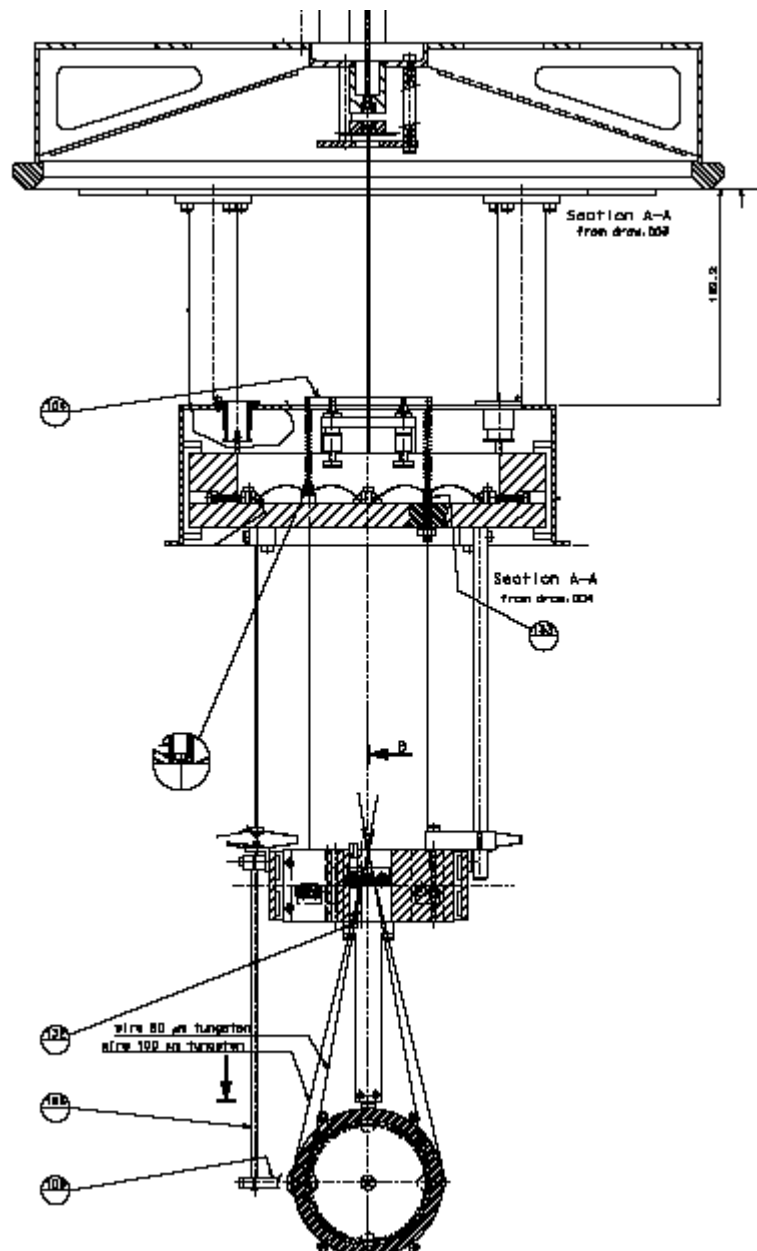


Figure 5.6: A detailed view of the payload: we note the filter, the suspension platform, the intermediate mass, the mirror.

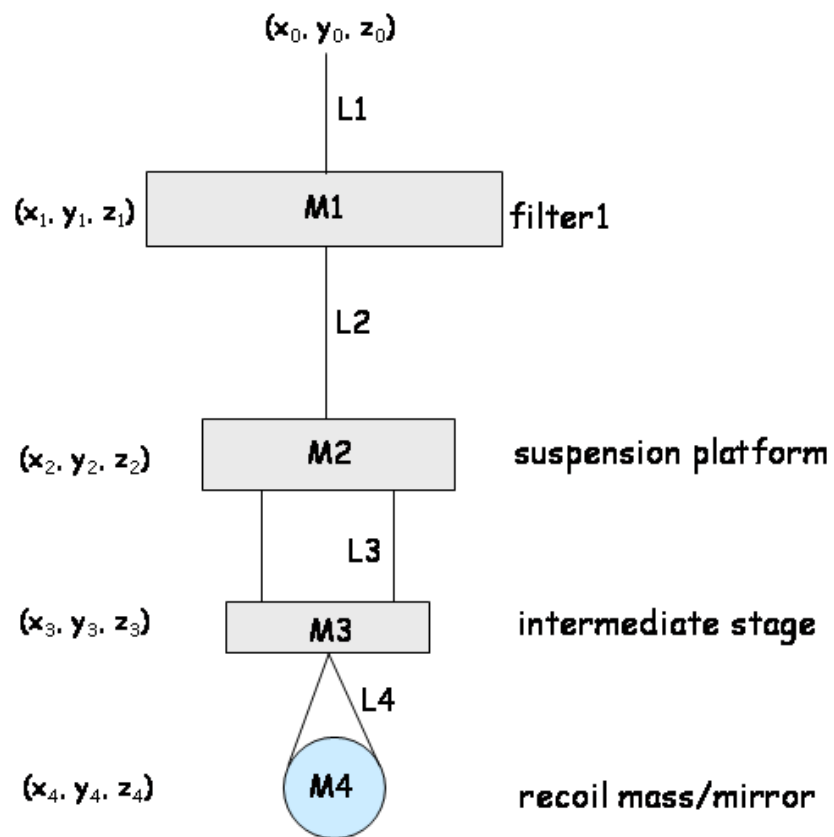


Figure 5.7: A schematic model for the payload.

where the kinetic contributions of the four masses are:

$$\begin{aligned}
K_{M1} &= \frac{M_1}{2} \left\{ [x_1(L_1)]^2 + [y_1(L_1)]^2 \right\} + \frac{J_{1x}}{2} [x_1'(L_1)]^2 + \frac{J_{1y}}{2} [y_1'(L_1)]^2 \\
K_{M2} &= \frac{M_2}{2} \left\{ [x_2(L_2)]^2 + [y_2(L_2)]^2 \right\} + \frac{J_{2x}}{2} [x_2'(L_2)]^2 + \frac{J_{2y}}{2} [y_2'(L_2)]^2 \\
K_{M3} &= \frac{M_3}{2} \left\{ [x_3(L_3)]^2 + [y_3(L_3)]^2 \right\} + \frac{J_{3x}}{2} [x_3'(L_3)]^2 + \frac{J_{3y}}{2} [y_3'(L_3)]^2 \\
K_{M4} &= \frac{M_4}{2} \left\{ [x_4(L_4)]^2 + [y_4(L_4)]^2 \right\} + \frac{J_{4x}}{2} [x_4'(L_4)]^2 + \frac{J_{4y}}{2} [y_4'(L_4)]^2, \tag{5.18}
\end{aligned}$$

the kinetic contributions of the wires are:

$$\begin{aligned}
K_{W1} &= \frac{1}{2} \int_0^{L_1} \rho_1 A_1 [x_1(z)]^2 dz + \frac{1}{2} \int_0^{L_1} \rho_1 A_1 [y_1(z)]^2 dz \\
K_{W2} &= \frac{1}{2} \int_0^{L_2} \rho_2 A_2 [x_2(z)]^2 dz + \frac{1}{2} \int_0^{L_2} \rho_2 A_2 [y_2(z)]^2 dz \\
K_{W3} &= \frac{1}{2} \int_0^{L_3} \rho_3 A_3 [x_3(z)]^2 dz + \frac{1}{2} \int_0^{L_3} \rho_3 A_3 [y_3(z)]^2 dz \\
K_{W4} &= \frac{1}{2} \int_0^{L_4} \rho_4 A_4 [x_4(z)]^2 dz + \frac{1}{2} \int_0^{L_4} \rho_4 A_4 [y_4(z)]^2 dz, \tag{5.19}
\end{aligned}$$

and the potential contributions of the wires are:

$$\begin{aligned}
U_{W1} &= \frac{1}{2} \int_0^{L_1} EI_1 [x_1''(z)]^2 + T_1 [x_1'(z)]^2 dz + \frac{1}{2} \int_0^{L_1} EI_1 [y_1''(z)]^2 + T_1 [y_1'(z)]^2 dz \\
U_{W2} &= \frac{1}{2} \int_0^{L_2} EI_2 [x_2''(z)]^2 + T_2 [x_2'(z)]^2 dz + \frac{1}{2} \int_0^{L_2} EI_2 [y_2''(z)]^2 + T_2 [y_2'(z)]^2 dz \\
U_{W3} &= \frac{1}{2} \int_0^{L_3} EI_3 [x_3''(z)]^2 + T_3 [x_3'(z)]^2 dz + \frac{1}{2} \int_0^{L_3} EI_3 [y_3''(z)]^2 + T_3 [y_3'(z)]^2 dz \\
U_{W4} &= \frac{1}{2} \int_0^{L_4} EI_4 [x_4''(z)]^2 + T_4 [x_4'(z)]^2 dz + \frac{1}{2} \int_0^{L_4} EI_4 [y_4''(z)]^2 + T_4 [y_4'(z)]^2 dz. \tag{5.20}
\end{aligned}$$

The explicit approximated expansions for $U_{W1}, U_{W2}, U_{W3}, U_{W4}$ can be found respectively in (B.27), (B.28), (B.29), (B.30).

Motion equations for the four stage pendulum

Once we have written the total transversal Lagrangian, we calculate the motion equations of the wires. We take into account only the y variable. The motion equations are obtained by varying $y(z)$ in the Lagrangian (5.17) and considering the variations $\delta y, \delta y'$ as independent.

We obtain the following set of equations and boundary conditions:

$$\begin{aligned}
EI_1 y_1''''(z, t) - T_1 y_1''(z, t) &= -\rho_1 A_1 \ddot{y}_1(z, t) \\
[EI_1 y_1'''(L_1, t) - T_1 y_1'(L_1, t)] - [EI_2 y_2'''(0, t) - T_2 y_2'(0, t)] &= M_1 \ddot{y}_1(L_1, t) \\
y_1(0, t) &= 0, \tag{5.21}
\end{aligned}$$

$$\begin{aligned}
EI_2 y_2''''(z, t) - T_2 y_2''(z, t) &= -\rho_2 A_2 \ddot{y}_2(z, t) \\
[EI_2 y_2''''(L_2, t) - T_2 y_2''(L_2, t)] - [EI_3 y_3''''(0, t) - T_3 y_3''(0, t)] &= M_2 \ddot{y}_2(L_2, t) \\
y_2(0, t) &= y_1(L_1, t),
\end{aligned} \tag{5.22}$$

$$\begin{aligned}
EI_3 y_3''''(z, t) - T_3 y_3''(z, t) &= -\rho_3 A_3 \ddot{y}_3(z, t) \\
[EI_3 y_3''''(L_3, t) - T_3 y_3''(L_3, t)] - [EI_4 y_4''''(0, t) - T_4 y_4''(0, t)] &= M_3 \ddot{y}_3(L_3, t) \\
y_3(0, t) &= y_2(L_2, t),
\end{aligned} \tag{5.23}$$

$$\begin{aligned}
EI_4 y_4''''(z, t) - T_4 y_4''(z, t) &= -\rho_4 A_4 \ddot{y}_4(z, t) \\
EI_4 y_4''''(L_4, t) - T_4 y_4''(L_4, t) &= M_4 \ddot{y}_4(L_4, t) \\
y_4(0, t) &= y_3(L_3, t).
\end{aligned} \tag{5.24}$$

We now set $E = 0$, define:

$$\begin{aligned}
k_i &= \omega \sqrt{\frac{\rho_i A_i}{T_i}} \\
\mu_i &= \frac{T_{i+1}}{M_i g},
\end{aligned} \tag{5.25}$$

and rewrite the equations (5.21), (5.22), (5.23), (5.24) as:

$$y_i''(z) = -k_i^2 y_i(z). \tag{5.26}$$

As we can see from eq. (5.26) each wire suspending a filter has the general solution:

$$y_i(z) = \alpha_i \sin(k_i z) + \beta_i \cos(k_i z), \tag{5.27}$$

with the boundary conditions:

$$\begin{aligned}
y_1(0) &= 1 \\
y_i(L_i) &= y_{i+1}(0), \quad i \in [1, n-1] \\
\mu_i y'_{i+1}(0) - (1 + \mu_i) y'_i(L_i) &= -\frac{\omega^2}{g} y_i(L_i), \quad i \in [1, n-1] \\
y'_n(L_n) &= \frac{\omega^2}{g} y_n(L_n).
\end{aligned} \tag{5.28}$$

Explicitly we have the following set of equations:

$$\begin{aligned}
y_1(z) &= \alpha_1 \sin(k_1 z) + \beta_1 \cos(k_1 z) \\
y_2(z) &= \alpha_2 \sin(k_2 z) + \beta_2 \cos(k_2 z) \\
y_3(z) &= \alpha_3 \sin(k_3 z) + \beta_3 \cos(k_3 z) \\
y_4(z) &= \alpha_4 \sin(k_4 z) + \beta_4 \cos(k_4 z),
\end{aligned} \tag{5.29}$$

and the following set of boundary conditions to be solved for the variables α_i, β_i :

$$\begin{aligned}\mu_1 y_2'(0) - (1 + \mu_1) y_1'(L_1) &= -\frac{\omega^2}{g} y_1(L_1) \\ y_1(0) &= 0,\end{aligned}\tag{5.30}$$

$$\begin{aligned}\mu_2 y_3'(0) - (1 + \mu_2) y_2'(L_2) &= -\frac{\omega^2}{g} y_2(L_2) \\ y_1(L_1) &= y_2(0),\end{aligned}\tag{5.31}$$

$$\begin{aligned}\mu_3 y_4'(0) - (1 + \mu_3) y_3'(L_3) &= -\frac{\omega^2}{g} y_3(L_3) \\ y_2(L_2) &= y_3(0),\end{aligned}\tag{5.32}$$

$$\begin{aligned}y_4'(L_4) &= \frac{\omega^2}{g} y_4(L_4) \\ y_3(L_4) &= y_4(0).\end{aligned}\tag{5.33}$$

In the above set of equations the first ones represent the motion equations for the various pendulum stages, while the second ones represent the boundary conditions for the positions of the stages.

Transfer functions

Once we have obtained the motion equations we compute the transfer functions for the various stages of the pendulum following the methods explained in Appendix B. The transfer functions obtained are shown in fig. 5.8, while fig. 5.9 shows the total transfer function for the suspension system, including the inverted pendulum.

5.3 Sensitivity curve of the Michelson suspended interferometer

This last section is devoted to the theoretical calculus of the sensitivity curve of the 3mx3m Michelson interferometer under development in Virgo Lab in Napoli [39].

We will analyze the performances of the interferometer and the various noise sources which are expected to limit the sensitivity of this device.

The main noise contributions according to their sources can be divided into:

- environmental noises: seismic, magnetic and newtonian noise
- optical noises: shot noise, radiation pressure noise
- thermal noise in the mechanical suspensions and in the optical components

In the following equations the spectral amplitude of the variuos noises will be expressed in terms of h , in units of $1/\sqrt{Hz}$. The relative displacement spectrum can be obtained from: $\Delta L = \frac{1}{2} L_{arm} h$, where L_{arm} represents the nominal length of the interferometer arm.

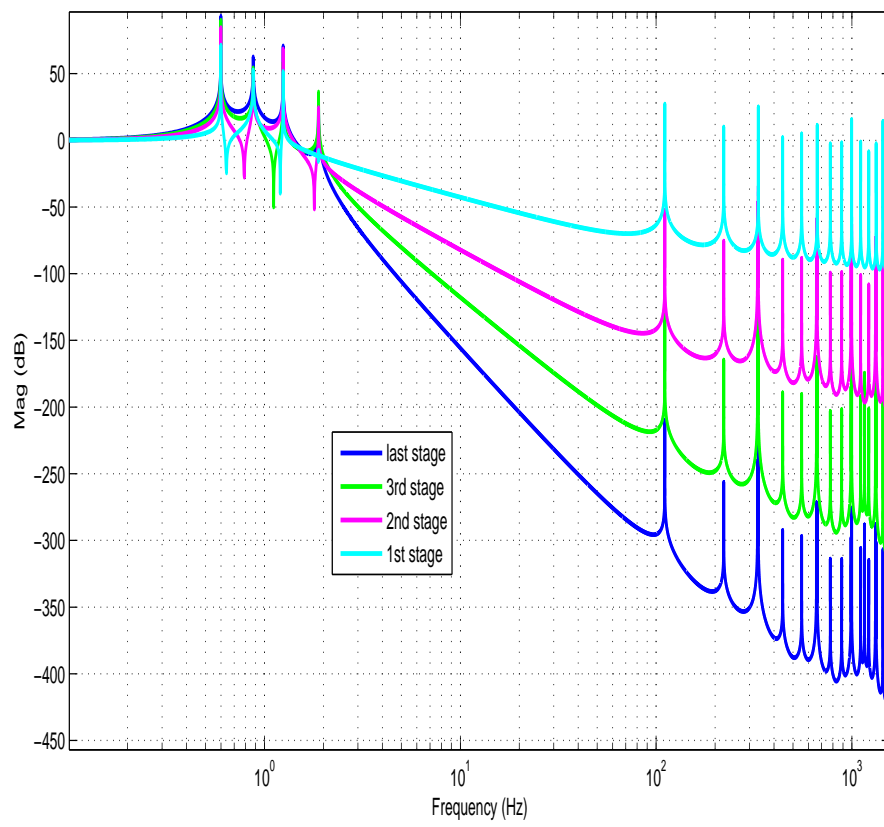


Figure 5.8: Transfer function for the four stages pendulum.

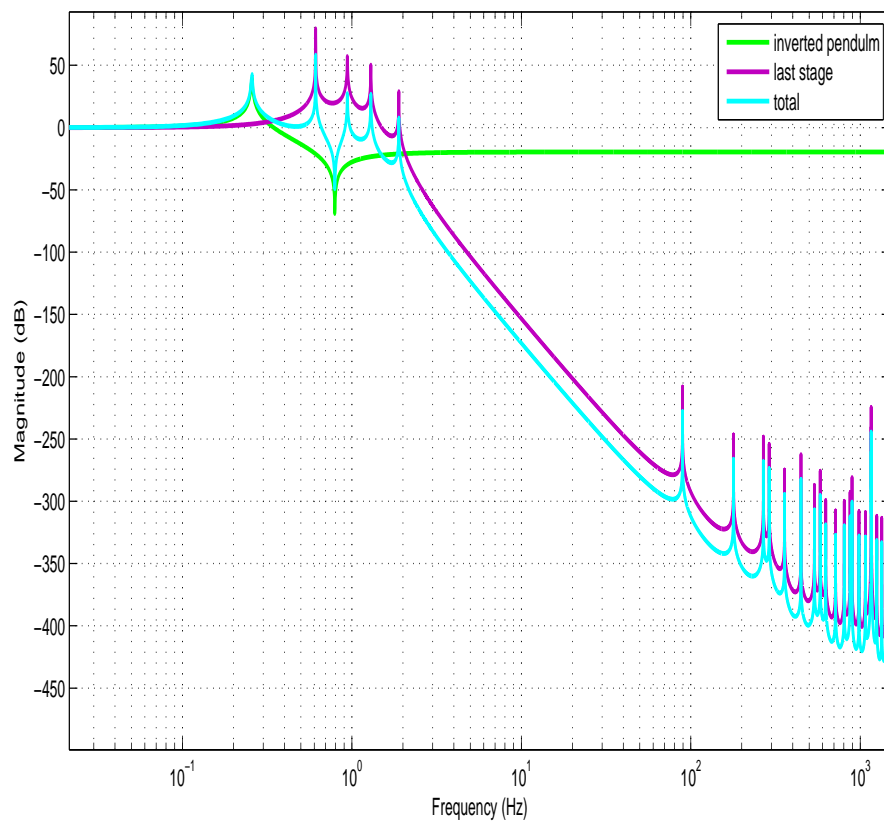


Figure 5.9: Total transfer function for the suspension system.

5.3.1 Environmental noise

Seismic noise

Seismic motion is one of the unavoidable noise sources for interferometers built on the Earth's crust. This motion can be excited by natural phenomena like macro-seismic, oceanic, and atmospheric activities, as well as by human activities. We adopt a seismic spectral amplitude:

$$\tilde{x}(f) \approx \frac{A_0}{f^2}. \quad (5.34)$$

with $A_0 = 10^{-7}$. This noise is very well filtered by the ULF suspension system, whose total transfer function is H_{TF} .

The equivalent h for seismic noise is:

$$h_{seism}(f) = \frac{\sqrt{4}}{L_{arm}} \sqrt{H_{TF}^2} \tilde{x}(f). \quad (5.35)$$

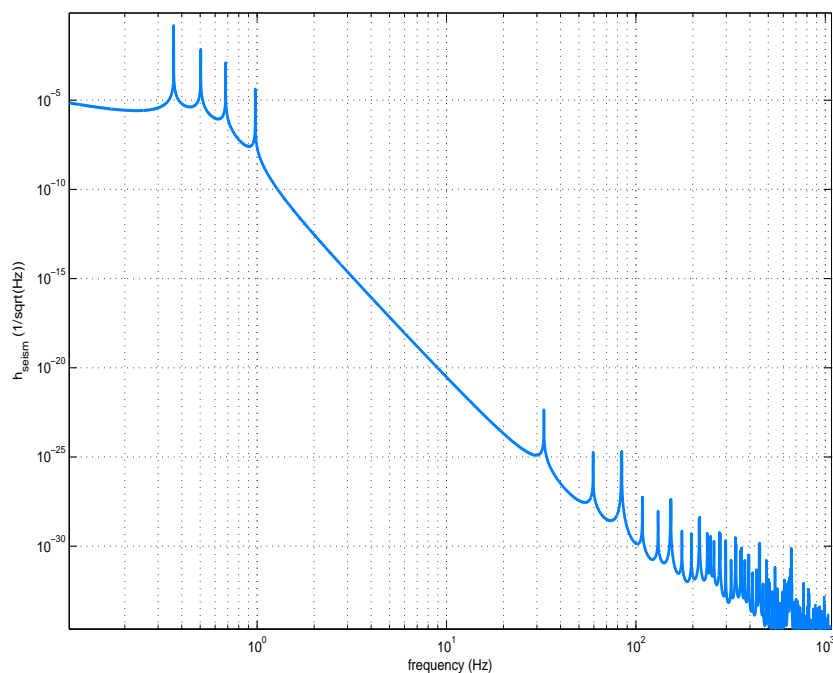


Figure 5.10: Spectrum of the seismic noise.

Newtonian and magnetic noise

The newtonian noise is given by static gravitational field modulation by the seismic noise [40].

The equivalent h for this noise is:

$$h_{\text{NN}}(f) = \frac{3 \cdot 10^{-11}}{f^2} \tilde{x}_{\text{seism}}(f). \quad (5.36)$$

The seismic noise and the presence of magnets on the marionetta have effect on the interferometer sensitivity.

The equivalent h given by magnetic noise is given by:

$$h_{\text{mag}}(f) = H_m \frac{2}{L_{\text{arm}}} \cdot \sqrt{\tilde{x}_{\text{M1}}^2 + \tilde{x}_{\text{M2}}^2 + \tilde{x}_{\text{M3}}^2}, \quad (5.37)$$

where the first contribution is due to diamagnetic marionetta tower coupling, the second to eddy currents on the tower walls, and the last one to marionetta fluctuation due to eddy currents [41].

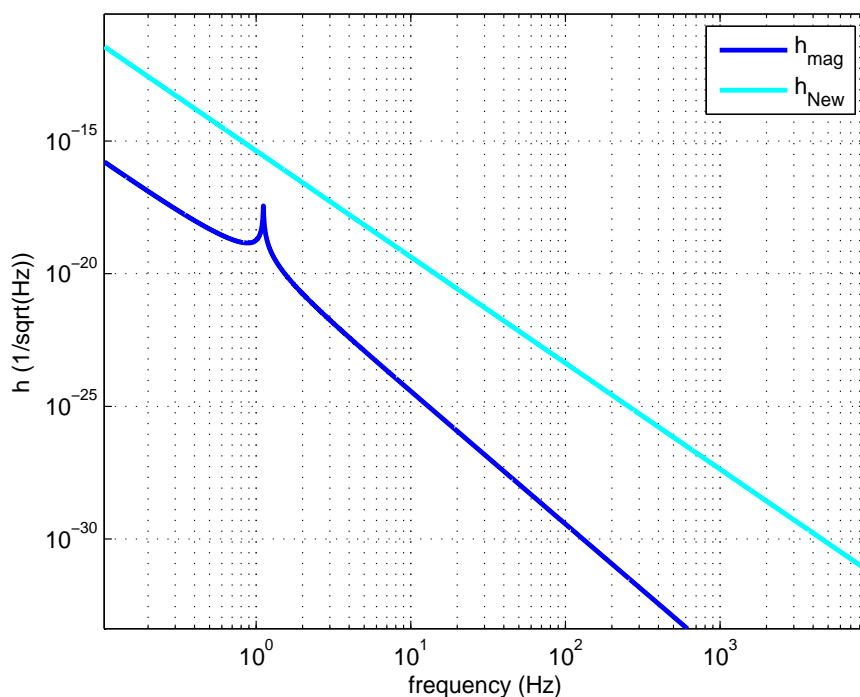


Figure 5.11: Spectrum of the magnetic and newtonian noise.

5.3.2 Optical noise

Shot noise and radiation pressure noise

The photon *shot noise* arises from the quantum nature of light and gives the noise at the output of the interferometer linked to the smallest detectable change in the optical power [42].

This noise is one of the fundamental limits to the sensitivity of interferometers and is described by a

white spectral density of magnitude:

$$h_{shot}(f) = \frac{1}{L_{arm}} \sqrt{\frac{h_p \lambda c}{4\eta \pi^2 P_{las}}}. \quad (5.38)$$

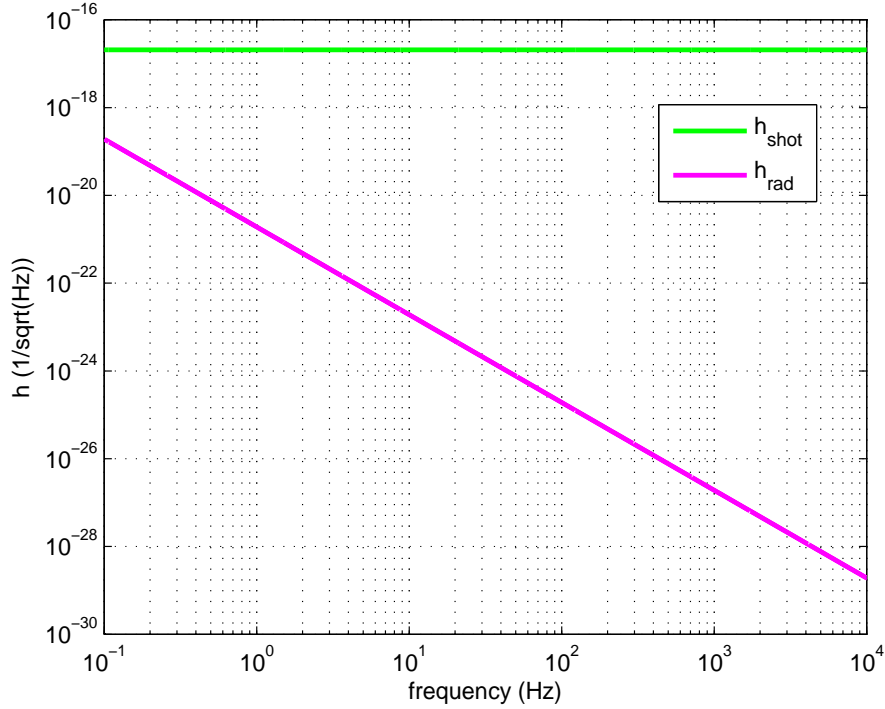


Figure 5.12: Spectrum of the shot noise and radiation pressure noise.

The *radiation pressure noise* is linked to the quantum nature of light, as the *shot noise*, but it scales with the light power in an opposite way. It represents the force exerted by an electromagnetic wave reflecting from a mirror: as light power increases the radiation pressure grows up.

The radiation pressure noise expression is:

$$h_{rad}(f) = \frac{1}{L_{arm} M_m f^2} \sqrt{\frac{h_p P_{las}}{4\pi^4 c \lambda}}. \quad (5.39)$$

The *shot noise* and the *radiation pressure noise* can be considered as two faces of a single noise: the *optical readout noise*, give by the quadrature sum:

$$h_{o.r.o.}(f) = \sqrt{h_{shot}^2(f) + h_{rad}^2(f)}. \quad (5.40)$$

At low frequencies the radiation pressure term will dominate, while at high frequencies the *shot noise* is more important. At any given frequency f_0 there is a minimum noise spectral density; this occurs when the power P_{las} is chosen to have the value P_{opt} that yields $h_{shot}(f_0) = h_{rad}(f_0)$. When we plug the expression

for P_{opt} into the formula for $h_{o.r.o.}$, we find:

$$h_{QL}(f) = \frac{1}{\pi f L_{arm}} \sqrt{\frac{\hbar}{M_m}}. \quad (5.41)$$

This is the so called *standard quantum limit*, to emphasize its fundamental relationship to quantum mechanical limits to the precision of measurements.

5.3.3 Thermal noise

Besides the discreteness of light as a fundamental limit to the sensitivity of interferometers, an equally fundamental limit exists on the degree to which a test mass can remain at rest: this phenomenon is generally called *thermal noise*. It indicates fluctuations affecting a physical observable of a macroscopic system at thermal equilibrium with its environment. The internal energy of a macroscopic apparatus at thermal equilibrium is shared between all its degree of freedom or, equivalently, between all its normal modes each carrying an average energy $K_B T$. Such an energy manifests itself as a random fluctuation of the relevant observable experimentally perceived as the noise affecting its measured value. In this picture thermal noise is a prototype of *displacement noise*.

In seismic inteferometers we are interested in energy loss processes in the suspension wires and test masses [43] [44]: if we treat the whole suspension structure as a multi stage pendulum the action of thermal noise will make the position of each element of the pendulum chain fluctuate in time.

This is particularly true for the position of the optical components located at the last stage of the chain.

Fluctuation-Dissipation theorem

The calculus of thermal noise from various sources of dissipation may be performed using the *Fluctuation-Dissipation theorem*. This theorem establishes the relation between fluctuation and dissipation.

The theorem states that if $z(t)$ is any degree of freedom of any oscillator driven by the conjugated force $F(t)$, then fluctuations of F due to temperature T give rise to fluctuations of z having the following spectral density:

$$S_z(f) = \frac{4K_B T}{\omega^2} \Re\{\sigma(\omega)\}, \quad (5.42)$$

where

$$\sigma(\omega) = \frac{v(f)}{F(f)} \quad (5.43)$$

represents the mechanical conductance. We list now various contributions to thermal noise from different sources. The detailed calculus of their final expressions can be found in appendix C.

Suspension wires thermal noise

Suspension wires contribute to thermal noise through 3 processes:

- Pendulum thermal oscillation
- Vertical thermal oscillation
- Violin modes

These three contributions are shown in fig. 5.13.

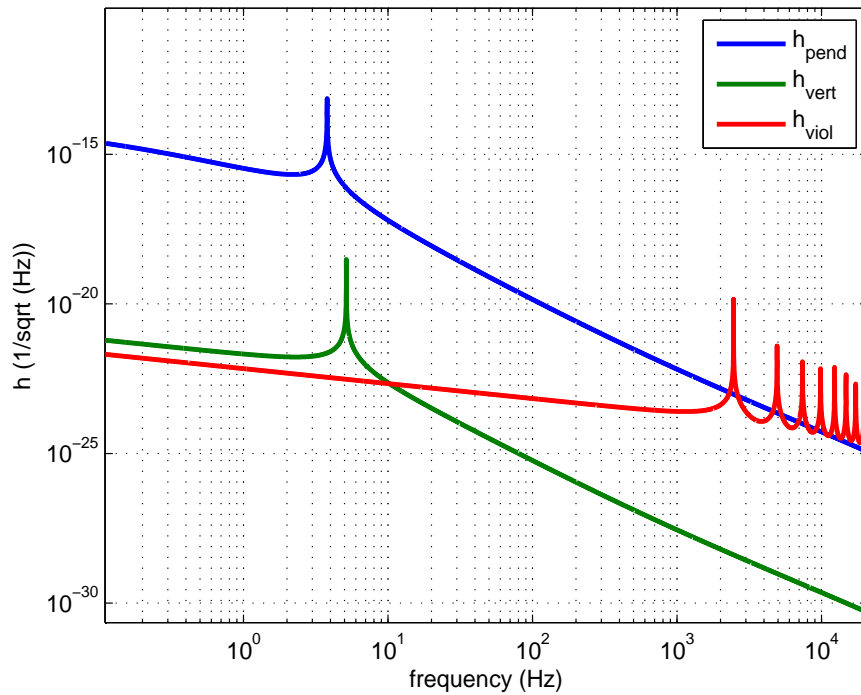


Figure 5.13: Spectrum of the suspension wires thermal noise.

Test mass thermal noise

The test mass thermal noise can be computed in two different ways: expanding the vibrating state of the mirror on the basis of normal modes, or considering the static deformation of the mirror under a gaussian pressure. Fig. 5.14 shows this contribution.

Thermodynamical noise and heating by laser beam

Other important thermal noise sources are coating and bulk thermodynamical contributions, shown in fig. 5.15, and thermal noise linked to the heating by laser beam, shown in fig. 5.16.

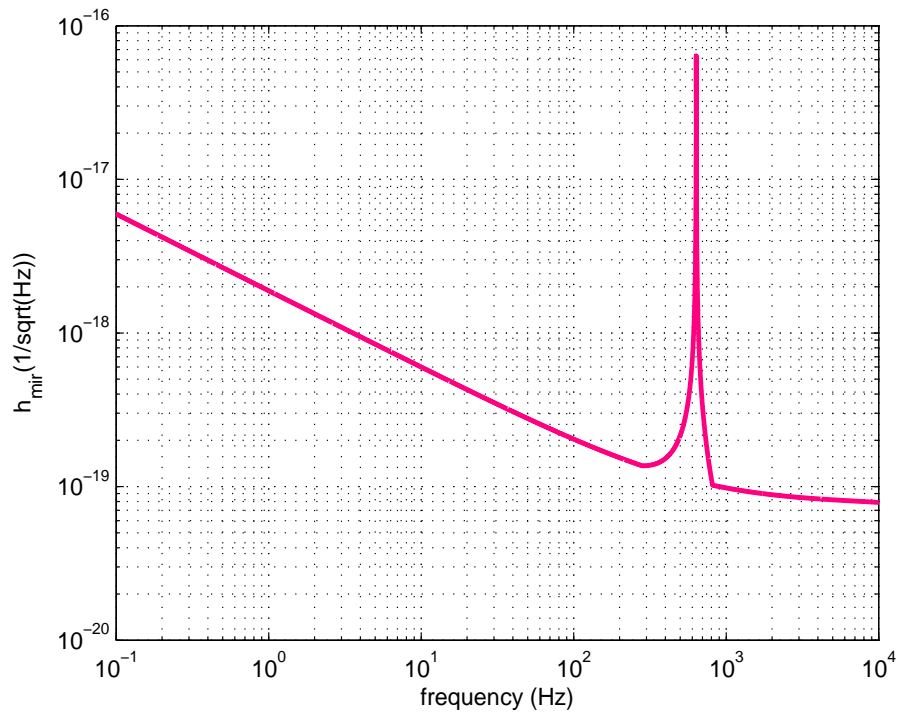


Figure 5.14: Spectrum of the test mass thermal noise.

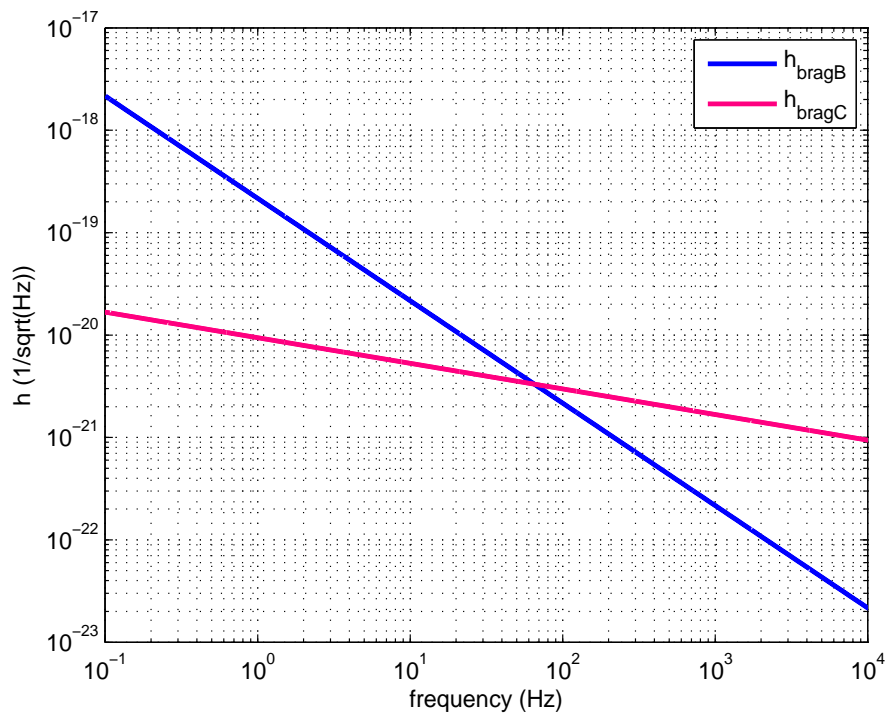


Figure 5.15: Spectrum of the coating and bulk thermodynamical noise.

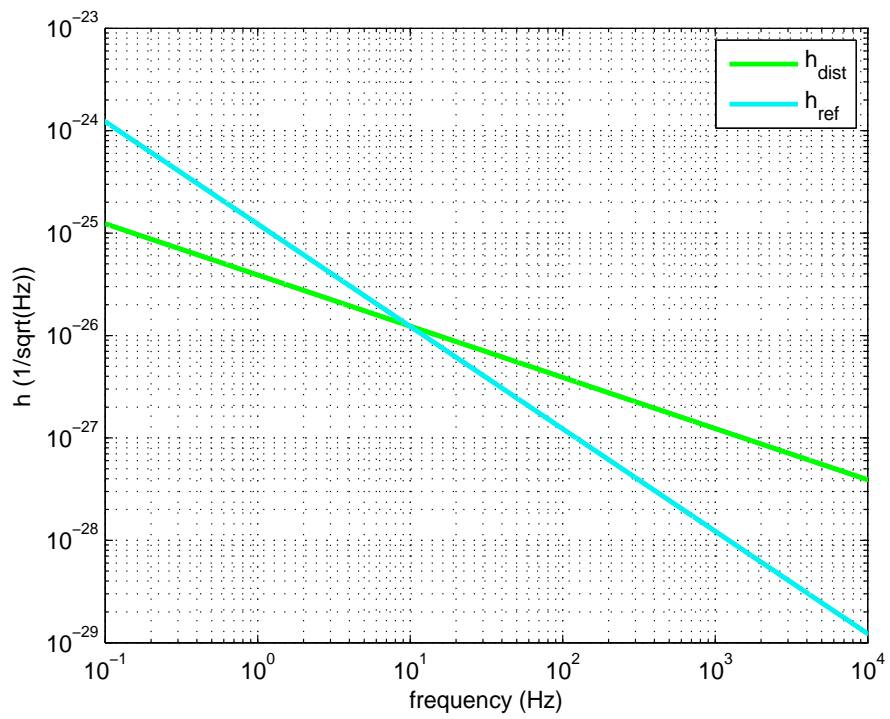


Figure 5.16: Spectrum of the noise due to distortion by laser heating and phase reflectivity of the coating.

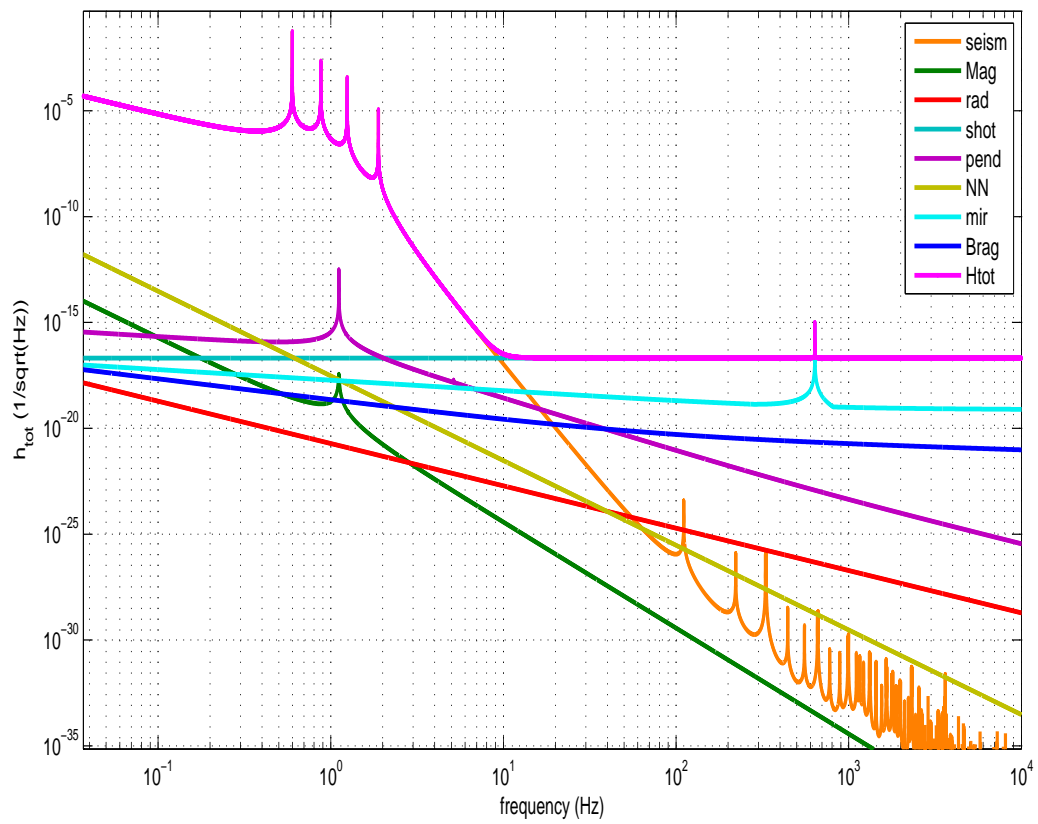


Figure 5.17: Interferometer sensitivity curve (various contributions).

Conclusions

This thesis work has been developed to study the feasibility of a new seismometer using a Fabry Perot cavity with a suspended mirror. To this aim several steps have been performed.

The first step consisted in the detailed analysis of the working principle of the currently used seismometers, paying particular attention to the systems used to isolate the sensing mass from the ground motion and to read its position. Besides seismometers several applications of the Michelson and Fabry Perot interferometers for geophysical purposes have been analyzed.

The second step consisted in the design of a Fabry Perot cavity usable for seismic measurements. This cavity is a plane-concave one, with the plane mirror suspended to the last stage of a double pendulum, in order to isolate it from the ground motion in the frequency band higher than its resonances. This design required a detailed theoretical study both of the optical cavity properties and of the suspension system. The theoretical studies of the optical cavity concern the response of a suspended and misaligned Fabry Perot cavity. The studies of the suspension system concern an alternative to the coil-magnet actuation system, based on the electrostatic actuation: the current theoretical model for the electrostatic actuation has been analyzed and refined and the new experimental data confirm that this system can represent a good alternative to the old actuation system, for the fine control of the last suspension stages.

Another step consisted in the assembling of the experimental set-up in all its parts; a preliminar set of measurements has been performed on a cavity with both mirrors fixed to the optical bench, in order to align the cavity in a standard configuration, and to test the fringe counting algorithm for the reconstruction of the motion by the reflected cavity power.

The last step consisted in the acquirement of all the significant data about the reconstruction of the relative mirror motion of the suspended cavity. This set of measurements has pointed out the current limitations in the reconstruction of the motion. The limitations are linked to the instantaneous variation of the modulation amplitude due to the residual motion of the suspended mirror, the narrow dynamical range of the piezoelectric actuator and low sampling frequency in the digital acquisition system.

Besides the development of the seismic sensor, several theoretical simulations about the overall performance on a 3mx3m Michelson interferometer have been performed in this work: this interferometer is currently under development in the Virgo lab in Napoli and seems to be very promising for sensitive seismic

measurements at very low frequencies. The simulations concern the lagrangian model and the transfer functions of the ULF suspension system, and the calculus of the sensitivity curve of the interferometer, with the analysis of the main noise contributions expected.

In conclusion we can state that there is no theoretical limitation about the use of the device developed in this work as a sensitive seismometer, but variuos improvements on the control of the suspended mass and the digital acquisition system are required in the experimental set-up.

Appendix A

Electric field by an array of electrodes in the presence of dielectrics

This appendix represents a complement to the chapter related to the control of suspended test mass in seismic interferometers: in this chapter we introduced a new kind of actuation system, the electrostatic actuation.

Here we will develop in detail the calculus of the electric field produced by a linear charge distribution, first in the free space, and then in the presence of various dielectrics to obtain the force exerted by the new actuator.

A.1 Free space electrodes

We start now with the calculus of the expression for the kernel G_{fs} in free space.

This expression can be easily obtained if we note that in the proximity of each electrode with positive charge it reduces to the Green's function G_{fs} of a single wire in free space [45]:

$$G_{\text{fs}}(\omega) = -\frac{1}{2\pi\epsilon_0} \Re \{ \ln[\omega] \} . \quad (\text{A.1})$$

Now we have to impose the periodicity condition of eq. (3.4); the properties required are verified by the function:

$$G_{\text{fs}}(\omega) = -\frac{1}{2\pi\epsilon_0} \Re \left\{ \ln \left[\tan \left(\frac{\pi\omega}{2b} \right) \right] \right\} . \quad (\text{A.2})$$

We normalize the variables with respect to the array period b , indicating the normalized variables with a

caret and work with the homogeneous integral equation:

$$\int_{-\hat{a}/2}^{\hat{a}/2} \frac{\partial}{\partial \hat{x}} G(\hat{x} - \hat{\zeta}) \rho_{\text{fs}}(\hat{\zeta}) d\hat{\zeta} = 0. \quad (\text{A.3})$$

In addition, considering points that lie on the electrode surface, the generally complex variable ω becomes real and, combining the above equation with eq. (A.2), we obtain:

$$\int_{-\hat{a}/2}^{\hat{a}/2} \frac{\rho_{\text{fs}}(\hat{\zeta})}{\sin \left| \pi(\hat{x} - \hat{\zeta}) \right|} d\hat{\zeta} = 0. \quad (\text{A.4})$$

This is a singular integral equation similar to those of the Cauchy type [46], which admits the integral $\rho_{\text{fs}}(\hat{\zeta}) \propto 1/\sqrt{\hat{a}^2/4 - \hat{\zeta}^2}$ singular at $\hat{x} = \pm\hat{a}/2$. In view of this it is worth expressing the charge density as a product of the above singular function times an unknown regular function y_{fs} :

$$\rho_{\text{fs}}(\hat{\zeta}) = \frac{y_{\text{fs}}(\hat{\zeta})}{\sqrt{\hat{a}^2/4 - \hat{\zeta}^2}}. \quad (\text{A.5})$$

Next, we introduce the coordinate ϕ defined by $\hat{\zeta} = (a/2) \sin \phi$ and putting $V_e = 1$ we recast eq. (A.4) in the form:

$$\int_0^{\pi/2} M_{\text{fs}}(\psi, \phi) y_{\text{fs}}(\phi) d\phi = 1, \quad (\text{A.6})$$

where

$$M_{\text{fs}}(\psi, \phi) = \ln \left| \tan \left(\pi \frac{\hat{a}}{4} |\sin \psi - \sin \phi| \right) \times \tan \left(\pi \frac{\hat{a}}{4} |\sin \psi + \sin \phi| \right) \right|. \quad (\text{A.7})$$

We can now put equation (A.6) in matrix form dividing the interval $[0, \pi/2]$ in N parts with extreme $\phi_i = ((i-1)/N)\pi/2, (i = 1 \cdots N+1)$ and centers $\bar{\phi}_i = ((i-0.5)/N)\pi/2, (i = 1 \cdots N)$. We obtain:

$$\mathbf{M}_{\text{fs}} \cdot \mathbf{y}_{\text{fs}} = \mathbf{1}, \quad (\text{A.8})$$

namely:

$$\sum_{j=1}^N M_{(\text{fs})ij} y_{(\text{fs})j} = 1, \quad i = 1, 2 \cdots N, \quad (\text{A.9})$$

with:

$$\begin{aligned} y_{(\text{fs})j} &= y_{\text{fs}}(\bar{\phi}_j) \\ M_{(\text{fs})ij} &= \frac{\pi}{4N} (M_{\text{fs}}(\bar{\phi}_i, \phi_j) + M_{\text{fs}}(\bar{\phi}_i, \phi_{j+1})), \quad i \neq j \\ M_{(\text{fs})ii} &= \int_{\phi_i}^{\phi_{i+1}} M_{\text{fs}}(\bar{\phi}_i, \phi) d\phi. \end{aligned} \quad (\text{A.10})$$

Inverting \mathbf{M}_{fs} in eq. (A.8) gives the vector:

$$\mathbf{y}_{\text{fs}} = \mathbf{1} \cdot \mathbf{M}_{\text{fs}}^{-1}. \quad (\text{A.11})$$

Finally, by multiplying both sides by the vector $(\pi/2)/N \mathbf{1}$ and by restoring the original dimensions we obtain for the capacity the following expression:

$$C_{\text{fs}} = \frac{\pi^2 \epsilon_0 L}{N} \mathbf{1} \cdot \mathbf{M}_{\text{fs}}^{-1} \cdot \mathbf{1}. \quad (\text{A.12})$$

A.2 Electrodes on a dielectric substrate

In order to realistically describe the strip actuator we have to take into account the presence of the dielectric slab of thickness h supporting the metallic strips.

Hence we use the method of images, considering sequentially the reflections from the slab surface and ignoring at the moment the presence of the mirror.

Starting from the reflection from the front, and continuing with the back, front surface and so on we define the sequence of reflection coefficients:

$$\gamma_s = \frac{\epsilon_s - \epsilon_0}{\epsilon_s + \epsilon_0}, \quad \gamma'_s = \frac{2\epsilon_s}{\epsilon_s + \epsilon_0}, \quad \gamma''_s = \frac{2\epsilon_0}{\epsilon_s + \epsilon_0}, \quad \gamma_m = \frac{\epsilon_m - \epsilon_0}{\epsilon_m + \epsilon_0}. \quad (\text{A.13})$$

The respective images are located at $\hat{z} = \hat{0}, 2\hat{h}, 4\hat{h}, \dots$, the Green's function G_{sub} is represented by a rapidly converging series:

$$G_{\text{sub}}(\hat{\omega}) = (1 - \gamma_s)G_{\text{fs}}(\hat{\omega}) + \gamma_s\gamma'_s\gamma''_s G_{\text{fs}}(\hat{\omega} + 2i\hat{h}) + \gamma_s^3\gamma'_s\gamma''_s G_{\text{fs}}(\hat{\omega} + 4i\hat{h}) + \dots \quad (\text{A.14})$$

Accordingly, the electrode-substrate system is equivalent for the half-space $\hat{z} < 0$ to a series of arrays, with the first element corresponding to the physical distribution scaled by the factor $1 - \gamma_s$. The higher order terms are placed at increasing distance from the electrode plane (see fig: A.1).

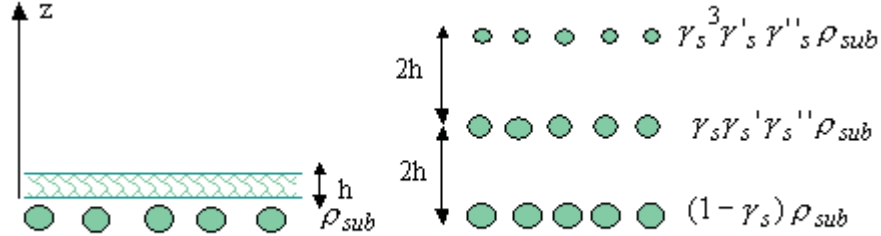


Figure A.1: Array of linear distributions on the dielectric substrate of thickness h and the equivalent system consisting of a series of arrays at distances $z = 0, 2h, 4h \dots$

The integral equation (A.4) becomes:

$$\int_{-\hat{a}/2}^{\hat{a}/2} \rho_{\text{sub}}(\hat{\zeta}) \left(\frac{1 - \gamma_s}{\sin[\pi(\hat{x} - \hat{\zeta})]} + \frac{\gamma_s\gamma'_s\gamma''_s}{\sin[\pi(\hat{x} - \hat{\zeta} + 2i\hat{h})]} + \frac{\gamma_s^3\gamma'_s\gamma''_s}{\sin[\pi(\hat{x} - \hat{\zeta} + 4i\hat{h})]} + \dots \right) d\hat{\zeta} = 0. \quad (\text{A.15})$$

In conclusion we can represent the effect of the substrate by introducing the factor $1 - \gamma_s$ in the free-space kernel, leading to:

$$M_{\text{sub}} = M_{\text{fs}}(1 - \gamma_s). \quad (\text{A.16})$$

Therefore from equations (A.12) and (A.16) the capacity C_{sub} in the presence of the dielectric slab becomes:

$$C_{\text{sub}} = \frac{C_{\text{fs}}}{1 - \gamma_s}. \quad (\text{A.17})$$

A.3 Electrodes in the presence of a mirror

We want now to take into account the presence of the mirror. In this situation the Green's function in eq. (A.14) modifies as:

$$G_{\text{m}}(\hat{\omega}) = (1 - \gamma_s)G_{\text{fs}}(\hat{\omega}) + \gamma_s \gamma'_s \gamma''_s G_{\text{fs}}(\hat{\omega} + 2i\hat{h}) + \gamma_s^3 \gamma'_s \gamma''_s G_{\text{fs}}(\hat{\omega} + 4i\hat{h}) - \gamma_m G_{\text{fs}}(\hat{\omega} - i\hat{d}) + \gamma_m \gamma_s G_{\text{fs}}(\hat{\omega} + i\hat{d}) + \dots. \quad (\text{A.18})$$

Accordingly the integral equation (A.6) becomes:

$$\int_0^{\pi/2} M_{\text{m}}(\psi, \phi) y_{\text{m}}(\phi) d\phi = 1, \quad (\text{A.19})$$

with

$$M_{\text{m}}(\psi, \phi) = (1 - \gamma_s)[M_{\text{fs}}(\psi, \phi) - \gamma_m M_{\text{d}}(\psi, \phi)], \quad (\text{A.20})$$

where

$$M_{\text{d}}(\psi, \phi) = 2\pi\epsilon_0 \left[G_{\text{fs}} \left(\frac{\hat{a}}{2}(\sin \psi - \sin \phi) - i\hat{d} \right) + G_{\text{fs}} \left(\frac{\hat{a}}{2}(\sin \psi + \sin \phi) - i\hat{d} \right) \right]. \quad (\text{A.21})$$

Using the matrix formalism we obtain that the capacity C_{m} is proportional to the capacity C_{sub} , namely:

$$C_{\text{m}} = \alpha C_{\text{sub}} \quad (\text{A.22})$$

through the factor

$$\alpha(\hat{d}) = \frac{\mathbf{1} \cdot \mathbf{M}_{\text{m}}^{-1} \cdot \mathbf{1}}{\mathbf{1} \cdot \mathbf{M}_{\text{sub}}^{-1} \cdot \mathbf{1}}. \quad (\text{A.23})$$

In conclusion the total force developed by the strip array is given by:

$$F_T = \frac{d\alpha(\hat{d})}{d\hat{d}} \frac{C_{\text{sub}}}{b} N V_e^2. \quad (\text{A.24})$$

Appendix B

Potential methods

This appendix represents a complement to the chapter related to the mechanical simulation of the ULF suspension system .

Here we will describe in detail the method followed to obtain the equation of motion for a chain of pendula, taking into account the internal modes of the wires connecting the various masses.

We will start with the study of the potential energy for an elastic line under tension with various boundary conditions and then specialize the problem for our real system of suspension.

We will first derive the lagrangian in the static approximation, then will introduce the violin modes of the wires and, at the end, we will describe a simple method to obtain the transfer function.

B.1 Potential energy of the elastic line

We start analyzing the equation of motion of an elastic line $y(z)$ under a tension T [47] [48]. Fig. B.1 shows the chosen coordinate system for the motion in the plane (y, z) .

The potential energy of the elastic line is:

$$U = \frac{1}{2} \int_0^L [EI(y'')^2 + Ty'^2] dz . \quad (\text{B.1})$$

By the use of a variational principle we obtain the equation of motion:

$$EI'''' - Ty'' = 0 , \quad (\text{B.2})$$

where E is the Young modulus and $I = \frac{\pi r^4}{4}$ the inertia of the beam. We can also express the equation (B.2) as:

$$I'''' - k^2 y'' = 0 , \quad (\text{B.3})$$

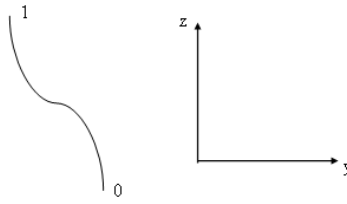


Figure B.1: The chosen coordinate system

where

$$k^2 = \frac{TL^2}{EI}. \quad (\text{B.4})$$

Once we have obtained the equation of motion we have to impose the boundary conditions, according to the situation we want to describe.

Clamped boundary conditions

We redefine now the unit length introducing $z = \xi L$. The four boundary conditions of clamp, for instance the position and orientation in $(0, L)$, are:

$$\mathbf{y}^T = (y(0), y'(0), y(1), y'(1)) \quad (\text{B.5})$$

and the most general solution for the elastic line equation is given by:

$$y(\xi) = (\sinh k\xi, \cosh k\xi, k\xi, 1) \cdot \mathbf{c}, \quad (\text{B.6})$$

where $\mathbf{c} = (c_1, c_2, c_3, c_4)$ is a vector of coefficients. Then the potential energy can be written in "matrix" form, noting that:

$$y''(\xi)^2 = k^4 \mathbf{c}^T \cdot \mathbf{Y}_2(\xi) \cdot \mathbf{c}, \quad (\text{B.7})$$

where the nonzero entries of the matrix \mathbf{Y}_2 are:

$$\mathbf{Y}_2 [1 : 2, 1 : 2] \equiv \begin{bmatrix} \sinh(k\xi)^2 & \sinh k\xi \cosh k\xi \\ \sinh k\xi \cosh k\xi & \cosh(k\xi)^2 \end{bmatrix}. \quad (\text{B.8})$$

With analogous formulas for $y'(\xi)$ we define the integrand of U and then:

$$U = \frac{TL}{2} \frac{k^2}{L^2} \mathbf{c} \cdot \mathbf{A} \cdot \mathbf{c}, \quad (\text{B.9})$$

where

$$\mathbf{A} [1 : 3, 1 : 3] = \begin{bmatrix} \frac{\sinh(2k)}{2k} & \frac{\sinh(k)^2}{k} & \frac{\sinh(k)}{k} \\ \frac{\sinh(k)^2}{k} & \frac{\sinh(2k)}{2k} & \frac{2 \sinh(\frac{k}{2})^2}{k} \\ \frac{\sinh(k)}{k} & \frac{2 \sinh(\frac{k}{2})^2}{k} & 1 \end{bmatrix}. \quad (\text{B.10})$$

To obtain the potential energy as a function of the boundary conditions \mathbf{x} , we impose the boundary relations:

$$\mathbf{B} \cdot \mathbf{c} = \mathbf{x}, \quad (\text{B.11})$$

where the matrix \mathbf{B} is:

$$\mathbf{B} = \begin{bmatrix} 0 & 1 & 0 & 1 \\ k & 0 & k & 0 \\ \sinh(k) & \cosh(k) & k & 1 \\ k \cosh(k) & k \sinh(k) & k & 0 \end{bmatrix}. \quad (\text{B.12})$$

It follows that

$$U = \frac{TL}{2} \mathbf{x}^T \cdot \mathbf{W} \cdot \mathbf{x}, \quad (\text{B.13})$$

where the matrix \mathbf{W} is given by:

$$\mathbf{W} = \frac{k}{L^2[k - 2 \tanh(\frac{k}{2})]} \times \begin{bmatrix} 1 & \frac{\tanh(k/2)}{k} & -1 & \frac{\tanh(k/2)}{k} \\ \frac{\tanh(k/2)}{k} & \frac{1}{k} \left(\frac{1}{\tanh(k)} - \frac{1}{k} \right) & -\frac{\tanh(k/2)}{k} & \frac{1}{k} \left(\frac{\tanh(k/2)}{k} - \frac{1}{\cosh k} \right) \\ -1 & -\frac{\tanh(k/2)}{k} & 1 & -\frac{\tanh(k/2)}{k} \\ \frac{\tanh(k/2)}{k} & \frac{1}{k} \left(\frac{\tanh(k/2)}{k} - \frac{1}{\cosh k} \right) & -\frac{\tanh(k/2)}{k} & \frac{1}{k} \left(\frac{1}{\tanh(k)} - \frac{1}{k} \right) \end{bmatrix}. \quad (\text{B.14})$$

A similar formula holds for the x coordinate: taking into account that the variable z has been rescaled to $z = L\xi$ and referring to fig. B.1, the correspondence between derivative x', y' and rotation angles around axes \mathbf{y}, \mathbf{x} are:

$$\begin{aligned} x'(0, 1) &= +L\theta_y(0, 1) \\ y'(0, 1) &= -L\theta_x(0, 1). \end{aligned} \quad (\text{B.15})$$

Hence the total potential energy of the elastic line is given by:

$$\begin{aligned} \mathbf{U} &= \frac{TL}{2} [\mathbf{y}^T \cdot \mathbf{W} \cdot \mathbf{y} + \mathbf{x}^T \cdot \mathbf{W} \cdot \mathbf{x}] \\ \mathbf{x} &= (x(0), L\theta_y(0), x(1), L\theta_y(1)) \\ \mathbf{y} &= (y(0), -L\theta_x(0), y(1), -L\theta_x(1)). \end{aligned} \quad (\text{B.16})$$

Approximations of W

The parameter k is generally rather large. In the limit of large tension we can expand the hyperbolic functions in the expression of W .

We can set $\tanh(k/2) \approx 1$ and $\cosh \approx \infty$ obtaining with very good approximation:

$$\mathbf{W} = \frac{k}{L^2[k-2]} \begin{bmatrix} 1 & \frac{1}{k} & -1 & \frac{1}{k} \\ \frac{1}{k} & \frac{k-1}{k^2} & -\frac{1}{k} & \frac{1}{k^2} \\ -1 & -\frac{1}{k} & 1 & -\frac{1}{k} \\ \frac{1}{k} & \frac{1}{k^2} & -\frac{1}{k} & \frac{k-1}{k^2} \end{bmatrix}. \quad (\text{B.17})$$

This expression can be further expanded in $1/k$.

Large tension limit

In the case in which $k \rightarrow \infty$, we obtain:

$$\mathbf{W}_0 = \frac{1}{L^2} \begin{bmatrix} 1 & 0 & -1 & 0 \\ 0 & 0 & 0 & 0 \\ -1 & 0 & 1 & 0 \\ 0 & 0 & 0 & 0 \end{bmatrix}. \quad (\text{B.18})$$

In this situation the potential energy is simply:

$$U \approx U_0 \equiv \frac{TL}{2} \left\{ \left[\frac{y(0) - y(1)}{L} \right]^2 + \left[\frac{x(0) - x(1)}{L} \right]^2 \right\}, \quad (\text{B.19})$$

which is the same formula that would result by considering the elastic line as a rigid constraint of length L .

The first correction to this formula comes by retaining in the formula (B.17) the $1/k$ term. We get:

$$\mathbf{W} \approx \mathbf{W}_0 + \mathbf{W}_1 + O(1/k^2), \quad (\text{B.20})$$

where

$$\mathbf{W}_1 = \frac{1}{kL^2} \begin{bmatrix} 2 & 1 & -2 & 1 \\ 1 & 1 & -1 & 0 \\ -2 & -1 & 2 & -1 \\ 1 & 0 & -1 & 1 \end{bmatrix}. \quad (\text{B.21})$$

Hence the potential is given by:

$$U \approx U_0 + U_1, \quad (\text{B.22})$$

where

$$U_1 = \frac{TL}{2} \frac{1}{k} \left\{ \left[\frac{x(0) - x(1)}{L} + \theta_y(0) \right]^2 + \left[\frac{x(0) - x(1)}{L} + \theta_y(1) \right]^2 + \left[\frac{y(0) - y(1)}{L} - \theta_x(0) \right]^2 + \left[\frac{y(0) - y(1)}{L} - \theta_x(1) \right]^2 \right\}. \quad (\text{B.23})$$

The second correction in $1/k$ to the matrix \mathbf{W} is:

$$\mathbf{W}_2 = \frac{1}{k^2 L^2} \begin{bmatrix} 4 & 2 & -4 & 2 \\ 2 & 1 & -2 & 1 \\ -4 & -2 & 4 & -2 \\ 2 & 1 & -2 & 1 \end{bmatrix}. \quad (\text{B.24})$$

Thus we obtain for the potential energy:

$$U \approx U_0 + U_1 + U_2, \quad (\text{B.25})$$

where

$$U_2 = \frac{TL}{2} \frac{4}{k^2} \left\{ \left[\frac{x(0) - x(1)}{L} + \frac{\theta_y(0) + \theta_y(1)}{2} \right]^2 + \left[\frac{y(0) - y(1)}{L} - \frac{\theta_x(0) + \theta_x(1)}{2} \right]^2 \right\}. \quad (\text{B.26})$$

In the more general case of four suspended masses M_1, M_2, M_3, M_4 through four wires with length L_1, L_2, L_3, L_4 under the tensions $T_1 = g(M_1 + M_2 + M_3 + M_4), T_2 = g(M_2 + M_3 + M_4), T_3 = g(M_3 + M_4), T_4 = gM_4$ the potential contributions of the wires for both variables x and y are:

$$\begin{aligned} U_{W1} = & \frac{T_1 L_1}{2} \left\{ \left[\frac{y_1(0) - y_1(L_1)}{L_1} \right]^2 + \left[\frac{x_1(0) - x_1(L_1)}{L_1} \right]^2 \right\} + \\ & + \frac{T_1 L_1}{2} \frac{1}{k} \left\{ \left[\frac{x_1(0) - x_1(L_1)}{L_1} + \theta_{y1}(0) \right]^2 + \left[\frac{x_1(0) - x_1(L_1)}{L_1} + \theta_{y1}(L_1) \right]^2 + \right. \\ & + \left. \left[\frac{y_1(0) - y_1(L_1)}{L_1} - \theta_{x1}(0) \right]^2 + \left[\frac{y_1(0) - y_1(L_1)}{L_1} - \theta_{x1}(L_1) \right]^2 \right\} + \\ & + \frac{T_1 L_1}{2} \frac{4}{k^2} \left\{ \left[\frac{x_1(0) - x_1(L_1)}{L_1} + \frac{\theta_{y1}(0) + \theta_{y1}(L_1)}{2} \right]^2 + \right. \\ & + \left. \left[\frac{y_1(0) - y_1(L_1)}{L_1} - \frac{\theta_{x1}(0) + \theta_{x1}(L_1)}{2} \right]^2 \right\}, \end{aligned} \quad (\text{B.27})$$

$$\begin{aligned} U_{W2} = & \frac{T_2 L_2}{2} \left\{ \left[\frac{y_2(0) - y_2(L_2)}{L_2} \right]^2 + \left[\frac{x_2(0) - x_2(L_2)}{L_2} \right]^2 \right\} + \\ & + \frac{T_2 L_2}{2} \frac{1}{k} \left\{ \left[\frac{x_2(0) - x_2(L_2)}{L_2} + \theta_{y2}(0) \right]^2 + \left[\frac{x_2(0) - x_2(L_2)}{L_2} + \theta_{y2}(L_2) \right]^2 + \right. \\ & + \left. \left[\frac{y_2(0) - y_2(L_2)}{L_2} - \theta_{x2}(0) \right]^2 + \left[\frac{y_2(0) - y_2(L_2)}{L_2} - \theta_{x2}(L_2) \right]^2 \right\} + \\ & + \frac{T_2 L_2}{2} \frac{4}{k^2} \left\{ \left[\frac{x_2(0) - x_2(L_2)}{L_2} + \frac{\theta_{y2}(0) + \theta_{y2}(L_2)}{2} \right]^2 + \right. \\ & + \left. \left[\frac{y_2(0) - y_2(L_2)}{L_2} - \frac{\theta_{x2}(0) + \theta_{x2}(L_2)}{2} \right]^2 \right\}, \end{aligned} \quad (\text{B.28})$$

$$\begin{aligned}
U_{W3} = & \frac{T_3 L_3}{2} \left\{ \left[\frac{y_3(0) - y_3(L_3)}{L_3} \right]^2 + \left[\frac{x_3(0) - x_3(L_3)}{L_3} \right]^2 \right\} + \\
& + \frac{T_3 L_3}{2} \frac{1}{k} \left\{ \left[\frac{x_3(0) - x_3(L_3)}{L_3} + \theta_{y3}(0) \right]^2 + \left[\frac{x_3(0) - x_3(L_3)}{L_3} + \theta_{y3}(L_3) \right]^2 + \right. \\
& + \left. \left[\frac{y_3(0) - y_3(L_3)}{L_3} - \theta_{x3}(0) \right]^2 + \left[\frac{y_3(0) - y_3(L_3)}{L_3} - \theta_{x3}(L_3) \right]^2 \right\} + \\
& + \frac{T_3 L_3}{2} \frac{4}{k^2} \left\{ \left[\frac{x_3(0) - x_3(L_3)}{L_3} + \frac{\theta_{y3}(0) + \theta_{y3}(L_3)}{2} \right]^2 + \right. \\
& + \left. \left[\frac{y_3(0) - y_3(L_3)}{L_3} - \frac{\theta_{x3}(0) + \theta_{x3}(L_3)}{2} \right]^2 \right\}, \tag{B.29}
\end{aligned}$$

$$\begin{aligned}
U_{W4} = & \frac{T_4 L_4}{2} \left\{ \left[\frac{y_4(0) - y_4(L_4)}{L_4} \right]^2 + \left[\frac{x_4(0) - x_4(L_4)}{L_4} \right]^2 \right\} + \\
& + \frac{T_4 L_4}{2} \frac{1}{k} \left\{ \left[\frac{x_4(0) - x_4(L_4)}{L_4} + \theta_{y4}(0) \right]^2 + \left[\frac{x_4(0) - x_4(L_4)}{L_4} + \theta_{y4}(L_4) \right]^2 + \right. \\
& + \left. \left[\frac{y_4(0) - y_4(L_4)}{L_4} - \theta_{x4}(0) \right]^2 + \left[\frac{y_4(0) - y_4(L_4)}{L_4} - \theta_{x4}(L_4) \right]^2 \right\} + \\
& + \frac{T_4 L_4}{2} \frac{4}{k^2} \left\{ \left[\frac{x_4(0) - x_4(L_4)}{L_4} + \frac{\theta_{y4}(0) + \theta_{y4}(L_4)}{2} \right]^2 + \right. \\
& + \left. \left[\frac{y_4(0) - y_4(L_4)}{L_4} - \frac{\theta_{x4}(0) + \theta_{x4}(L_4)}{2} \right]^2 \right\}. \tag{B.30}
\end{aligned}$$

B.2 Violin modes

Until now we did not take into account the internal modes of the wires. The total Lagrangian of a thin wire including the kinetic energy is:

$$\mathcal{L} = \frac{1}{2} \int_0^L \rho A \left(\frac{\partial y(z, t)}{\partial t} \right)^2 dz - \frac{1}{2} \int_0^L \left[EI \left(\frac{\partial^2 y(z, t)}{\partial z^2} \right)^2 + T \left(\frac{\partial y(z, t)}{\partial z} \right)^2 \right] dz, \tag{B.31}$$

where A represents the wire section, ρA the linear mass density.

A *violin mode* is an oscillating solution of the motion equation derived from the Lagrangian (B.31) at frequency ω , so we have to solve the equation:

$$Ey'''' - Ty'' = \omega^2 \rho A y, \tag{B.32}$$

with the prescribed boundary conditions.

Analytic solution

We make the common ansatz for the solution of the (B.32):

$$y(z) = \sum_{i=1}^4 c_i e^{\lambda_i z} \tag{B.33}$$

which gives the algebraic equation, for each root:

$$EI\lambda_i^4 - T\lambda_i^2 - \omega^2\rho A = 0 \quad (\text{B.34})$$

whose general solution is:

$$\begin{aligned} \lambda_{1,2} &= \pm \sqrt{\frac{T}{2EI}} \sqrt{1 + \sqrt{1 + \frac{4\omega^2\rho AEI}{T^2}}} \\ \lambda_{3,4} &= \pm \sqrt{\frac{T}{2EI}} \sqrt{\sqrt{1 + \frac{4\omega^2\rho AEI}{T^2}} - 1}. \end{aligned} \quad (\text{B.35})$$

The solution is therefore of the form:

$$y(z) = A \cos \lambda_3(z) + B \sin \lambda_3(z) + C \cosh \lambda_1(z) + D \sinh \lambda_1(z). \quad (\text{B.36})$$

Imposing the boundary conditions we finally obtain the eigenvalue equation:

$$[\lambda_3 \sin \lambda_3 L + \lambda_1 \sinh \lambda_1 L] [\lambda_3 \sinh \lambda_1 L + \lambda_1 \sinh \lambda_3 L] = \lambda_1 \lambda_3 [\cos \lambda_3 L - \cosh \lambda_1 L]^2. \quad (\text{B.37})$$

This equation depends on ω through $\lambda_{1,3}$ and its solutions give the eigenfrequencies of the system.

B.3 Matrix method for transfer functions

We introduce now a simple method for the computation of the transfer functions.

Let us consider a chain of pendula connected by concentrated masses, and assume for simplicity a second order system; we can define for each wire the state vector:

$$\psi_i(z) = \begin{pmatrix} y_i(z) \\ y_i'(z) \end{pmatrix} \quad (\text{B.38})$$

and note that the motion equation:

$$Ty''(z) = -\omega^2\rho Ay(z) \quad (\text{B.39})$$

can be rewritten in first order form as:

$$\frac{d}{dz}\psi_i(z) = \mathbf{H} \cdot \psi_i(z), \quad (\text{B.40})$$

where

$$\mathbf{H} = \begin{bmatrix} 0 & 1 \\ -\frac{\omega^2\rho A}{T} & 0 \end{bmatrix}. \quad (\text{B.41})$$

The first order equation can be easily integrated giving:

$$\psi(L_i) = \mathbf{U}_i(L_i) \cdot \psi_i(0), \quad (\text{B.42})$$

where

$$\mathbf{U}_i(L_i) = e^{\mathbf{H}L_i} = \begin{bmatrix} \cos k_i L_i & \frac{1}{k_i} \sin k_i L_i \\ -k_i \sin k_i L_i & \cos k_i L_i \end{bmatrix} \quad (\text{B.43})$$

and as before $k_i = \omega \sqrt{\rho_i A_i / T_i}$. The boundary conditions introduced by each filter:

$$\begin{aligned} y_{i+1}(0) &= y_i(L_i) \\ T_{i+1} y'_{i+1}(0) - T_i y'_i(L_i) &= -\omega^2 M_i y_i(L_i) \end{aligned} \quad (\text{B.44})$$

can be rewritten in matrix form as:

$$\psi_{i+1}(0) = \mathbf{Z}_i \cdot \psi_i(L_i), \quad (\text{B.45})$$

with

$$\mathbf{Z}_i = \begin{bmatrix} 1 & 0 \\ -\omega^2 \frac{M_i}{T_{i+1}} & \frac{T_i}{T_{i+1}} \end{bmatrix}. \quad (\text{B.46})$$

These equations are closed by the motion equation for the last mass:

$$T_n y'_n(L_n) = \omega^2 M_n y_n(L_n). \quad (\text{B.47})$$

We introduce now the quantities:

$$\Phi_{n,1} = \mathbf{U}_n(L_n) \cdot \mathbf{Z}_{n-1} \cdots \mathbf{U}_1(L_1) \quad (\text{B.48})$$

and

$$\mathbf{Z}_n = \begin{bmatrix} 1 & 0 \\ -\frac{\omega^2}{g} & 1 \end{bmatrix}. \quad (\text{B.49})$$

As the matrices are, by construction, with unit determinant and:

$$\det \Phi_{n,1} = \prod_{i=2}^n \det \mathbf{Z}_{i-1} = \frac{T_1}{T_n} \quad (\text{B.50})$$

we obtain this expression for y_n :

$$y_n(L_n) = \frac{T_1}{T_n} \frac{1}{(\mathbf{Z}_n \cdot \Phi_{n,1})_{2,2}}. \quad (\text{B.51})$$

Once we have obtained the expression for $y_n(L_n)$ we can also obtain the transfer function for an intermediate element y_m from:

$$\psi_m(0) = \frac{(\mathbf{Z}_n \cdot \Phi_{n,m})_{2,2}}{\det \Phi_{n,m}} y_n(L_n) = \frac{T_1}{T_m} \frac{(\mathbf{Z}_n \cdot \Phi_{n,m})_{2,2}}{(\mathbf{Z}_n \cdot \Phi_{n,1})_{2,2}}. \quad (\text{B.52})$$

Appendix C

Thermal noise in seismic interferometers

This appendix represents a complement to Chapter 5 and contains the detailed calculus of thermal noises from various sources in seismic interferometers.

C.1 Suspension wires thermal noise

Pendulum mode

The force to displacement transfer function for the pendulum mode is:

$$H(\omega) = \frac{1}{M_m} \frac{1}{(\omega_0^2 - \omega^2) + i\omega_{0w}^2 \phi(\omega)}, \quad (\text{C.1})$$

with

$$\omega_{0w}^2 = \frac{k_{el}}{M_m} = \frac{4 \cdot 2 \cdot \sqrt{EI_2 \Lambda}}{2M_m, L_{wm}^2} \quad (\text{C.2})$$

where Λ is the wire tension

$$\Lambda = \frac{M_m g}{4} \quad I_2 = \frac{\pi r_w^4}{4}. \quad (\text{C.3})$$

The ω_0 frequency is given by:

$$\omega_0^2 = \omega_{0g}^2 + \omega_{0w}^2, \quad (\text{C.4})$$

with

$$\omega_{0g}^2 = \frac{g}{L_{wm}}. \quad (\text{C.5})$$

The loss angle expression is:

$$\phi(\omega) = \phi_w + \phi_e + \phi_{te}(\omega) = \phi_w + \phi_e + \Delta \frac{\omega \tau}{1 + (\omega \tau)^2}, \quad (\text{C.6})$$

where

$$\Delta = \frac{E_d \alpha_{std}^2 T}{c_{std}} \quad (\text{C.7})$$

and

$$\tau = \frac{c_{\text{std}} d_{\text{wm}}^2}{2.16 \cdot 2\pi \cdot k_{\text{std}}} . \quad (\text{C.8})$$

The various terms take into account the losses in the wire, the residual clamp losses and the thermoelastic effect, respectively [49].

From the Fluctuation-Dissipation theorem we obtain the horizontal displacement spectrum:

$$\langle x(\omega)^2 \rangle = \frac{4k_b T}{\omega} \cdot \Im\{H(\omega)\} = \frac{4k_b T}{\omega} \cdot [M_m \phi(\omega) \omega_{0w}^2] |H(\omega)|^2 , \quad (\text{C.9})$$

and the equivalent h for the thermal noise of the pendulum mode is:

$$h_{\text{pend}}(f) = \frac{2}{L_{\text{arm}}} \sqrt{\langle x(\omega)^2 \rangle} . \quad (\text{C.10})$$

Vertical oscillation

The force to displacement transfer function for the vertical mode is:

$$H_{vt}(\omega) = \frac{1}{M_m} \frac{1}{(\omega_{vt}^2 - \omega^2) + i\omega_{vt}^2 \phi(\omega)} , \quad (\text{C.11})$$

where

$$\omega_{vt}^2 = \frac{4\pi r_{\text{wm}}^2 E_d}{L_{\text{wm}} M_m} . \quad (\text{C.12})$$

The expression for the vertical displacement spectrum is:

$$\langle y(\omega)^2 \rangle = \frac{4k_b T}{\omega} \cdot [M_m \phi(\omega) \omega_{vt}^2] |H_{vt}(\omega)|^2 . \quad (\text{C.13})$$

The vertical displacement couples with the horizontal one through θ_0 , and the equivalent h for the thermal noise of the vertical mode is:

$$h_{vt}(f) = \frac{2\theta_0}{L_{\text{arm}}} \sqrt{\langle y(\omega)^2 \rangle} . \quad (\text{C.14})$$

Violin modes

The transverse modes of a pendulum wire (the so called *violin modes*) can be modelled as distributed systems.

We treat the wire as a flexible string under tension Mg ; the resonance frequencies are:

$$\omega_n = \frac{n\pi}{L_{\text{wm}}} \cdot \sqrt{\frac{M_m g}{4\rho_{\text{wd}} \pi r_{\text{wm}}^2}} \cdot \left(1 + \frac{2}{L_{\text{wd}}} \sqrt{\frac{4E_d I_2}{g M_m}} \right) \quad (\text{C.15})$$

and the squared amplitudes are:

$$\psi_n^2 = \frac{1}{n^2} \frac{2\rho_{\text{wd}} L_{\text{wm}}}{\pi M_m^2} . \quad (\text{C.16})$$

The loss angles have expression:

$$\phi_n = \frac{2\phi(\omega_n)}{L_{\text{wm}}} \sqrt{\frac{4E_d I_2}{M_m g}} \left[1 + \frac{(n\phi(\omega_n))^2}{2L_{\text{wm}}} \sqrt{\frac{4E_d I_2}{M_m g}} \right]^{-1} . \quad (\text{C.17})$$

The displacement spectrum is:

$$\langle x_{\text{viol}}(\omega) \rangle^2 = 4 \cdot \frac{4k_b T}{\omega} r_{\text{wm}}^2 \sum_n \frac{\psi_n^2 \omega_n^2 \phi_n}{(\omega_n^2 - \omega^2)^2 + (\omega_n^2 \phi_n^2)^2}, \quad (\text{C.18})$$

and the equivalent h results:

$$h_{\text{viol}}(f) = \frac{2}{L_{\text{arm}}} \sqrt{\langle x_{\text{viol}}(\omega) \rangle^2}. \quad (\text{C.19})$$

C.2 Test mass thermal noise

The test mass thermal noise can be computed in two different ways: expanding the vibrating state of the mirror on the basis of normal modes [50] [51], or considering the static deformation of the mirror under a gaussian pressure [52] [53].

The first approach is called *modal approach* and is based on the assumption that the matter constituting the mirror's substrate is moving due to brownian motion .

Another approach to calculate the thermal noise of the test mass is to calculate the strain energy U stored in the substrate by the laser beam pressure. In our model this pressure has a gaussian distribution, the beam width being w .

Modal approach

The motion of the matter must be considered within the framework of the classical linear theory of elasticity. In the case where the solid is modeled as a cylinder, each eigenmode is viewed as a series of Love modes.

The following items are followed:

- Find all normal elastic modes of the substrate
- Give the equal energy $K_B T$ to each mode and compute the corresponding amplitude
- Compute the coupling rate of each mode with the gaussian beam and convert the displacement amplitude into an effective displacement (a phase change)
- Sum all these contributions

Almost all the resonant frequencies are well above our detection band, so we can approximate the mass of the thermal mode (the mass of the part of the mirror which interacts with light) with the mass of the mirror.

This way we obtain an upper bound for thermal noise for the modal approach.

The following displacement spectrum is obtained:

$$\langle \tilde{x}_m(\omega) \rangle^2 = \frac{4k_b T}{\omega} \cdot \frac{\phi_{\text{quartz}} \cdot \omega_m^2}{M_m^{\text{eff}} [(\omega_m^2 - \omega^2)^2 + (\phi_{\text{quartz}} \cdot \omega_m^2)^2]}. \quad (\text{C.20})$$

Static deformation under a gaussian pressure

The energy U is calculated in the case of a finite cylinder having radius R_{mir} and thickness h_{m} . In what follows $J_p(z)$ are the Bessel functions and the $\{\zeta_m, m = 1, 2, \dots\}$ are the zeros of $J_1(z)$.

The displacement spectrum has the form:

$$\langle x_{\text{low}}(\omega) \rangle^2 = \frac{8k_b T}{\omega} \cdot \phi(\omega) \{U_0 + \Delta U\}, \quad (\text{C.21})$$

where

$$U_0 = \frac{1 - \sigma_{\text{m}}^2}{\pi E_{\text{m}} R_{\text{mir}}} \sum_{m=1}^{\infty} U_m \frac{\exp\left[-\left(\frac{\zeta_m w}{2R_{\text{mir}}}\right)^2\right]}{\zeta_m J_0(\zeta_m)^2}, \quad (\text{C.22})$$

with

$$U_m = \frac{1 - \exp\left[-\frac{4\zeta_m h_{\text{m}}}{R_{\text{mir}}}\right] + \left(\frac{4\zeta_m h_{\text{m}}}{R_{\text{mir}}}\right) \exp\left[-\frac{2\zeta_m h_{\text{m}}}{R_{\text{mir}}}\right]}{\left(1 - \exp\left[-\frac{2\zeta_m h_{\text{m}}}{R_{\text{mir}}}\right]\right)^2 - \left(\frac{4\zeta_m h_{\text{m}}}{R_{\text{mir}}}\right)^2 \exp\left[-\frac{2\zeta_m h_{\text{m}}}{R_{\text{mir}}}\right]} \quad (\text{C.23})$$

and

$$s = \sum_{m=1}^{\infty} \frac{\exp\left[-\frac{1}{2}\left(\frac{\zeta_m w}{2R_{\text{mir}}}\right)^2\right]}{\zeta_m^2 J_0(\zeta_m)}. \quad (\text{C.24})$$

The correction term ΔU is

$$\Delta U = \frac{R_{\text{mir}}^2}{6\pi h_{\text{m}}^3 E_{\text{m}}} \left[\left(\frac{h_{\text{m}}}{R_{\text{mir}}}\right)^4 + 12\sigma_{\text{m}} s \left(\frac{h_{\text{m}}}{R_{\text{mir}}}\right)^2 + 72(1 - \sigma_{\text{m}}) s^2 \right]. \quad (\text{C.25})$$

Using a combination of the two methods we obtain

$$h_{\text{mir}}(f) = \frac{\sqrt{2}}{L_{\text{arm}}} \sqrt{\max\{\langle x_{\text{m}}(\omega) \rangle^2, \langle x_{\text{low}}(\omega) \rangle^2\}}. \quad (\text{C.26})$$

To obtain h_{mir} the series for U_0 was truncated at the first 100 terms.

C.3 Thermodynamical noise in the mirrors

Even in presence of a perfectly stable light beam, at room temperature, in a finite volume, the temperature fluctuates and couples with the motion of the reflecting surface via the thermal expansion coefficient in the bulk, and with the phase reflectance via the thermal refractive index [54].

Thermodynamical fluctuations in the bulk

Concerning the thermodynamical fluctuations in the bulk the amplitude spectral density is:

$$h_{\text{bragB}}(f) = \frac{1}{L_{\text{arm}} f} \frac{2\sqrt{2} K_B k_{\text{m}} T \alpha_{\text{m}} (1 + \sigma_{\text{m}})}{\pi^{\frac{5}{4}} c_{\text{m}} \rho_{\text{m}}} \sqrt{\frac{2}{w^3}}. \quad (\text{C.27})$$

Thermodynamical fluctuations in the coating

Concerning the thermodynamical fluctuations in the coating the amplitude spectral density is:

$$h_{\text{bragC}}(f) = \frac{1}{L_{\text{arm}}} \frac{d\Phi}{dn} \frac{dn}{dT} \frac{\lambda}{4\pi} \frac{2\sqrt{2K_B T}}{(\pi c_m \rho_m k_m)^{\frac{1}{4}}} \frac{1}{f^{\frac{1}{4}}} \sqrt{\frac{2}{w^2}}. \quad (\text{C.28})$$

C.4 Heating by laser beam

This kind of noise is linked to the fact that a part of the power falling on the mirrors is dissipated into heat in the coating: this causes a distorsion of the mirror and a change in the reflectivity of the coating.

Distorsion by laser heating

Laser heating can cause a distorsion of the reflecting surface via the thermal expansion coefficient and hence a displacement noise.

When we consider power fluctuations due to *shot noise* the equivalent h is:

$$h_{\text{dist}}(f) = \frac{1}{L_{\text{arm}} f} \sqrt{2P_{\text{las}} \frac{hc}{\lambda}} \sqrt{2\Theta^2}, \quad (\text{C.29})$$

where the opto thermal coefficient Θ is:

$$\Theta = \frac{\alpha_m (1 + \sigma_m) \epsilon}{\pi^2 \rho_m c_m w^2}. \quad (\text{C.30})$$

and $\epsilon = 10^{-6}$.

Phase reflectivity of the coating

The effect of a fluctuating temperature is also to change the refraction indices of the dielectric layers stack constituting the reflective coatings. These index changes cause a detuning of each layer, or elementary Fabry Perot, which produces a spurious phase.

The equivalent spectral amplitude is:

$$h_{\text{ref}}(f) = \frac{d\Phi}{dn} \frac{dn}{dT} \frac{\lambda \epsilon}{\pi \sqrt{\pi \rho_m k_m c_m}} \frac{1}{\sqrt{f}} \sqrt{2P_{\text{las}} \frac{hc}{\lambda}} \frac{1}{\sqrt{2w^4}}, \quad (\text{C.31})$$

where $\frac{d\Phi}{dn} = 2.8$ and $\frac{dn}{dT} = 1.5 \cdot 10^{-5}$.

Bibliography

- [1] L. Reiter. *Earthquake Hazard Analysis*. Columbia University Press, 1991.
- [2] S. Stein and M. Wyssession. *An Introduction to Seismology, Earthquakes and Earth Structure*. Blackwell Publishing, 2003.
- [3] K. Aki and P. G. Richards. *Quantitative Seismology, 2nd edition*. University Science Books, California, 2002.
- [4] Peter M. Shearer. *Introduction to Seismology*. Cambridge University Press, 1999.
- [5] M. Born and E. Wolf. *Principles of Optics, 7th edition*. Cambridge University Press, 1999.
- [6] H. Kogelnik and T. Li. Laser beams and resonators. *Applied Optics*, 65:1550–1567, 1966.
- [7] S. Solimeno, B. Crosignani, and P. Di Porto. *Guiding, Diffraction and Confinement of Optical Radiation*. Academic Press, London, 1986.
- [8] A. Yariv. *Quantum Electronics*. Wiley, New York, 1988.
- [9] G. Hernandez. *Fabry-Perot interferometers*. Cambridge University Press, 1987.
- [10] J. Berger and R. H. Lovberg. Earth strain measurements with a laser interferometer. *Science*, 170:296–303, 1970.
- [11] J. Berger. Laser applications in the geosciences. *Western Periodicals, Calif.*, 50:203, 1960.
- [12] N. R. Goult, G. C. King, and A. J. Wallard. Iodine stabilized laser strainmeter. *Geophys. J. R. Astronomical Society*, 39:269–282, 1974.
- [13] N. R. Goult, G. C. King, and A. J. Wallard. High resolution laser strainmeter. *Nature*, 246:470–471, 1973.
- [14] R. G. Bilham, G. C. King, and D. Davies. New strainmeters for geophysics. *Nature*, 223:818–819, 1969.
- [15] V. A. Aleshin, M. N. Dubrov, and A. P. Yakovlev. A tunnel geophysical laser strainmeter. *Physics of the Solid Earth*, 29:358–363, 1993.

-
- [16] V. A. Aleshin, M. N. Dubrov, and A. P. Yakovlev. Laser interferometer for measuring earth's crust deformations. *Dokl. Akad. Nauk SSSR*, 253:1343–1346, 1980.
- [17] A. Araya, K. Kawabe, N. Mio, T. Satu, and K. Tsubono. Highly sensitive wideband seismometer using a laser interferometer. *Review of Scientific Instruments*, 64:1337–1341, 1993.
- [18] L. Crescentini and A. Amoruso. Installation of a high-sensitivity laser strainmeter in a tunnel in central italy. *Review of Scientific Instruments*, 68:3206–3210, 1997.
- [19] L. Crescentini, A. Amoruso, and R. Scarpa. Constraints on slow earthquake dynamics from a swarm in central italy. *Science*, 286:2132–2134, 1999.
- [20] J. Levine and J. L. Hall. Design and operation of a methane absorption stabilized laser strainmeter. *Journal of Geophysical Research*, 77:2595–2609, 1972.
- [21] C. Bostrom and V. Vali. Some earth strain observations with a thousand meter interferometer. *Earth Planet. Sci. Lett*, 4:436, 1968.
- [22] A Di Virgilio, et al. The low frequency facility fabry-perot cavity used as a speed-meter. *Physics Letters A*, 316:1–9, 2003.
- [23] G. Cella, A. Di Virgilio, P. La Penna, V. D'auria, A. Porzio, I. Ricciardi, and S. Solimeno. Optical response of a misaligned and suspended fabry perot cavity. *Physical Review A*, 74:1–14, 2006.
- [24] V. P. Mitrofanov, N. A. Styazhkina, and K. V. Tokmakov. Relation between mechanical barkhausen noise and magnetomechanical internal friction. *Journal De Physique*, 12:C8407–C8412, 1987.
- [25] H. Sakamoto, M. Okada, and M. Homma. Theoretical analysis of barkhausen noise in carbon steels. *IEEE Transactions on Magnetics*, 23:2236–2238, 1987.
- [26] L Holloway, et al. A coil system for virgo providing a uniform gradient magnet field. *Physics Letters A*, 171:162–166, 1992.
- [27] V. P. Mitrofanov, N. A. Styazhkina, and K. V. Tokmakov. Test mass damping associated with electrostatic actuator. *Classical and Quantum Gravity*, 19:2039–2043, 2002.
- [28] B. H. Lee, C. Zhao, L. Ju, and D. G. Blair. Implementation of electrostatic actuators for suspended test mass control. *Classical and Quantum Gravity*, 21:S977–S983, 2004.
- [29] M Plissi, et al. Geo 600 triple pendulum suspension system: seismic isolation and control. *Review of Scientific Instruments*, 71:2539–2545, 2000.
- [30] S. Grasso et al. Electrostatic systems for fine control of mirror orientation in interferometric gw antennas. *Physics Letters A*, 244:360–370, 1998.

- [31] R. Bruzzese. *Ottica, Laser e Applicazioni*. Liguori Editore, 1994.
- [32] O. Svelto. *Principles of Lasers*. Plenum Press, New York, 1982.
- [33] E. Calloni, L. Di Fiore, A. Grado, and L. Milano. A non linear signal extraction technique for length control of a fabry perot cavity. *Optics Communications*, 161:287–296, 1997.
- [34] F. Acernese and others [Virgo Collaboration]. Measurement of the seismic attenuation performance of the virgo superattenuator. *Astroparticle Physics*, 23:557–565, 2005.
- [35] F. Acernese and others [Virgo Collaboration]. Properties of the seismic noise at the virgo site. *Classical and Quantum Gravity*, 21:S433–S440, 2004.
- [36] A. Takamori. *Low Frequency Seismic isolation for Gravitational Wave Detectors*. Phd Thesis, University of Tokio.
- [37] R. Del Fabbro. *Super Attenuator Dynamics, PartI*. Virgo Note-PJT94-006 (1994).
- [38] R. Del Fabbro. *Super Attenuator Dynamics, PartII*. Virgo Note-NTS95-004 (1995).
- [39] M. Punturo. *The Virgo Sensitivity curve*. Virgo Note-PER-1390-51 (2004).
- [40] C. Cella and E. Cuoco. *Estimation of newtonian noise spectrum for the Virgo interferometer*. Virgo Note-PIS-1390-099 (1997).
- [41] G. Cagnoli and J. Kovalik. *Experimental check of calculation for eddy current damping between mirror and reference mass*. Virgo Note-PER-1390-080 (1997).
- [42] P. Saulson. *Interferometric gravitational wave detectors*. World Scientific Publishing, Singapore, 1994.
- [43] P. R. Saulson. Thermal noise in mechanical experiments. *Physical Review D*, 42:2437–2445, 1990.
- [44] A. Gillespie and F. Raab. Thermally excited vibrations of the mirrors of laser interferometer gravitational-wave detectors. *Physical Review D*, 52:577–585, 1995.
- [45] J. B. Jackson. *Classical Electrodynamics*. John Wiley, New York, 1962.
- [46] Tricomi. *Integral Equations*. Interscience, New York.
- [47] L. Landau and E. Lifchitz. *Teoria dell’elasticità*. Editori riuniti MIR, Roma, 1979.
- [48] A. Vicerè. *In proceedings of the International Summer School on Experimental Physics of GW*. World Scientific Publishing, Singapore, 2000.
- [49] G Cagnoli, et al. Low frequency internal friction in clamped-free thin wires. *Physics Letters A*, 255:230–235, 1999.

-
- [50] F. Bondu and J.Y. Vinet. Mirror thermal noise in interferometric gravitational wave detectors. *Physics Letters A*, 198:74–78, 1995.
- [51] F. Bondu, J.Y. Vinet, and P. Hello. Thermal noise in mirrors of interferometric gravitational wave antennas. *Physics Letters A*, 246:227–236, 1998.
- [52] J. V. Vinet. *Noise produced by opto-thermal couplings in mirrors*. Virgo Note-OCA-1390-166 (2001).
- [53] Y. Levin. Internal thermal noise in the ligo test masses: a direct approach. *Physical Review D*, 57:659–663, 1998.
- [54] V. Braginsky, M. Gorodetsky, and S. Vyatchanin. Thermodynamical fluctuations and photo-thermal shot noise in gravitational wave antennae. *Physics Letters A*, 264:1–10, 1999.

Ringraziamenti

*Al termine di questo percorso vorrei esprimere la mia gratitudine
al professor Milano, per aver creduto in me ed essere stato in ogni momento il mio
riferimento,
al professor Solimeno, per avermi ancora una volta incoraggiato nell'affrontare
nuovi problemi,
a Rosario, per essere stato l'esempio da seguire ed una guida preziosa,
a Luciano, per avermi messo a disposizione la sua esperienza nel risolvere i problemi
più complicati,
ad Enrico, per le sue delucidazioni chiare ed eleganti,
a Fabrizio, per i suoi saggi consigli,
a Fabio, per non essersi mai sottratto ad una mia richiesta di supporto,
a Fausto, per il suo contributo alle tante tematiche che ho affrontato in questi anni,
ad Antonio E., per il suo aiuto nella programmazione, e per aver ragionato con me
su ogni tipo di problema,
ad Antonio P., per la sua presenza eccezionale,
a Ketino, per la sua dignità nella vita e la sua serietà nel lavoro,
a Lara, per la sua serenità, la sua lucidità e la sua simpatia,
ad Adelfina, per avermi donato la sua amicizia,
alla cara Simona, per essere stata una valida compagna di lavoro nella fase finale
della tesi,
a Sergio, Nando, Saverio, Alessio, Silvio, Daniele, per essere stati davvero dei
buoni compagni di laboratorio,
a Cosimo, per essere stato fonte di fiducia e tranquillità,
a Peppino, Antonio e Carmen, per essere i miei Amici sempre e comunque.*

*Amico Padre, che mi ha insegnato ad essere me stessa,
a mia Madre, che mi ha insegnato a lavorare con passione e ad andare avanti,
a mio fratello, che mi ha insegnato a impegnarmi e a resistere,
a mia sorella, che mi ha insegnato a guardare la vita con Filosofia,
alla mia nipotina Vittoria, per aver riportato il Sole nelle nostre vite,
a Luca, per essere giorno dopo giorno la mia dolce ed insostituibile metà.*